Transient chaos analysis of string scattering

Takuya Yoda *

Department of Physics, Kyoto University, Kyoto 606-8502, Japan

Dec. 2022

A Dissertation in candidacy for
the degree of Doctor of Philosophy

*t.yoda(at)gauge.scphys.kyoto-u.ac.jp

Abstract

In this Ph.D. thesis, we look for chaos in highly excited strings. Recent studies show that black holes are characterized by chaos due to redshift near the event horizon. Since the microscopic degrees of freedom of a black hole originate in a highly excited string, it is expected that there is a chaotic dynamics in a highly excited string.

We have studied scattering amplitudes of open bosonic strings at tree-level. Our results show that there is no sign of chaos, however, we have not yet excluded all possibilities. We have conjectured that string scatterings can be chaotic if we include higher loop corrections, or if we consider closed strings, 5-point or 6-point amplitudes.

We hope that our work serves as a step toward the formulation of chaos in string scatterings, and bridges a gap between microscopic dynamics of strings and macroscopic nature of black holes.

Contents

1 Introduction

Why chaos?

Almost half a century ago, the black hole information paradox [1, 2] showed inconsistency between general relativity and quantum mechanics. Although general relativity and quantum mechanics are great achievements of modern physics, the paradox tells us that there must be unknown mysteries hidden inside the horizon. It is necessary to identify the appropriate microscopic degrees of freedom and reconcile its microscopic laws with macroscopic phenomena.

Microscopic degrees of freedom of a black hole originate in a highly excited string. The information paradox motivated the construction of a unitary S-matrix which describes black hole formation and evaporation [3–6][1]. The idea of the black hole S-matrix was elaborated in the principle of black hole complementarity[2] [10–13]. For a distant observer who phenomenologically describes a black hole as a standard quantum system, its microscopic degrees of freedom live near the event horizon. Its string interpretation shows that strings tend to form a single large string, implying that there is a correspondence between black hole states and highly excited string states [14]. The correspondence has been intensively studied in [14–22][3] to identify the microscopic origin of black holes.

Our next mission will be reconciling the laws of strings with macroscopic phenomena. Its key lies in black hole chaos. Chaos often refers to the irregularity of microscopic dynamics which causes thermalization on macroscopic scales. Black holes can be regarded as chaotic scatterers in the spirit of black hole S-matrix.[4] When a particle is shot into a black hole, its initial condition is apparently forgotten due to thermalization, and it takes a long time to evaporate due to the redshift near the event horizon (See Fig. 1). These two macroscopic features imply that there are microscopic irregular dynamics in black holes. The idea of black hole chaos is supported by the fact that a light ray passing near the event horizon is sensitive to perturbation of the horizon [7, 8, 24]. In the AdS/CFT correspondence, such sensitivity in the gravity side corresponds to quantum chaos on the holographic side [25–31].

From the viewpoint of chaos, black holes are distinguished objects. The point of black hole chaos is that it is associated with an event horizon. Indeed the Lyapunov exponent, a measure of chaos, is related to surface gravity. It is also conjectured that black holes are the

[1] See also an overview [7] and related works [8, 9]

[2] It was named after an idea to implement the equivalence principle. While a distant observer sees a phenomenological surface, called the stretched horizon, near the event horizon, an infalling observer sees nothing when crossing the event horizon. Apparently, these two observations contradict each other. However, there is no way for the infalling observer to report the absence of the stretched horizon to the distant observer. In this sense, there is complementarity between the two observers.

[3] See also a review [23].

[4] Chaos on the stretched horizon was already mentioned in [10].

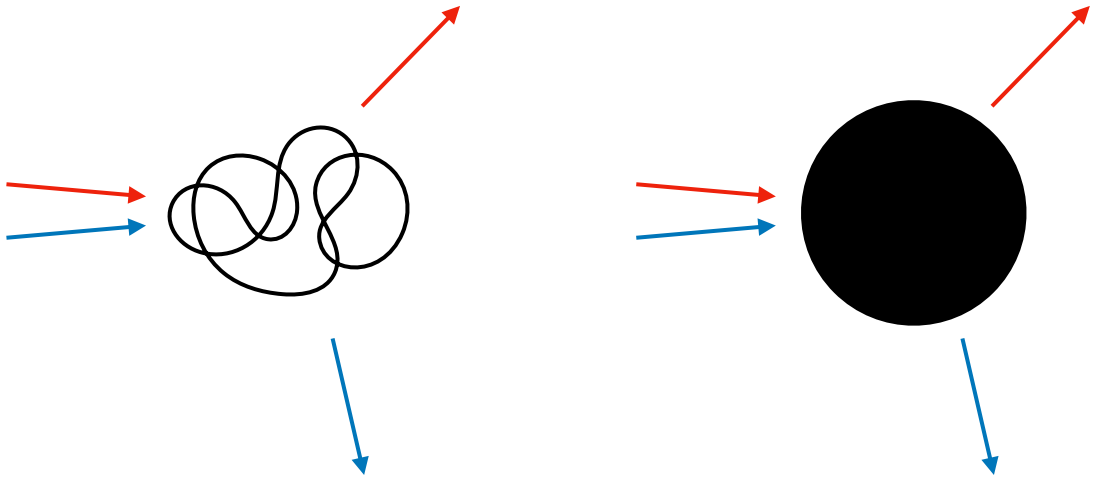

Figure 1: A highly excited string and a black hole are expected to be chaotic scatterers. When a particle is shot into a black hole, its initial conditions are apparently forgotten due to the thermalization, and it takes a long time for a particle to escape due to the redshift near the event horizon. Actually, initial condition sensitivity and a long delay-time are typical features of chaotic scatterers. We look for its microscopic origin in scatterings of a highly excited string.

fastest scramblers [32][5] and saturate chaos bounds [35, 36], implying that black holes are the most chaotic systems in the universe.[6] These features distinguish black hole chaos from the chaos in ordinary many body systems.

From the reasons above, there is a motivation to look for chaos in highly excited strings. Recently it has been shown that, even at tree-level, scattering amplitudes of highly excited strings are erratic functions [43, 44][7] which was thought to be a sign of chaos. However, the precise mechanism where chaos shows up has not yet been identified, nor has a quantitative evaluation of chaos been made.

Research

In this Ph.D. thesis, we look for chaos in string scatterings. As the first step, we study open bosonic strings at tree-level. In order to extract chaos in erratic scattering amplitudes, we resort to an established method: the transient chaos analysis.

Transient chaos is a type of chaos in which chaotic behavior lasts only for a finite time. For

[5] See also [33, 34].

[6] Precise definitions for scrambling and chaos in quantum systems are still in progress. While these conjectures motivate us to study black hole chaos, we should deepen our understanding of chaos to explain the thermal nature of black holes from microscopic viewpoints. See also [37–42].

[7] See also related works [45–47].

example, classical pinball scatterings are classified as transient chaos since a particle escapes from a chaotic scattering region within a finite time. In classical scatterings, there are two diagnoses for chaos: fractal structure in scattering data, and non-trivial geometrical structure in scattering region.

Firstly, the analysis of the fractal structure we employ is summarized as follows. Consider a particle scattered by a potential. The scattering data consists of a pair of the incoming and the outgoing angles of the particle motion, and we shall name it (θ, θ'). For a sufficient number of numerical experiments of the scattering, one finds a lot of the pair data, which is translated into a one-dimensional function $\theta'(\theta)$. For chaotic scattering, one should be able to find a fractal structure in this function $\theta'(\theta)$. Like in the chaotic dynamics produced by the baker map, the fractal structure detects chaotic dynamics within a scattering region [48–52].

We apply the transient chaos analysis described above to string scattering amplitudes. In particular, we consider scattering amplitudes of a tachyon and a highly excited string (HES), *i.e.* amplitudes of HES-tachyon to HES-tachyon, which mimic a scattering of a tachyon by a HES. To describe the in- and out-HES state, we follow the method adopted in the chaos analyses [43] using the DDF states [53].[8] To obtain the scattering data $\theta'(\theta)$ from the quantum scattering amplitudes, we extract the outgoing angles of the largest pole θ' of the amplitude for fixed incoming angles θ. Since generically string scattering amplitudes have multiple poles, we regard the largest pole as the most probable scattering in the quantum treatment.

Secondly, the analysis of geometrical structure is summarized as follows. Consider a classical pinball scattering. When a particle is shot into a scattering region, typically, it bounces between pins many times, and eventually escapes from the scattering region. Such irregular bounces are the source of chaos [48–52]. However, if the pins are aligned along a straight line, such irregular bounces do not occur. Thus the geometrical structure in a scattering region detects chaos.

In this research, we study the geometrical structure of a string scattering region. Since the geometrical structure is not given as the pins in classical scatterings, we reconstruct images of a scattering region from string amplitudes. We employ a formula used in [58, 59]. The reconstruction method is basically a Fourier transformation of string amplitudes, mimicking ordinal imaging technologies such as tomography.

Results and future works

Our results show that there is no fractal structure in the scattering data, nor non-trivial geometrical structure in the string scattering region. Thus we have concluded that there is no

[8] The calculation of the HES amplitudes was developed in [54]. See also [55,56] for HES states studied from the viewpoint of cosmic strings, and a recent paper [57] for a classical limit of HES amplitudes.

sign of chaos, at least, in open bosonic strings at tree-level.

Nevertheless, we have not yet excluded all possibilities. We expect that chaos shows up if we include higher loop corrections, or if we consider closed strings, 5-point or 6-point scattering amplitudes, based on physical interpretations of our results. Studying such cases is left for future works.

Another task might be a refinement of our strategy to extract chaos. One caveat is that the absence of the fractal structure may originate in the quantum nature of the string scattering amplitudes. As described above, our strategy to obtain the scattering data is to pick the largest pole in the amplitude. There could be a refined strategy to extract the scattering data by taking some classical limit of the scattering amplitudes.

Our ultimate goal is to pin down where chaos shows up in string scatterings, and to describe the thermal nature of black holes from microscopic viewpoints. Strings are finite-size objects and thus have exponentially large number of excitations. Those features cause complicated patterns of zeros and poles in scattering amplitudes, which distinguish strings from ordinary point particles. Only strings might be able to generate the most chaotic systems, and that might be the reason why a black hole horizon emerges.[9] We hope that this research serves as a step toward the formulation of chaos, and bridges a gap between strings and black holes.

Organization of this thesis

This paper is organized as follows. In Sec. 2, we review black hole chaos. The point of black hole chaos is the redshift near the horizon. Later we review the correspondence principle to motivate us to look for the origin of black hole chaos in highly excited strings. Then we review recent studies on erratic scatterings of highly excited strings.

In Sec. 3, we review transient chaos. We introduce basic concepts and measures to characterize chaos. We can detect chaotic dynamics from the fractal structure in scattering data and the geometrical structure in a scattering region.

In Sec. 4, we look for a fractal structure in scattering data of a highly excited string. We compute a scattering amplitude of HES-tachyon to HES-tachyon. Although its scattering data are highly erratic, we could not find any fractal structure. We discuss the possibility that chaos shows up if we include higher loop corrections.

In Sec. 5, we study geometrical structure in a scattering region of highly excited strings. We employ an imaging method: Fourier transformation of string amplitudes. Our results show that strings look like double-slits. We discuss the possibility that chaos shows up if we

[9]Just showing that a given system is chaotic is insufficient since typical systems in the universe are chaotic. This research will become truly valuable when we identify specific dynamics of strings which explain the development of black holes.

consider closed strings, 5-point or 6-point scattering amplitudes.

In Sec. 6, we conclude this paper and discuss future prospects.

2 Black hole chaos

In this section, we review black hole chaos, which is a bridge between the thermal properties of black holes and the microscopic dynamics of strings. Black holes are regarded as chaotic scatterers due to the event horizon. A particle orbit near the event horizon is sensitive to its perturbation due to the redshift. Such a sensitivity corresponds to quantum chaos in the AdS/CFT correspondence. Also, a phenomenological description of black holes shows that black holes are the fastest scramblers. It is conjectured that black holes saturate chaos bounds. These features distinguish black holes from ordinary chaotic systems.

The microscopic origin of black hole chaos is expected to lie in highly excited strings. There is a correspondence between black hole states and single string states. A transition from a highly excited string to a black hole implies that the geometrical structure of a string is highly complicated just before black hole formation. Recently, it has been shown that scattering amplitudes involving highly excited strings are erratic functions.

2.1 Redshift near horizon

Sensitivity to horizon perturbation

Let us consider a $D = d + 1 = 4$ dimensional Schwarzschild black hole, whose metric is given by

$$-\mathrm{d}\tau^2 = -\left(1 - \frac{2GM}{r}\right)\mathrm{d}t^2 + \left(1 - \frac{2GM}{r}\right)^{-1}\mathrm{d}r^2 + r^2\,\mathrm{d}\Omega^2\,. \tag{2.1}$$

This metric is useful for a distant observer. A clock at infinity records the Schwarzschild time t. Although the metric is singular at the event horizon $r = 2GM$, it is just a coordinate singularity. Indeed the curvature near the horizon is finite $\sim \kappa^2 < \infty$. Here $\kappa = 1/4GM$ is the surface gravity. Also, a free falling observer reaches the event horizon within a finite proper time.

The Rindler coordinates (ω, ρ) are useful to describe the near horizon behaviors. It is given by

$$\mathrm{d}\omega = \kappa\,\mathrm{d}t\,, \tag{2.2}$$

$$\mathrm{d}\rho = \left(1 - \frac{2GM}{r}\right)^{-1/2}\mathrm{d}r\,. \tag{2.3}$$

The Rindler time ω is just the dimensionless version of the Schwarzschild time, and ρ is the proper distance. The metric near the event horizon $\rho \simeq 0$ reduces to

$$-\mathrm{d}\tau^2 \simeq -\rho^2\,\mathrm{d}\omega^2 + \mathrm{d}\rho^2 + r^2\,\mathrm{d}\Omega^2\,. \tag{2.4}$$

We can find the Hawking temperature $\beta_{\rm BH}$ by Wick rotation and by removing its conical singularity $\omega_{\rm E} \sim \omega_{\rm E} + 2\pi$. Then the Euclidean time at infinity is periodic as $t_{\rm E} \sim t_{\rm E} + 2\pi/\kappa$, which tells us that the Hawking temperature is $\beta_{\rm H} = 2\pi/\kappa$.

The Minkowski coordinates (T, Z) are useful to describe a free falling observer. It is given by

$$T = \rho \sinh \omega, \tag{2.5}$$

$$Z = \rho \cosh \omega. \tag{2.6}$$

Writing the S^2 part as $X^2 + Y^2 = r^2 \, \mathrm{d}\Omega^2$, the metric reduces to

$$-\,\mathrm{d}\tau^2 = -\,\mathrm{d}T^2 + \mathrm{d}Z^2 + \mathrm{d}X^2 + \mathrm{d}Y^2 \,. \tag{2.7}$$

Consider a free falling particle $1 = \mathrm{d}T \,/\, \mathrm{d}\tau$, $0 = \mathrm{d}Z \,/\, \mathrm{d}\tau$. Its momentum and position behave as

$$p \sim e^{+\kappa t}, \tag{2.8}$$

$$\rho \sim e^{-\kappa t}, \tag{2.9}$$

at late time $\kappa t \gg 1$. Due to the redshift, a free falling particle asymptotically approaches the event horizon. Although the particle cannot reach the event horizon within a finite Schwarzschild time t, it acquires exponentially large momentum, causing a high energy shock wave.

The Kruskal-Szekeres coordinates (U, V) extend the patch into the region inside the event horizon. It is given by

$$U = -e^{-\kappa(t - r^*)}, \tag{2.10}$$

$$V = +e^{+\kappa(t + r^*)}. \tag{2.11}$$

where r^* is the Tortoise coordinates, or Regge-Wheeler coordinates, such that

$$\left(1 - \frac{2GM}{r}\right)^{-1/2} \mathrm{d}r = \left(1 - \frac{2GM}{r}\right)^{+1/2} \mathrm{d}r^* \,. \tag{2.12}$$

Paths $U = \text{const.}/V = \text{const.}$ describe outgoing/incoming light rays, respectively. The metric is rewritten as

$$-\,\mathrm{d}\tau^2 = -2A \, \mathrm{d}U \, \mathrm{d}V + r^2 \, \mathrm{d}\Omega^2 \,, \tag{2.13}$$

where

$$A = \frac{16(GM)^3}{r} e^{-\frac{r}{2GM}}. \tag{2.14}$$

Now let us analyze sensitivity to horizon perturbation. Consider an incoming light ray $V = V_{\rm in} = 0$ with momentum $p_{V,{\rm in}}$ shot into a black hole. Due to the redshift factor (2.8), the momentum of the incoming ray exponentially increases, causing a shock wave near the event horizon. Its shock wave geometry is computed in [7, 8]. The result is

$$-\,\mathrm{d}\tau^2 = -2A\,\mathrm{d}V\,(\mathrm{d}U - F(V,\Omega)\,\mathrm{d}V) + r^2\,\mathrm{d}\Omega^2\,, \tag{2.15}$$

where

$$-\Delta_{S^2}F + F = 8\pi G(-p_{V,{\rm in}})\,\delta(V - V_{\rm in})\delta^2(\Omega - \Omega_{\rm in}). \tag{2.16}$$

It shows that the shock wave delays a clock around it, causing a shift of U coordinate. If another outgoing ray $U = $ const. crosses the incoming ray $V = 0$, its path shifts as

$$\Delta U = \int \mathrm{d}U = \int \mathrm{d}V\ F(V,\Omega). \tag{2.17}$$

Then the arrival time at infinity is also shifted [7, 8, 24]. It is

$$\Delta t = \frac{\mathrm{d}t}{\mathrm{d}U}\Delta U = \kappa^{-1}e^{\kappa(t-r^*)}\Delta U. \tag{2.18}$$

Remark that the exponential factor $e^{\kappa t}$ comes from the redshift near the event horizon. For a distant observer, who describes a black hole phenomenologically as a standard object, a small shift ΔU grows exponentially with respect to time.

An exponential growth of a small deviation is a necessary condition for chaos. One of the important measures characterizing chaos is the Lyapunov exponent. Consider a dynamical system with a phase space $\{q_1, \dots q_d, p_1, \dots, p_d\}$. The Lyapunov exponent $\lambda_{\rm L}$ is defined by the rate of expansion of a small deviation as

$$\delta q_i(t) \sim \delta q_i(0) e^{\lambda_{\rm L} t} \tag{2.19}$$

at late time $\lambda_{\rm L} t \gg 1$. The Lyapunov exponent measures how the system is sensitive to an initial condition. More precise definitions of chaos and other important measures will be introduced in the next section Sec. 3.

The result is also interpreted as follows. When an incoming shock wave crosses the event horizon, the horizon grows due to an injected energy into a black hole. Then another light ray travels a path closer to the new horizon. It takes an exponentially longer time to go away from the horizon due to the redshift.

Holography

The authors of [25–31] related a shock wave geometry to an exponential growth of out-of-time-order correlator (OTOC) [60] in the AdS/CFT correspondence. They considered a thermofield double state corresponding to a two sided black hole

$$|\Psi\rangle = \frac{1}{Z^{1/2}} \sum_n e^{-\beta E_n/2} |n\rangle_{\rm L} |n\rangle_{\rm R} \,, \tag{2.20}$$

and considered a correlator corresponding to shock wave geometry

$$\langle\Psi| V(t_1)W(t_2)V(t_1)W(t_2) |\Psi\rangle \,. \tag{2.21}$$

Here $V(t_1)$ and $W(t_2)$ create light rays inside the bulk whose endpoints are at boundary time t_1, t_2 respectively. The correlator was computed by interpreting it as a scattering amplitude.

The S-matrix to compute bulk scattering amplitude was constructed by [7, 8]. Let us rewrite the shift due to an incoming shock wave as

$$F(V,\Omega) = (-\delta P_{V,\rm in})\delta(V - V_{\rm in})\, f(\Omega,\Omega_{\rm in}). \tag{2.22}$$

The shift in the U-direction must cause a phase shift for an outgoing state. Then the state must be replaced as

$$\begin{aligned} |P_{\rm out}\rangle &\to \exp\left[i \int {\rm d}^2\Omega_{\rm out}\ \hat{P}_{\rm out}\Delta U \right] |P_{\rm out}\rangle \,, \\ &= \exp\left[i \int {\rm d}^2\Omega_{\rm out}\ \hat{P}_{\rm out} f(\Omega_{\rm out},\Omega_{\rm in})(-\delta P_{V,\rm in}) \right] |P_{\rm out}\rangle \,. \end{aligned} \tag{2.23}$$

Summing over incoming particles, the S-matrix for a shock wave geometry is constructed as

$$\langle P_{\rm out}|P_{\rm in}\rangle = \mathcal{N} \exp\left[-i \int {\rm d}^2\Omega_{\rm in}\, {\rm d}^2\Omega_{\rm out}\ P_{\rm out} f(\Omega_{\rm out},\Omega_{\rm in}) P_{\rm in} \right]. \tag{2.24}$$

Its perturbative expansion at the leading order

$$S \sim e^{i\delta} \sim 1 + i\delta \tag{2.25}$$

can be roughly evaluated by noting that

$$f(\Omega_{\rm out},\Omega_{\rm in}) \sim G \sim \frac{\rm Area}{S_{\rm BH}}, \tag{2.26}$$

$$\Delta U \sim e^{\kappa(t_1 - t_2)}. \tag{2.27}$$

Using this S-matrix to compute the bulk scattering amplitude, we find that the OTOC grows as

$$\langle\Psi| V(t_1)W(t_2)V(t_1)W(t_2) |\Psi\rangle \sim \frac{1}{S_{\rm BH}} e^{\kappa(t_1 - t_2)}. \tag{2.28}$$

The rate of the growth of OTOC is a quantum version of the Lyapunov exponent. For example, consider an ordinary quantum mechanical system, and its OTOC[10]

$$-\left\langle [q(t), p(0)]^2 \right\rangle . \tag{2.29}$$

Taking the semi-classical limit, we can replace the commutator with the Poisson bracket. Then we find that

$$\begin{aligned} -\left\langle [q(t), p(0)]^2 \right\rangle &\sim \{q(t), p(0)\}^2 = \left(\frac{\partial q(t)}{\partial q(0)} \right)^2 \\ &\sim e^{2\lambda_{\rm L} t}. \end{aligned} \tag{2.30}$$

Thus the exponential growth of OTOC is understood as the quantum version of the Lyapunov exponent.

Fast scrambling

For a distant observer who phenomenologically describes a black hole as a standard system, a black hole looks like the fastest scrambler.[11] We review the fast scrambling conjectured by [32].

Let us consider the near horizon geometry of a Schwarzschild black hole, and write its S^2 part as $X_\perp^2 = X^2 + Y^2 = r^2 \, \mathrm{d}\Omega^2$. We consider free falling charged particles: $1 = \mathrm{d}T \,/\, \mathrm{d}\tau \,, 0 = \mathrm{d}Z \,/\, \mathrm{d}\tau \,, X_\perp = 0$, and observe their electrical field at infinity. When the charged particles approach the stretched horizon, a distant observer sees an electrical field

$$\begin{aligned} E_\rho = E_Z &= \frac{Z - Z_0}{[(Z - Z_0)^2 + X_\perp^2]^{3/2}} \\ &\sim \ell_{\rm P}^{-2} \frac{e^\omega}{[e^{2\omega} + \xi_\perp^2]^{3/2}}, \end{aligned} \tag{2.31}$$

where we defined a dimensionless coordinate $\xi_\perp = X_\perp / \ell_{\rm P}$ on the stretched horizon. The stretched horizon is a phenomenological surface $r \sim 2GM + \ell_{\rm P}$ on which microscopic degrees of freedom live for a distant observer [10–14]. The distant observer can phenomenologically understand that charges are distributed as

$$\sigma(\omega, \xi_\perp) \sim E_\rho. \tag{2.32}$$

[10] This is also called the out-of-time-order commutator, which is roughly equal to the out-of-time-order correlator plus some trivial terms.

[11] Precise definitions for scrambling and chaos in quantum systems are still in progress. See also [37–42].

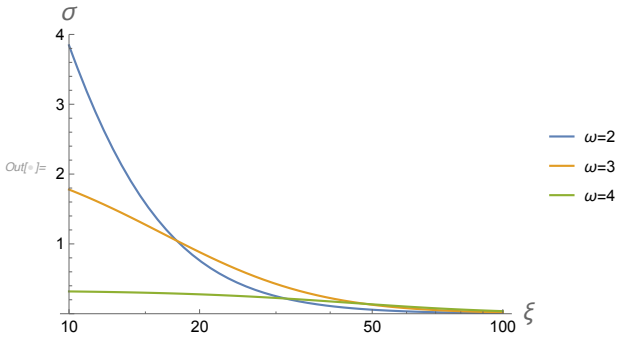

Figure 2: Surface density of charges for a distant observer. Charges are spread out on the stretched horizon at an exponential rate.

This surface charge density is plotted in Fig. 2. As the time at infinity progresses, the charges are spread over the stretched horizon. Note that for a fixed $\xi_\perp$ local charge density reaches the maximum at

$$\omega \sim \ln \xi_\perp. \tag{2.33}$$

Then we can evaluate the time ω^* when charged particles are fully spread over a black hole. Substituting $\xi_\perp \sim r_{\rm BH} \sim S_{\rm BH}^{1/2}$

$$\omega^* \sim \ln S_{\rm BH} \tag{2.34}$$

Remark that this scrambling time is faster than ordinary systems $\omega^* \sim S^{\#}$, and that the logarithm came from the redshift factor. In this sense, a black hole is regarded as a fast scrambler.

Black holes are distinguished objects from the viewpoint of chaos. It is conjectured that black holes saturate chaos bound [35]

$$\lambda \leq \lambda_{\rm L} = \kappa = \frac{2\pi}{\beta_{\rm BH}}. \tag{2.35}$$

Another type of chaos bound is proposed in [36], which is consistent with the above chaos bound at the high temperature limit.

From the fast scrambling conjecture and chaos bounds, we may expect that there is a distinguished dynamics which realizes the maximally chaotic systems.

2.2 Correspondence principle

In the context of black hole complementarity [10–12], the author of [14] speculated that there is a one-to-one correspondence between black hole states and single string states. In this part, we review a correspondence between a microscopic black hole and a highly excited string.

Let us consider a $D = d + 1 = 4$-dimensional Schwarzschild black hole. Its Schwarzschild radius and the Bekenstein-Hawking entropy are

$$r_{\rm BH} = 2GM, \tag{2.36}$$

$$S_{\rm BH} = \frac{\text{Area}}{4G} = 4\pi G M^2. \tag{2.37}$$

When the black hole size is of the order of string scale, the black hole entropy is compatible with the string entropy as follows.

Consider a string with mass M. Let $\alpha' \sim 1$, for simplicity, so that string tension is of the order of unity. Then the total length is $L \sim M$. The string mass is expressed by its excitation level N as $M \sim N^{1/2}$. For a fixed excitation level N, there are as many string states as the number of partition of N. Thus string state degeneracy grows exponentially as $n(M) \sim e^{\beta_{\rm H} M}$. Here a constant $\beta_{\rm H} > 0$ is called the Hagedorn temperature.

The effective size of the string is $l \sim L^{1/2}$. This is understood by a random walk picture of a string, in which a string is regarded as the path of a random walk. Using the microcanonical ensemble of string states, we find that the string entropy is $S \sim \ln n(M)$. Thus

$$l \sim L^{1/2} \sim N^{1/4}, \tag{2.38}$$

$$S \sim M \sim N^{1/2}. \tag{2.39}$$

When a black hole is string scale size $1 \sim r_{\rm BH} \sim GM$, the black hole entropy and the string entropy are compatible as

$$S_{\rm BH} \sim M \sim S. \tag{2.40}$$

Interpreting the gravitational constant as the string coupling $G \sim g^2$, such a correspondence occurs at

$$g \sim G^{1/2} \sim M^{-1/2} \sim N^{-1/4}. \tag{2.41}$$

However, the effective string size $l \sim N^{1/4}$ is apparently too large for $N \gg 1$, comparing to the black hole size $1 \sim r_{\rm BH}$. Actually, a string contracts from the random walk size to the string scale due to its self-interactions. Although the string coupling g is small at the corresponding point, there is a non-perturbative effect which causes the contraction of a string. Since

$$\beta \sim \frac{\partial S(M)}{\partial M} \sim \beta_{\rm H}, \tag{2.42}$$

we shall analyze a region slightly below the Hagedorn temperature $0 < \beta - \beta_{\rm H} \ll 1$. See also *e.g.* [61] for the thermodynamics of strings. As we will see below, self-interactions decrease the temperature of a string.

Let us use the canonical ensemble below. We will follow computations by [19]. Consider strings wound on a thermal circle. Near the Hagedorn temperature, two winding modes with the winding number ± 1 become massless, and eventually become tachyonic above the Hagedorn temperature. Thus strings near the Hagedorn temperature are effectively described by two real scalar modes on a thermal circle. Combining the two scalars into a single complex scalar χ, its action is

$$I[\beta;\chi] = -\beta \int \mathrm{d}^d x \left(|\partial\chi|^2 + m^2(\beta)|\chi|^2 \right), \tag{2.43}$$

where

$$m^2(\beta) \sim M^2(\beta)\big|_{\text{winding mode}} \sim \beta^2 - \beta_{\mathrm{H}}^2. \tag{2.44}$$

Its first quantization gives a single string contribution.

We can check that this thermal scalar formalism reproduces the single string degeneracy $n(M) \sim e^{\beta_{\mathrm{H}} M}$ and the random walk size $l(M) \sim N^{1/4} \sim M^{1/2}$. Let us define a partition function as

$$\mathbf{Z} = \int \mathcal{D}\chi \, e^{-I[\beta;\chi]}. \tag{2.45}$$

Its single string contribution is its logarithm $Z = \ln \mathbf{Z}$. Critical behavior $m^2(\beta) \ll 1$ is dominated by the zero mode as

$$\begin{aligned} Z &\sim \ln \mathbf{Z} \\ &\sim -\ln \det\left(-\partial^2 + m^2(\beta)\right) \sim -\ln(\beta - \beta_{\mathrm{H}}) \\ &\sim \int_0^\infty \frac{\mathrm{d}M}{M} \, e^{-(\beta-\beta_{\mathrm{H}})M} = \int_0^\infty \mathrm{d}M \; M^{-1} e^{\beta_H M} \, e^{-\beta M} \end{aligned} \tag{2.46}$$

Then the single string degeneracy $n(M) \sim e^{\beta_{\mathrm{H}} M}$ is reproduced.

Since the random work size is $\sim l(M)$, the distribution of strings are approximately $\sim e^{x^2/l^2(M)}$. Its thermal ensemble is

$$\int_0^\infty \mathrm{d}M \; n(M) e^{-\beta M} \, e^{-x^2/l^2(M)} \sim e^{-Cm(\beta)x} \tag{2.47}$$

where C is a constant $\sim \mathcal{O}(1)$. Note that its typical size $m(\beta)^{-1}$ agrees with the correlation length of the thermal scalar. Thus the thermal scalar formalism is consistent with the random walk picture.

Now let us introduce self-interactions. Including the lightest modes, dilaton and graviton, actions are

$$I[\beta;\chi] = -\beta\sqrt{G_{\tau\tau}} \int \mathrm{d}^d x \, \sqrt{\det G_{ij}} \, e^{-2\Phi} \left[G^{ij} \partial_i \chi^* \partial_j \chi + m^2(\beta) \chi^* \chi \right],$$

$$I[\beta; G, \Phi] = -\frac{\beta\sqrt{G_{\tau\tau}}}{16\pi G}\int \mathrm{d}^d x\,\sqrt{\det G_{ij}}\,e^{-2\Phi}\left[R + 4G^{ij}\partial_i\Phi\partial_j\Phi\right], \tag{2.48}$$

where the mass $m(\beta)$ is modified to

$$m^2(\beta) \sim \beta^2 G_{\tau\tau} - \beta_{\mathrm{H}}^2 \tag{2.49}$$

since gravity changes the proper length.

[19] solved this problem by mean field approximation. The thermal scalar χ obeys the Schrödinger equation with an effective potential due to self-interactions. Rescaling χ and coordinates, it becomes

$$\left[-\frac{\partial^2}{\partial\xi_i^2} - \int \mathrm{d}^d\xi' \,\frac{|\psi(\xi')|^2}{|x|_>^{d-2}}\right]\psi(\xi) = \varepsilon\psi(\xi), \tag{2.50}$$

where

$$\xi = (g^2 M)^{1/(4-d)} x, \tag{2.51}$$

$$\psi(\xi) = (g^2 M)^{-d/(8-2d)}\chi(x), \tag{2.52}$$

and where

$$\varepsilon \sim -(g^2 M)^{-2/(4-d)}\beta_H(\beta_{\mathrm{c}} - \beta_{\mathrm{H}}). \tag{2.53}$$

Here $|\xi|_>$ is defined as the greater of $|\xi|$ and $|\xi'|$. Its term is interpreted as an effective potential due to gravitational sources inside a region $[0, \xi]$. The gravitational constant is identified with the string coupling $G \sim g^2$. Also β_{c} is the local temperature around an effective potential region. It is determined by consistency of mean field approximation[12]. The size of the wave function is of the order of the potential size $\xi \sim \mathcal{O}(1)$. Imposing a bound state condition $\varepsilon \sim -\mathcal{O}(1)$, we obtain

$$l \sim (g^2 M)^{-1/(4-d)} \sim (g^2 N^{1/2})^{-1/(4-d)}. \tag{2.54}$$

Then the effective size of a string at the transition point $g \sim N^{-1/4}$ is

$$l \sim 1. \tag{2.55}$$

This agrees with the black hole size $1 \sim r_{\mathrm{BH}}$, thus the discrepancy of two sizes of a black hole and a string is solved.

It is remarkable that a string can contract to the string scale size $l \sim 1$ while its total length remains $L \sim N^{1/2} \gg 1$. It shows that the long string is confined to a tiny region, thus the geometrical structure of a string must be highly complicated when self-interactions are included. It motivates us to look for the origin of black hole chaos in a highly excited string.

[12] This is improved in [22] to study phase transition between a string and a black hole. The authors introduced another scalar to describe the radius of thermal circle. While its radius is fixed to β at infinity, locally the radius changes.

2.3 Erratic string scattering

Recently, [43, 44][13] studied on scattering amplitudes of highly excited strings. The authors employed the DDF operator construction method to obtain a general formula. Its physical interpretation is that a highly excited string is constructed by shooting many photons into a tachyon. The photons supply energy and angular momentum to the tachyon, and finally picking out a pole, we find a contribution from a highly excited string.

In this part, we review the result by [44]. Let us consider open bosonic strings. We shoot J photons, into a tachyon, with momentum $\{-N_a q\}_{a=1,\ldots,J}$ and with the same polarization λ.[14] Here q is a unit null vector perpendicular to the polarization vector. Picking out a pole, we can construct a highly excited state with mass $M^2 = 2(N-1)$, $N = \sum_{a=1}^{J} N_a$, and with angular momentum J.

Then we can compute a decaying amplitude of a highly excited string into two tachyons. Denoting the tachyon momentum by p, the amplitude is

$$\mathcal{A} = \prod_{a=1}^{J} (-p \cdot \lambda) \frac{\Gamma(N_a + N_a p \cdot q)}{\Gamma(N_a)\Gamma(1 + N_a p \cdot q)}. \tag{2.56}$$

Note that this amplitudes has many poles and zeros due to the Gamma functions, which corresponds to a distinguished feature of a string that strings have many excitations. The authors of [43, 44] evaluated amplitudes numerically for generic partitions of the excitation level $N = \sum_{a=1}^{J} N_a$ and showed that their behaviors are highly erratic.

[13] See also [45–47]

[14] See [43, 44, 54] for more general cases.

3 Transient chaos

In this section, we review transient chaos. Transient chaos is characterized by three properties: unpredictability, aperiodicity, and fractality. These are generated by three key mechanisms: stretching, folding, and escape.[15] We demonstrate how transient chaos is generated in a simple toy model called the gluttonous baker map. We see that fractality in the phase space is a good probe of chaos. Other measures of chaos are also introduced later.

Next, we review classical scatterings of a particle by multiple disks. Typical scattering systems show chaotic behavior and generate a fractal structure. However, when all disks are aligned along the same straight line, the system does not show chaotic behavior since the folding mechanism is absent in such a case. In this sense, the geometrical structure in a scattering region is a good probe of chaos.

This review is based on [40–42, 48–52].

3.1 Basic concepts

Transient chaos is a type of chaos whose chaotic behavior lasts only for a finite time. By contrast, ordinary chaos which lasts for an infinitely long time is called permanent chaos.[16] Transient chaos is characterized by three properties in the phase space[17]:

- Unpredictability
- Aperiodicity
- Fractality[18]

These are generated by three key mechanisms:

- Stretching
- Folding
- Escape

The unpredictability means that the deviation of the initial condition grows exponentially. When it comes to simulating a chaotic system numerically, we need an exponentially powerful computer to improve the precision. Thus it is practically impossible to know the long term behavior of a chaotic system. The mechanism which expands a deviation is called stretching.

[15] Compared to the stretching and folding mechanisms, the word "escape mechanism" is not popularly used. However, we use these three words on an equal footing in this paper so that we can clearly understand how fractal structure appears from transient chaos.

[16] Also, there is another classification: dissipative/conservative chaos.

[17] These properties are not independent. Indeed measures of chaos are related to each other as we will see later.

[18] Permanent chaos also shows fractal structure, but it does not originate in the escape mechanism of transient chaos.

The stretching mechanism is iterated by the folding mechanism. Then the expansion of a deviation lasts for a long time, resulting aperiodic phase space. The expansion rate is measured by the Lyapunov exponent. Its topological versions are called the topological entropy and the metric entropy.

The fractality means that the chaotic sets in the phase space have a self-similar structure and fill only the partial of the phase space. It is associated with the escape mechanism where some regions in the phase space escape from chaotic regions. The measure for the fractal structure is called the fractal dimension.

In the following parts, we demonstrate how these characteristics and key mechanisms are related in simple toy models: the baker map and its modification, the gluttonous baker map.

Stretching and folding

The baker map[19] is one of the simplest and analytically tractable examples of chaos. It contains all the key mechanisms for chaos: stretching and folding.

Suppose that we have a piece of bread dough with a unit length $[0, 1)$. We put a teaspoon of flavor powder at x on the dough, and knead it so that the powder is distributed uniformly. The kneading process consists of stretching the dough to twice its length, cutting it, and folding them to the original size. The position x of the flavor powder is mapped by a function

$$f_{\rm b}(x) = \begin{cases} 2x & 0 \le x < 1/2 \\ 2x - 1 & 1/2 \le x < 1 \end{cases} . \tag{3.1}$$

Repeating the same process n times, it is mapped to

$$f_{\rm b}^{\circ n}(x) = f_{\rm b}(f_{\rm b}(\dots f_{\rm b}(x))), \tag{3.2}$$

where $\circ n$ denotes the n-th iteration.

We can easily confirm that the flavor powder is distributed randomly. It is convenient to use binary representation. Suppose that the original position of the flavor powder is represented by

$$x_0 = (0.\xi_1\xi_2\dots\xi_{n+1}\xi_{n+2}\dots)_2, \tag{3.3}$$

and that the lower digits $\xi_{n+1}, \xi_{n+2}\dots$ are not specified since they are much smaller than the size of the teaspoon. By the definition of the map $f_{\rm b}(x)$, the position x_0 is mapped to

$$x_n = (0.\xi_{n+1}\xi_{n+2}\dots)_2 \tag{3.4}$$

[19]The baker map often refers to a two-dimensional map. It generates a fractal structure in a one-dimensional direction on a two-dimensional sheet to which the map is applied. In this paper, we analyze a one-dimensional version of the baker map, ignoring the fractal structure which does not originate in transient chaos.

after the n-th iteration. Since the smaller digits cannot be specified, effectively the flavor powder is randomly distributed. Remark that the sequence $x_n \to x_{n+1} \to \cdots$ is not periodic and that the deviation of the smaller digits $\xi_{n+1}, \xi_{n+2}, \ldots$ grows exponentially by the iterations of the stretching and the folding. The chaoticity of the baker map originates in the stretching and the folding mechanisms. The stretching of the bread dough expands a small deviation, resulting in shifts of the digits ξ_i to the left. The folding of bread dough keeps it in its original size and allows iterations for a long time.

Also, there is another version of the map [20]

$$f_{\rm t}(x) = \begin{cases} 2x & 0 \le x < 1/2 \\ 2(1-x) & 1/2 \le x \le 1 \end{cases} . \tag{3.5}$$

Similarly this map shows chaotic behavior.

Escape

Transient chaos is a type of chaos in which a chaotic process lasts only for a finite time. Its essence is also understood in a simple toy model, the gluttonous baker map. We can clearly see that a fractal structure in the phase space is associated with the escape mechanism.

Suppose that we have a piece of bread dough with a unit length $[0, 1]$. We knead the bread dough with a teaspoon of flavor powder. However, this time the baker is so gluttonous. Kneading processes are as follows. The bread dough is stretched to triple its length, and cut into three pieces. The gluttonous baker eats one of the three pieces, and folds only the two pieces into the original size. The position x of the flavor powder is mapped by a function

$$f_{\rm gb}(x) = \begin{cases} 3x & 0 \le x \le 1/3 \\ 3(1-x) & 2/3 \le x \le 1 \end{cases} . \tag{3.6}$$

Here the middle piece $1/3 < x < 2/3$ is eaten by the baker.

This map also generates chaos in the same way as the ordinary baker map $f_{\rm b}(x)$. However, in this case, some subset of the bread dough $[0, 1]$ escapes from the chaotic processes within a finite time. Let us denote, by C, a subset of the original dough $[0, 1]$ which is not eaten by the baker. By the definition of the function $f_{\rm gb}(x)$, we can find a subset $C_n \subset [0, 1]$ which is not eaten the baker until the n-th iteration. For each n, we find that

$$C_0 = [0, 1], \tag{3.7}$$

$$C_1 = \left[0, \frac{1}{3}\right] \cup \left[\frac{2}{3}, 1\right], \tag{3.8}$$

[20] This is called the tent map.

$$C_2 = \left[0, \frac{1}{9}\right] \cup \left[\frac{2}{9}, \frac{3}{9}\right] \cup \left[\frac{6}{9}, \frac{7}{9}\right] \cup \left[\frac{8}{9}, 1\right], \tag{3.9}$$

$$\vdots \quad \vdots \tag{3.10}$$

The set C is the limit $C = \lim_{n\to\infty} C_n$. This is nothing but the Cantor set. The Cantor set is a typical fractal set, which has a self-similar structure and non-integer dimension.

Remark that transient chaos generates a fractal structure in the phase space. The original interval $C_0 = [0, 1]$ is mapped to a unit interval but with a hole at the middle $C_1 = [0, 1/3] \cup [2/3, 1]$ since the middle region $[1/3, 2/3]$ escapes from the mapping (or is eaten by the baker). The same processes are performed iteratively due to the stretching and folding mechanism, resulting in a self-similar structure of intervals with a hole.

Inversely a fractal structure of phase space probes chaos. Its self-similar structure means that there are some iteration mechanisms. For each iteration, the bread dough needs to be stretched more than the unity in order to compensate for the loss of the bread dough. The stretched dough needs to be folded to keep its original size.

3.2 Measures

We introduce measures of chaos. As explained before, fractality is a good probe of chaos. It is measured by the fractal dimension. We will see that the fractal dimension determines the Lyapunov exponent. Although we will use the gluttonous baker map as an example in this section, the following measures and relations between them can be generalized to other fractal sets.

Let us consider the gluttonous baker map

$$g_{\rm gb}(x) = \begin{cases} \varepsilon_1^{-1} x & 0 \le x \le \varepsilon_1 \\ \varepsilon_2^{-1}(1-x) & 1-\varepsilon_2 \le x \le 1 \end{cases}. \tag{3.11}$$

We assume $0 < \varepsilon_1 < \varepsilon_2 < 1$ without loss of generality. This map generates the Cantor set as the limit of

$$I^{(0)} = [0, 1], \tag{3.12}$$

$$I^{(1)} = I_1^{(1)} \cup I_2^{(1)}, \tag{3.13}$$

$$I^{(2)} = I_1^{(2)} \cup I_2^{(2)} \cup I_3^{(2)} \cup I_4^{(2)}, \tag{3.14}$$

$$\vdots \quad \vdots \tag{3.15}$$

We denote the length of an interval $I_i^{(n)}$ by $\varepsilon_i^{(n)}$.

Natural measure

A chaotic set consists of small pieces of different sizes. The natural measure characterizes how often each piece appears in a chaotic set. Let ε be the resolution to measure length. For example, if we choose $\varepsilon \sim \varepsilon^{(n)} < \varepsilon_1^n$, we can measure the length of an interval $I_i^{(n)}$ with good precision. We denote, by $N_i(\varepsilon)$, the minimum number of small boxes with length ε necessary to cover the interval $I_i^{(n)}$, and by $N(\varepsilon)$ to cover the whole set $I^{(n)}$. The natural measure is defined by

$$P_i(\varepsilon) = \frac{N_i(\varepsilon)}{N(\varepsilon)}. \tag{3.16}$$

In the case of the gluttonous baker map (3.11),

$$P_i(\varepsilon^{(n)}) = \frac{\varepsilon_i^{(n)}}{(\varepsilon_1 + \varepsilon_2)^n}. \tag{3.17}$$

Escape rate

The escape rate characterizes how quickly randomly selected initial conditions escape from a chaotic set. It is defined at late time by

$$(\text{chaotic sets}) \sim e^{-\kappa n}. \tag{3.18}$$

In the case of the gluttonous baker map (3.11), it is given by

$$(\varepsilon_1 + \varepsilon_2)^n \sim e^{-\kappa n}, \tag{3.19}$$

or equivalently

$$\varepsilon_i^{(n)} e^{\kappa n} \sim P_i(\varepsilon^{(n)}). \tag{3.20}$$

Then we find that

$$\kappa = -\ln(\varepsilon_1 + \varepsilon_2). \tag{3.21}$$

Box counting dimension

The fractality of a given set is measured by fractal dimension, which is a generalization of the ordinary dimension. One way to measure a dimension is to count the number of boxes which cover a set. Suppose that a given set is embedded in a d-dimensional space. Let $N(\varepsilon)$ be the minimum number of small boxes with length ε necessary to cover the set. For sufficiently small ε, the box counting dimension is defined by

$$N(\varepsilon) \sim \left(\frac{1}{\varepsilon}\right)^{D_0}. \tag{3.22}$$

This definition is a generalization of an ordinary dimension since d dimensional spaces satisfy $D_0 = d$. Rearranging it we can write also as

$$D_0 = \frac{\ln N(\varepsilon)}{-\ln \varepsilon}, \tag{3.23}$$

for the limit $\varepsilon \to 0$. Noting that the Cantor set generated by (3.11) has a strict self-similar structure,

$$\begin{aligned} \left(\frac{1}{\varepsilon}\right)^{D_0} &\sim N(\varepsilon) = \sum_i N_i(\varepsilon) \\ &= \sum_i N(\varepsilon/\varepsilon_i) \\ &\sim \left(\frac{1}{\varepsilon/\varepsilon_i}\right)^{D_0}. \end{aligned} \tag{3.24}$$

Thus the box counting dimension is also determined by an equation

$$\sum_i \varepsilon_i^{D_0} = 1. \tag{3.25}$$

Information dimension

The information dimension is another type of generalization of the ordinary dimension. While we used identical boxes to define the box counting dimension, we may use boxes of different sizes to cover segments of different lengths and define an effective number of boxes to cover the whole set. An effective number of boxes can be counted by using information

$$I(\varepsilon) = -\sum_i P_i(\varepsilon) \ln P_i(\varepsilon). \tag{3.26}$$

Let us explain its meaning quickly. For example, consider a two-sided coin whose head or tail appears with the equal probability $\{P_i\} = \{1/2, 1/2\}$. Since the head and tail can be distinguished, we may say that the coin has a size two, and has 1-bit information. Indeed the information defined above satisfies $2 = e^I$. Next, consider a super unfair coin $\{P_i\} = \{1, 0\}$. Since the coin always shows its head, we may say that the coin has an effective size one, and has 0-bit information. Indeed $1 = e^I$ is satisfied. Thus the exponential of information can define an effective size of a system.

The information dimension is defined by

$$e^{I(\varepsilon)} \sim \left(\frac{1}{\varepsilon}\right)^{D_1}. \tag{3.27}$$

When the probability distribution is uniform, the effective number of boxes $e^{I(\varepsilon)}$ reduces to $N(\varepsilon)$. Rearranging it we can write as

$$D_1 = \frac{\ln e^{I(\varepsilon)}}{-\ln \varepsilon}, \tag{3.28}$$

for the limit $\varepsilon \to 0$. We can easily show that the information dimension is no greater than the box counting dimension

$$D_1 \leq D_0. \tag{3.29}$$

Noting that $-\ln \varepsilon \sim -\sum_i P_i(\varepsilon^{(n)}) \ln \varepsilon_i^{(n)}$ holds for sufficiently high resolution,

$$D_1 = \frac{-\sum_i P_i(\varepsilon^{(n)}) \ln P_i(\varepsilon^{(n)})}{-\sum_i P_i(\varepsilon^{(n)}) \ln \varepsilon_i^{(n)}}. \tag{3.30}$$

In the case of the gluttonous baker map (3.11), it is given by

$$\begin{aligned} D_1 &= \frac{-\frac{\varepsilon_1}{\varepsilon_1+\varepsilon_2} \ln \frac{\varepsilon_1}{\varepsilon_1+\varepsilon_2} - \frac{\varepsilon_2}{\varepsilon_1+\varepsilon_2} \ln \frac{\varepsilon_2}{\varepsilon_1+\varepsilon_2}}{-\frac{\varepsilon_1}{\varepsilon_1+\varepsilon_2} \ln \varepsilon_1 - \frac{\varepsilon_2}{\varepsilon_1+\varepsilon_2} \ln \varepsilon_2} \\ &= \frac{-\varepsilon_1 \ln \varepsilon_1 - \varepsilon_2 \ln \varepsilon_2 + (\varepsilon_1+\varepsilon_2) \ln(\varepsilon_1+\varepsilon_2)}{-\varepsilon_1 \ln \varepsilon_1 - \varepsilon_2 \ln \varepsilon_2}. \end{aligned} \tag{3.31}$$

Lyapunov exponent

The Lyapunov exponent characterizes how fast the deviation of initial conditions grows. Let us consider a small interval $\Delta_i^{(n)} \subset I_i^{(n)}$. Its expansion factor $\Lambda_{1i}(n)$ is given by

$$\frac{\Delta_i^{(n)}}{\Delta^{(0)}} \sim e^{\Lambda_{1i}(n)}. \tag{3.32}$$

The Lyapunov exponent is defined as the average of the local expansion factor by

$$\lambda_1 = \sum_i P_i(\varepsilon) \frac{\Lambda_i(n)}{n} = \sum_i P_i(\varepsilon^{(n)}) \frac{-\ln \varepsilon_i^{(n)}}{n}. \tag{3.33}$$

In the case of the gluttonous baker map (3.11), it is given by

$$\lambda_1 = -\frac{\varepsilon_1}{\varepsilon_1+\varepsilon_2} \ln \varepsilon_1 - \frac{\varepsilon_2}{\varepsilon_1+\varepsilon_2} \ln \varepsilon_2. \tag{3.34}$$

Topological entropy

The topological entropy characterizes how fast the original segments in a set are divided into smaller segments at each step. Let us allocate a sequence of symbols for each interval $I_i^{(n)}$.

For example, we can allocate as $\{I^{(0)}\} \to \{0\}$, $\{I_i^{(1)}\} \to \{0,1\}$, $\{I_i^{(2)}\} \to \{00,01,10,11\}, \ldots$. The topological entropy K_0 is defined by

$$(\#\text{allowed symbolic sequence}) \sim e^{K_0 n}. \tag{3.35}$$

In the case of the gluttonous baker map (3.11), each interval is divided into two smaller intervals at each step. Thus

$$K_0 = \ln 2. \tag{3.36}$$

Metric entropy

The metric entropy is a generalization of the topological entropy. We use an effective number of allowed symbolic sequences which is counted by the information $I(\varepsilon)$. The metric entropy is defined by

$$e^{-\sum_i P_i(\varepsilon^{(n)}) \ln P_i(\varepsilon^{(n)})} \sim e^{K_1 n}. \tag{3.37}$$

We can easily show that the metric entropy is no greater than the topological entropy

$$K_1 \leq K_0. \tag{3.38}$$

Relations

Chaos can be detected by fractality in the phase space as explained before in the gluttonous baker map. It can also be understood from relations between measures of chaos. From (3.20), (3.30), and (3.33), we find that the Lyapunov exponent is determined by fractal dimension as

$$\lambda_1 = \frac{\kappa}{1 - D_1}. \tag{3.39}$$

From (3.37), we find that the metric entropy is determined as

$$K_1 = \lambda_1 - \kappa = \lambda_1 D_1. \tag{3.40}$$

3.3 Chaos in scatterings

Classical scatterings on many disks are typically chaotic. When a particle is shot into a scattering region, it collides with the disks many times. Then the deviation of an initial condition, say, of the impact parameter grows exponentially. Within a finite time, a particle escapes from the scattering region. Then the chaos is transient.

We will see below that three-disk scatterings are chaotic while two-disk scatterings are not. This is because there is no folding mechanism in two-disk scatterings. The geometrical structure in a scattering region determines whether a scattering system is chaotic or not.

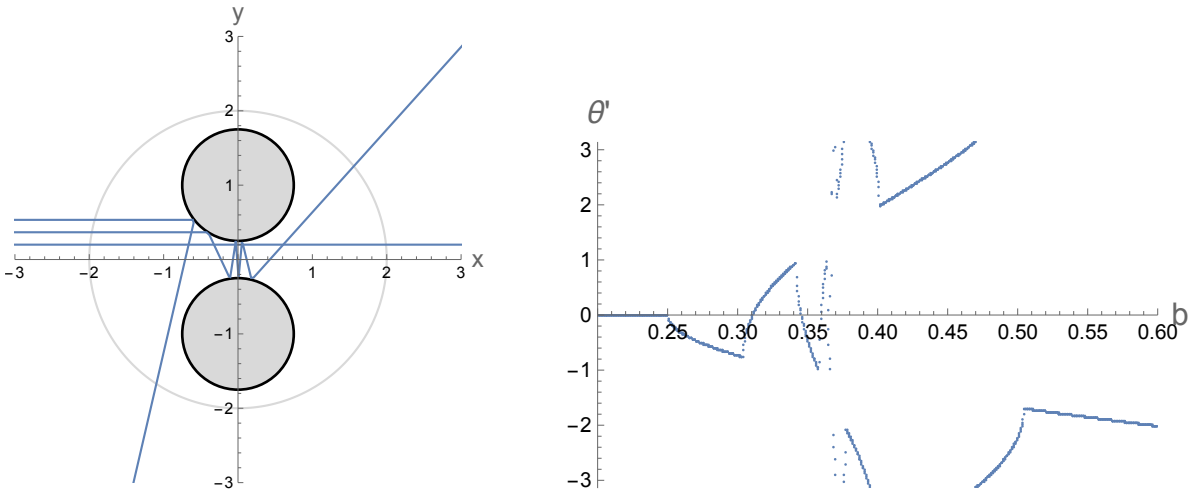

Figure 3: Classical two-disk scattering. The two disks with radius $r = 0.75$ are placed at $(x, y) = (0, \pm 1)$. The gray circle indicates a scattering region. Particles are shot from the left with impact parameter $b > 0$. They collide with disks and escape from the scattering region within a finite time. The right panel is a plot of scattering angle θ' with respect to impact parameter b. It is singular around $b_c \sim 0.37$; small segments are accumulated around $b = b_c$.

Scattering on disks

Let us consider a classical scattering on two disks as illustrated in the left panel of Fig. 3. We put two disks of radius $r = 0.75$ at $(x, y) = (0, \pm 1)$. A particle is shot from the negative x-axis with the impact parameter b. Its scattering angle θ' with respect to b is plotted in the right panel of Fig. 3.

As the figure shows, the scattering is irregular around a critical value $b_c \sim 0.37$. This is caused by an unstable periodic orbit: bounces between two disks along the y-axis. When the impact parameter is tuned around the critical value $b \sim b_c$, a particle bounces between the two disks many times. Since the bouncing orbit is unstable, a slight change of the impact parameter b discontinuously changes the scattering angle θ'. In this sense, scatterings by two disks stretch the deviation of initial conditions.

However, this system is not chaotic. Indeed, when we zoom into the plot, the number of small segments does not scale exponentially. Thus the plot cannot be fractal. The absence of fractality is clearer in the plot of the delay-time as shown in Fig. 4. From the plot, we can find a subset of all possible impact parameters for which a particle does not escape the scattering region no later than $T = T_c > 0$. This subset is analogous to a subset $I^{(n)} \subset I$ in the gluttonous baker map. Thus the subset of impact parameters is a fractal set if scatterings are chaotic. The plot is clearly not fractal. It just has a peak at $b \sim b_c$, which is caused by bounces of a particle between the two disks.

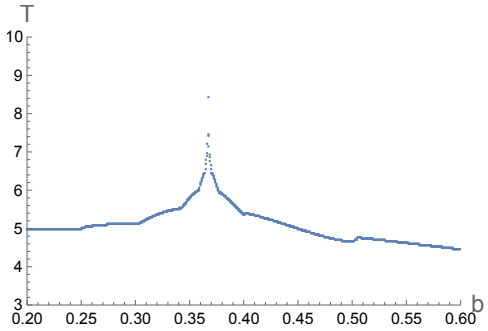

Figure 4: Escape time (or delay-time) with respect to impact parameter in two-disk scattering. The plot has a single peak at $b = b_c$ which corresponds to bounces between the two disks, thus it cannot be fractal.

Next, let us add another disk in the scattering region as illustrated in Fig. 5. We put three disks of radius $r = 0.75$ at $(x, y) = (-1/2, \pm\sqrt{3}/2), (1, 0)$. In this system, a particle scattered by disks bounces back by another disk, and is confined in the scattering region for a longer time. Such bounces give the folding mechanism. Then the scattering becomes chaotic. Indeed, the plot of the scattering angle in Fig. 5 is fractal. When we zoom into the plot, a similar structure re-appears and the number of small segments scales exponentially. Fractality is clearer in the plot of delay-time as shown in Fig. 6. When we zoom into the plot, a similar structure re-appears and the number of small segments scales exponentially.

Scattering on four-hill potential

Finally, we review particle scatterings by a four-hill potential and see that the scattering data, the plot of incoming/outgoing angles, has a fractal structure.

Consider the motion of a single particle scattered by a potential (see Fig. 7). A potential is localized around the origin of the space into which the particle is shot and then scattered to reach the spatial infinity. The scattering data could be, for example, the incoming angle θ and the impact parameter b for the initial state of the particle and the outgoing angle θ' and the impact parameter b' for the final state of the particle. Thus the data consists of a set of values (θ, b, θ', b') with many numerical experiments, for a fixed potential and fixed energy of the particle. In other words, the data is a set of functions $\theta'(\theta, b)$ and $b'(\theta, b)$.[21]

If one chooses a potential whose complexity is large enough, then it happens that the particle which was shot in can be trapped for a certain period of time and then escapes to the spatial infinity. During this trapping time, the particle is scattered many times by the

[21] One can choose $\theta = 0$ and ignore measuring b', then the scattering data is only $\theta'(b)$, which was used in [62].

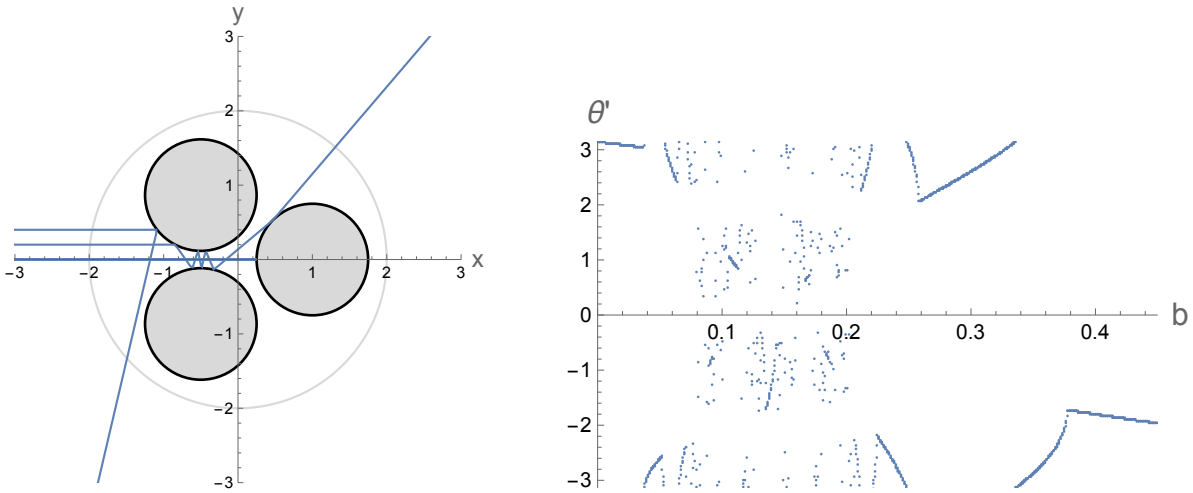

Figure 5: Classical three-disk scattering. Three disks with radius $r = 0.75$ are placed at $(x, y) = (-1/2, \pm\sqrt{3}/2), (1, 0)$. The gray circle indicates a scattering region. The right panel is a plot of scattering angle θ' with respect to impact parameter b. It is singular not only around a single value of b. Actually, there are infinitely many unstable periodic orbits.

inner structure of the potential and loses its initial information (which is θ and b). This causes chaos, the sensitivity to the initial condition.

In Fig. 7, two examples of the scattering of a particle which goes through the four-hill potential with the Lagrangian

$$L = \frac{1}{2}\dot{x}^2 + \frac{1}{2}\dot{y}^2 - x^2y^2e^{-x^2-y^2} \tag{3.41}$$

are presented. The particle is shot from the right hand side with the initial angle $\theta = 0.125$ and 0.127 respectively, with $b = 0$. The outcome is drastically different, although the initial conditions differ just slightly.

Generic scattering processes are different from the case of the bounded systems for which the standard definition of chaos applies: one cannot measure the chaos for infinite duration of time, because the particle can escape from the chaotic region. Therefore the chaotic nature is hidden in the scattering data of the particle which goes through the potential.

In Fig. 8, the scattering data of the particle which goes through the four-hill potential (3.41) is presented. We have chosen $b = 0$ for simplicity, and look at only the function $\theta'(\theta)$. The top-left panel is the whole view of the data. The scattering data obviously finds a lot of jumps, and in particular, the jumps are accumulated to form a dense part. If one magnifies the dense part, as seen in the other panels, one finds a similar dense structure in the scattering data. This is the fractal-like structure, which shows the transient chaos of the scattering process.

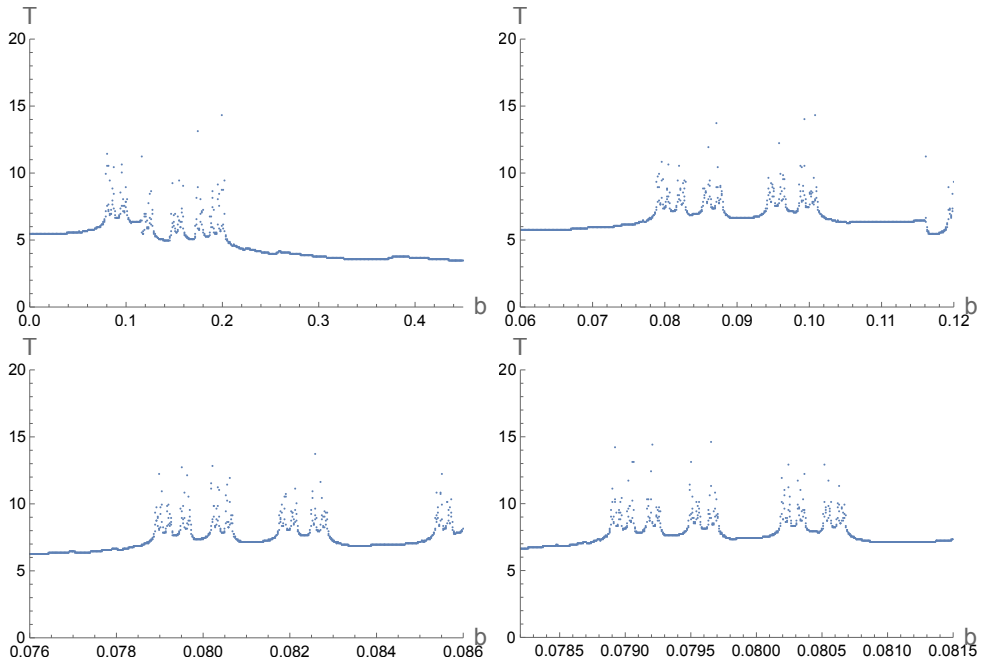

Figure 6: Escape time (or delay-time) with respect to impact parameter in three-disk scattering. When we zoom into the plot, a similar structure re-appears and the number of small segments scales exponentially. Thus the plot is fractal.

The existence of the fractal structure means that a single destination of the particle motion can have two or more paths. It is nothing but the initial condition sensitivity, that is the definition of classical chaos.

In summary, for classical scattering, there are two diagnoses for chaos: the fractal structure in the scattering data $\theta'(\theta)$ and the non-trivial geometrical structure in the scattering region. In the followings section, we obtain scattering data and a picture of a scattering region for string scatterings, in particular highly excited strings, and look for chaos.

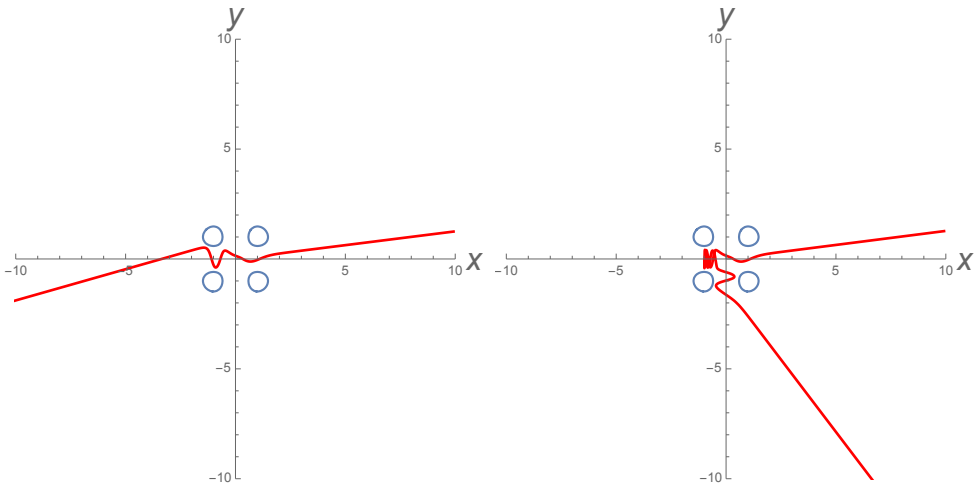

Figure 7: The classical scattering of a single particle in two spatial dimensions. The scattering potential is the four-hill potential (3.41) whose equal-height slice is plotted as four circles. Left: Initial condition is $\theta = 0.125$ with $b = 0$. Right: Initial condition is $\theta = 0.127$ with $b = 0$. For both plots, the energy is fixed to $E = 0.045$.

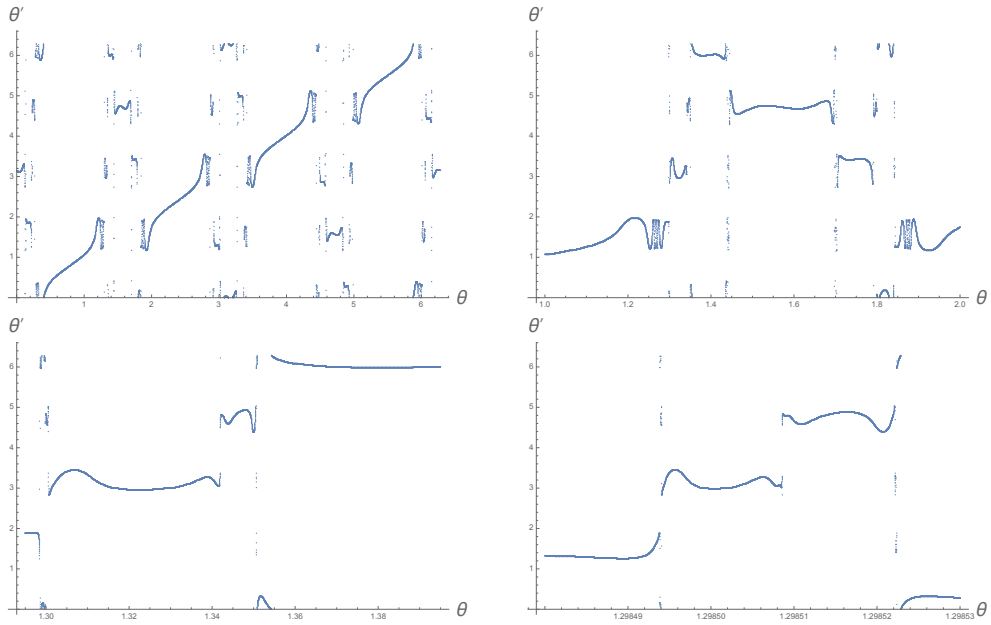

Figure 8: The scattering data of the particle for the four-hill potential model (3.41). The particle energy is fixed to $E = 0.045$, and the impact parameter is also fixed to $b = 0$. Top-left: the whole view of the scattering data $\theta'(\theta)$. The top-right, bottom-left, bottom-right panels are the magnified plots of the scattering data, while the top-left panel is the whole view of the scattering data. In the top-left panel, one finds connected lines and scattered plots. Interestingly, also in the magnified plots in the top-right, bottom-left and bottom-right panels, one finds a similar structure. This is the fractal-like structure of the self-similarity.

4 Fractal structure in string scattering data

In this section, we look for a fractal structure in scattering data of a highly excited string (HES). First of all, we generalize an idea of classical chaotic scatterings to quantum scatterings. Then we compute scattering amplitudes of HES-tachyon to HES-tachyon.

Our results show that the scattering amplitude is highly erratic. However, we could not find any fractal structure, which is necessary for chaos. Finally, we discuss the possibility that chaos shows up if we include higher loop corrections.

4.1 Generalization to quantum scattering

The transient chaos in classical scattering is well-understood, as we have reviewed in the previous subsection. However, string theory is built out of quantum scattering amplitudes. How can we generalize the classical analysis to the quantum scattering amplitudes? Here, let us explain our strategy to apply the transient chaos analysis for classical scattering processes which we reviewed in the previous subsection to the quantum scattering processes.

First of all, we need to note that in quantum scattering processes, due to the Heisenberg uncertainty principle, we do not have all the information which the classical scattering has. Thus here we start with a discussion on what parameters are suitable for the quantum scattering processes.

The quantum scattering in standard quantum field theories is normally described by plane waves, as any particle state is a superposition of quantized plane waves. This means that, the initial state and the final state are specified only by the momenta of all the particle states, incoming and outgoing. They are the parameters for quantum scattering, and we can further reduce the number of the independent parameters by considering some limit, as follows.

In the analogy of the physical set-up of the transient chaos in classical scattering, we suppose a scattering of a light particle by a potential. In the standard 2-to-2 scattering processes in quantum field theories, this potential scattering is realized if one requires a limit where the other particle is much heavier than the light scattered particle. Thus, in this limit, what specifies the scattering amplitude is only the combination $(p_\mu^{(\mathrm{ini})}, p_\mu^{(\mathrm{fin})})$, which is the momenta of the light scattered particle. Furthermore, once we specify the mass m of the light particle, then with the energy conservation, we find $p_0^{(\mathrm{ini})} = p_0^{(\mathrm{fin})} = \sqrt{p^2 + m^2}$ for the momentum magnitude p (> 0). The scattering is specified by p and the pair (θ, θ') where θ and θ' are the angles of the incoming and the outgoing momenta $(p_i^{(\mathrm{ini})}, p_i^{(\mathrm{fin})})$. Thus, the scattering data is given by the scattering amplitude $\mathcal{A}(p, \theta, \theta')$.

Next, we present our procedures to extract the scattering plot similar to Fig. 8 from the quantum scattering amplitudes, to find the transient chaos of the system. Note that the

classical scattering data is given by a map $(b, \theta) \to (b', \theta')$ for a given energy, where b is the impact parameter. In the quantum scattering we consider plane waves, meaning that the impact parameters are uniformly integrated. Once the impact parameter dependence is integrated, the classical scattering is specified by a map $\theta \to \theta'$, *i.e.* a function $\theta'(\theta)$ for a given energy.

We can relate this classical scattering data $\theta'(\theta)$ and the quantum scattering amplitude $\mathcal{A}(p, \theta, \theta')$ as follows. The absolute square of the scattering amplitude $\mathcal{A}$ describes the probability. When the amplitude has a pole at some value of θ', we can say that the value is most probable in the scattering. Since the position of the pole depends also on the other data (p, θ), it gives θ' as an implicit function of (p, θ). When the amplitude has multiple poles at $\theta' = \theta'_m$ for given p and θ, as

$$\mathcal{A}(p, \theta, \theta') \sim \sum_m \frac{R_m(p, \theta)}{\theta' - \theta'_m(p, \theta)} \tag{4.1}$$

then we can say that the value $\theta'_m(p, \theta)$ which gives the largest residue $|R_m(p, \theta)|$ among all poles is the most probable scattering. In this manner, we can extract the function $\theta'(p, \theta)$, which is $\theta'_m(p, \theta)$ with the largest $|R_m(p, \theta)|$, from the scattering amplitude $\mathcal{A}(p, \theta, \theta')$, and regard $\theta'(p, \theta)$ as a quantum counterpart of the classical scattering data $\theta'(\theta)$.

Note that the obtained function $\theta'(p, \theta)$ can be discontinuous, since the largest pole, or equivalently the label m of the largest residue, may differ for different θ. In general, when there are multiple poles in the scattering amplitude, the scattering data $\theta'(\theta)$ for a given value of p, which is a single-valued, consists of a set of segment functions whose domains are disjoint with each other.

In the following part, we use this definition of $\theta'(\theta)$ for the scattering data of the string scattering amplitudes.

4.2 HES-tachyon to HES-tachyon scattering

We study a scattering of a tachyon by a highly excited string (HES) in open bosonic string theory:

$$\text{HES} + \text{tachyon} \to \text{HES} + \text{tachyon}. \tag{4.2}$$

We compute its scattering amplitude $\mathcal{A}(p, \theta, \theta')$, and find that it has multiple poles at $\theta' = \theta'_m(\theta)$. We regard the angle associated with the largest pole as a quantum counterpart of the classical scattering data. We show that the scattering data $\theta'(\theta)$ consists of disconnected segments, and look for the fractal structure.

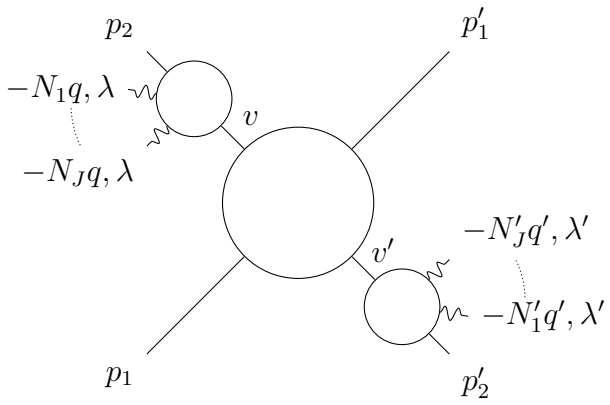

Figure 9: String amplitude for the process: (tachyon + J photons) + tachyon $\to$ (tachyon + J photons) + tachyon. The external lines on the left/right hand side are the incoming/outgoing strings. After picking out poles labeled with v, v', it describes the scattering of a tachyon by a highly excited string (HES).

4.2.1 Setups

To construct the HES-tachyon scattering amplitude, we start with a scattering:

$$(\text{tachyon} + J \text{ photons}) + \text{tachyon} \to (\text{tachyon} + J \text{ photons}) + \text{tachyon}. \tag{4.3}$$

Its diagram is shown in Fig. 9. The external lines on the left/right hand side are the incoming/outgoing strings. J photons have momenta $\{-N_a q\}_{a=1,\ldots,J}$ and the same polarization λ is shared by all the photons. The tachyon with momentum p_2 can form an intermediate HES state by absorbing all these J photons. By picking out a pole labeled with v, we focus on the HES state. A similar construction of a HES state has been used, for example, in [43, 44]. The HES scatters another incoming tachyon with momentum p_1. The outgoing strings are constructed in a similar but opposite processes. The incoming strings decay into an outgoing tachyon with momentum p_1' and a HES corresponding to a pole labeled with v'. The outgoing HES state is constructed from a tachyon with momentum p_2' and J photons which have momenta $\{-N_b' q'\}_{a=1,\ldots,J}$ and share the same polarization λ', or equivalently, the HES decays into a tachyon and J photons successively. The resulting amplitude with the poles v, v' extracted describes the desired process (4.2).

Let us summarize the setups and some assumptions to simplify computations. The momentum conservation law is

$$\begin{aligned} 0 &= p_1 + (p_2 - Nq) + (p_2' - N'q') + p_1' \\ &= p_1 + p_2 + p_2' + p_1' - N(q + q') \ , \end{aligned} \tag{4.4}$$

where

$$N = \sum_{a=1}^{J} N_a = \sum_{b=1}^{J} N'_b = N', \quad (N_a, N'_b \geq 1) \tag{4.5}$$

is the total excitation level of HES, and here, the total excitation number N' of the outgoing HES is taken to be the same as that (N) of the incoming HES. The mass M of HES is given in terms of the total excitation number N as

$$M^2 = 2(N-1). \tag{4.6}$$

Since all photons have the same polarization, the number of photons J equals to the total angular momentum. Here note that N'_b is not necessarily equal to N_b. The on-shell conditions for the tachyons and photons are

$$p_1^2 = p_2^2 = p_2'^2 = p_1'^2 = -(-2), \tag{4.7}$$

and

$$q^2 = q'^2 = 0, \tag{4.8}$$

respectively. For simplicity, we assume that $q \propto q'$ and $\lambda = -\lambda'$. Then the photon momenta and polarization vectors satisfy

$$\begin{aligned} &q \cdot q' = 0, \qquad\qquad \lambda^2 = \lambda'^2 = \lambda \cdot \lambda' = 0, \\ &q \cdot \lambda = q' \cdot \lambda' = q \cdot \lambda' = q' \cdot \lambda = 0. \end{aligned} \tag{4.9}$$

We also assume that

$$(p_1 + p_2) \cdot \lambda = (p'_1 + p'_2) \cdot \lambda' = 0 \tag{4.10}$$

for simplicity. This is satisfied without loss of generality, for example, by taking the center-of-mass frame of the incoming/outgoing strings. We define the Mandelstam(-like) variables as

$$s = -(p_1 + p_2 - Nq)^2 = -(p'_1 + p'_2 - N'q')^2, \tag{4.11}$$

$$t = -(p_1 + p'_2 - N'q')^2 = -(p'_1 + p_2 - Nq)^2, \tag{4.12}$$

$$u = -(p_1 + p'_1)^2 = -(p_2 - Nq + p'_2 - N'q')^2. \tag{4.13}$$

Also we define variables to describe the HES poles as

$$v = -(p_2 - Nq)^2, \tag{4.14}$$

$$v' = -(p'_2 - N'q')^2. \tag{4.15}$$

These satisfy an identity

$$s + t + u = 4 \cdot (-2) + 2 \cdot (1 + v/2) + 2 \cdot (1 + v'/2). \tag{4.16}$$

4.2.2 Amplitude and its largest pole

Here, we calculate the HES-tachyon to HES-tachyon amplitude. The amplitude becomes a four point amplitude after picking out the intermediate HES poles of v- and v'-channels, and is given in the form of a worldsheet boundary integral over the position of one of four vertex operators which cannot be fixed by the conformal symmetry. The integral can be split into three segments. The amplitude contains poles of three channels: s-, t- and u-channels, and each of three segments of the integral contains contributions from two of three channels. Here, we focus on the segment of integral $\mathcal{A}_{st}$ which contains contributions of s- and t-channels.[22]

Some straightforward computations in App. A show that the st-part contribution for the HES-tachyon to HES-tachyon scattering amplitude is

$$\mathcal{A}_{st} \sim \sum_{\{i_a=2,2'\}} \sum_{\{j_b=2,2'\}} \sum_{\{k_a=0\}}^{\{N_a\}} \sum_{\{l_b=0\}}^{\{N'_b\}} \left(\prod_{a=1}^{J} (p_{i_a}\cdot\lambda)\, c_{k_a}^{(i_a)}\right)\left(\prod_{b=1}^{J} (p_{j_b}\cdot\lambda')\, d_{l_b}^{(j_b)}\right) B(-\alpha(s)+k+l,-\alpha(t)). \quad (4.17)$$

Here the coefficients $c_k^{(i)}, d_l^{(j)}$ are defined by

$$c_k^{(2)} = +c_k(\alpha_2+1,\alpha_1+1,\alpha'_2), \quad (4.18)$$

$$c_k^{(2')} = -c_{k-1}(\alpha_2,\alpha_1,\alpha'_2+1), \quad (4.19)$$

$$d_l^{(2)} = -c_{l-1}(\beta'_2,\beta'_1,\beta_2+1), \quad (4.20)$$

$$d_l^{(2')} = +c_l(\beta'_2+1,\beta'_1+1,\beta_2), \quad (4.21)$$

where

$$c_k(\alpha_2,\alpha_1,\alpha'_2) = \frac{\Gamma(-\alpha_2+1)\Gamma(-\alpha_1+1)}{\Gamma(-\alpha_2-\alpha_1+2)}\frac{\Gamma(\alpha'_2+k)}{\Gamma(\alpha'_2)}\frac{\Gamma(-\alpha_2+1+k)}{\Gamma(-\alpha_2+1)}\frac{\Gamma(-\alpha_2-\alpha_1+2)}{\Gamma(-\alpha_2-\alpha_1+2+k)}\frac{1}{\Gamma(k+1)}, \quad (4.22)$$

and

$$\alpha_i = -(-N_a q)\cdot p_i, \quad \beta_j = -(-N'_b q')\cdot p_j. \quad (4.23)$$

The last factor $B(-\alpha(s)+k+l,-\alpha(t))$ in (4.17) is the Beta function

$$B(x,y) = \frac{\Gamma(x)\Gamma(y)}{\Gamma(x+y)}, \quad (4.24)$$

[22]The part $\mathcal{A}_{st}$ originates in the DDF construction of the fourth vertex operator going around one of the other three vertex operators, see App. A for the details. Although this is a part of the whole scattering amplitude, we assume that this is enough for looking at any possible fractal structure. In fact, the complete structure of the Veneziano amplitude is determined solely by $\mathcal{A}_{st}$.

and k, l and α are defined by

$$\alpha(x) = 1 + x/2, \qquad k = \sum_{a=1}^{J} k_a, \qquad l = \sum_{b=1}^{J} l_b. \tag{4.25}$$

To evaluate the amplitude (4.17), we have taken the following parameterization of the momenta and polarization vectors,

$$\begin{aligned}
&-q = \tfrac{1}{\sqrt{2(N-1)+p^2}-p\cos\theta}\begin{pmatrix}1\\0\\0\\-1\end{pmatrix}, \quad -(-q') = \tfrac{1}{\sqrt{2(N-1)+p^2}-p\cos\theta'}\begin{pmatrix}1\\0\\0\\-1\end{pmatrix}, \\
&\lambda = \tfrac{1}{\sqrt{2}}\begin{pmatrix}0\\1\\i\\0\end{pmatrix} \qquad\qquad -\lambda' = \tfrac{1}{\sqrt{2}}\begin{pmatrix}0\\1\\i\\0\end{pmatrix}, \\
&p_1 = \begin{pmatrix}\sqrt{p^2-2}\\p\sin\theta\\0\\p\cos\theta\end{pmatrix}, \qquad -p_1' = \begin{pmatrix}\sqrt{p^2-2}\\p\sin\theta'\cos\varphi'\\p\sin\theta'\sin\varphi'\\p\cos\theta'\end{pmatrix}, \\
&p_1+p_2-Nq = \begin{pmatrix}\sqrt{s}\\0\\0\\0\end{pmatrix}, \qquad -p_1'-p_2'+N'q' = \begin{pmatrix}\sqrt{s}\\0\\0\\0\end{pmatrix}.
\end{aligned} \tag{4.26}$$

Here, p stands for the magnitude of the momentum of the incoming tachyon, and the scattering amplitude is parametrized by the angles[23] θ, θ' and φ'. The Mandelstam(-like) variables are now expressed as

$$s = (\sqrt{2(N-1)+p^2} + \sqrt{p^2-2})^2, \tag{4.27}$$

$$t = (\sqrt{2(N-1)+p^2} - \sqrt{p^2-2})^2 - 2p^2(1+\cos\theta\cos\theta' + \sin\theta\sin\theta'\cos\varphi'), \tag{4.28}$$

$$u = -2p^2(1-\cos\theta\cos\theta' - \sin\theta\sin\theta'\cos\varphi'). \tag{4.29}$$

It is straightforward to check that these variables satisfy the identify (4.16). Also we easily

[23] In $2 \to 2$ scattering of scalar particles, one can take the center of mass frame with which the scattering angle is fixed. However, our HES has a specific spatial orientation which is its polarization. Our spherical coordinate system respects the polarization of the photons which are used to make the HES. There is no remaining rotation symmetry which could fix the angular variables.

find for (4.23) that

$$\begin{aligned} &p_1\cdot q=+\frac{\sqrt{2(-1)+p^2}+p\cos\theta}{\sqrt{2(N-1)+p^2}-p\cos\theta},\quad p_2\cdot q=+1,\quad p_2'\cdot q=-\frac{\sqrt{2(N-1)+p^2}-p\cos\theta'}{\sqrt{2(N-1)+p^2}-p\cos\theta},\\ &p_1'\cdot q'=+\frac{\sqrt{2(-1)+p^2}+p\cos\theta'}{\sqrt{2(N-1)+p^2}-p\cos\theta'},\quad p_2'\cdot q'=+1,\quad p_2\cdot q'=-\frac{\sqrt{2(N-1)+p^2}-p\cos\theta}{\sqrt{2(N-1)+p^2}-p\cos\theta'}, \end{aligned} \tag{4.30}$$

and for the coefficients in (4.17) that

$$p_2\cdot\lambda=-p_2\cdot\lambda'=\frac{-1}{\sqrt{2}}\,p\sin\theta, \tag{4.31}$$

$$p_2'\cdot\lambda'=-p_2'\cdot\lambda=\frac{-1}{\sqrt{2}}\,pe^{i\varphi'}\sin\theta'. \tag{4.32}$$

Under these parametrization, the HES-tachyon to HES-tachyon amplitude is given by the momentum and the incoming/outgoing angles $\mathcal{A}=\mathcal{A}(\{N_a\},\{N_b'\};p,\theta,\theta',\varphi')$.

We apply the strategy in Sec. 4.1 to this amplitude and find the largest pole, to extract the scattering data. Let us consider the amplitude for given excitation levels $\{N_a\},\{N_b'\}$ and magnitude of momentum p. Since the Mandelstam variable s depends only on the total excitation level N and magnitude of momentum p, the s-channel poles are independent of the angular variables. On the other hand, the t-channel poles come from the divergences of the Beta function in (4.17), and appear in certain outgoing angles for given incoming angles. The t-channel poles form a line in two-dimensional space of outgoing angles θ' and φ'. For a fixed φ', the positions of poles in the outgoing angle $\{\theta_m'(\theta)\}$ is given as functions of the incoming angle θ. They can be obtained by solving

$$\alpha(t(\theta,\theta'))=n,\quad n\in\mathbb{Z}_{\geq}, \tag{4.33}$$

as the t-channel poles come from the poles of $\Gamma(-\alpha(t))$ in the Beta function in (4.17). We evaluate this equation numerically. Among the data $\{\theta_m'(\theta)\}$, we look for their maximum poles, which has the largest residue of the poles. The residue around the poles is

$$\begin{aligned} \tilde{\mathcal{A}}_{st}&=\lim_{\alpha(t)\to n}\lim_{\{\alpha_2\}\to\{N_a\}}\lim_{\{\beta_2'\}\to\{N_b'\}}\frac{\sin\pi(-\alpha(t))}{\pi}\prod_{a=1}^{J}\frac{\sin\pi\alpha_2}{\pi}\prod_{b=1}^{J}\frac{\sin\pi\beta_2'}{\pi}\,\mathcal{A}_{st}\\ &=\mathcal{A}_{st}|_{B\to\tilde{B},c\to\tilde{c},d\to\tilde{d}}\,. \end{aligned} \tag{4.34}$$

Here we have defined

$$\begin{aligned} \tilde{B}(-\alpha(s)+k+l,-\alpha(t))&=\lim_{\alpha(t)\to n}\frac{\sin\pi(-\alpha(t))}{\pi}\,B(-\alpha(s)+k+l,-\alpha(t))\\ &=\frac{\Gamma(-\alpha(s)+k+l)}{\Gamma(-\alpha(s)-n+k+l)\Gamma(1+n)},\\ \tilde{c}_k(\alpha_2,\alpha_1,\alpha_2')&=\lim_{\alpha_2\to N_a}\frac{\sin\pi\alpha_2}{\pi}\,c_k(\alpha_2,\alpha_1,\alpha_2') \end{aligned} \tag{4.35}$$

$$= \frac{1}{\Gamma(k+1)\Gamma(\alpha_2-k)} \frac{\Gamma(\alpha_2-k+\alpha_1-1)}{\Gamma(\alpha_1)} \frac{\Gamma(\alpha_2'+k)}{\Gamma(\alpha_2')}, \tag{4.36}$$

and have also defined

$$\tilde{c}_k^{(2)} = -\tilde{c}_k(\alpha_2+1, \alpha_1+1, \alpha_2'), \tag{4.37}$$

$$\tilde{c}_k^{(2')} = -\tilde{c}_{k-1}(\alpha_2, \alpha_1, \alpha_2'+1), \tag{4.38}$$

$$\tilde{d}_l^{(2)} = -\tilde{c}_{l-1}(\beta_2', \beta_1', \beta_2+1), \tag{4.39}$$

$$\tilde{d}_l^{(2')} = -\tilde{c}_l(\beta_2'+1, \beta_1'+1, \beta_2). \tag{4.40}$$

Note that the signs of the coefficients $\tilde{c}^{(2)}, \tilde{d}^{(2')}$ are flipped since $\sin\pi(\alpha_2+1) = -\sin\pi\alpha_2$. Numerically evaluating the reside at $\{\theta_m'(\theta)\}$, and finding the largest one among them, we construct the scattering data $\theta'(\theta)$ of the HES-tachyon scattering amplitudes.

4.2.3 Transient chaos analysis of the scattering amplitude

In this subsection, we show numerical plots of the scattering data $\theta'(\theta)$ for various fixed parameters, and discuss their fractal feature (the self-similarity).

The results for a scattering of a tachyon and a HES with the angular momentum $J = 1$ are shown in Fig. 10. The top/middle/bottom two panels are the plots for the excitation levels $N = N_1 = N_1' = 1, 5, 9$. The three panels on the left and right hand side are the plots for $\varphi' = 0$ and $\varphi = \pi/4$, respectively. The momentum is fixed at $p = 2.6$ so that the energy squared is positive, $E^2 = p^2 - 2 \approx 7 - 2 > 0$.

The plots are highly erratic, for larger excitation levels. The tilted lines in the case $N = 1$ split into smaller segments in the cases $N = 5, 9$. However, we do not see any fractal structure. In particular, the number of the small segments does not increase exponentially in N. Note that typical fractal data is produced by a repeated action of an operation creating self-similar structure, and the number of small structure grows exponentially in the number of the action, thus also in our case, it is expected that the number of the smaller segments would have grown exponentially in N if the scattering were chaotic.

This is further confirmed in Fig. 11, where the excitation level is chosen as $N = 27$. This number $N = 27 \approx 4p^2$ was chosen so that as many t-channel poles, found in (4.33), appear as possible, nevertheless, the fractal feature, or the exponentially smaller structure, does not appear. Thus we conclude that the scattering data is not fractal. Assuming that the fractal nature is the sign of chaos in quantum systems, our result means that our HES-tachyon scattering is not chaotic.

The results for the scattering of the HES with $J > 1$ are shown in Fig. 12. The top, bottom-left and bottom-right panels are the plots for the excitation levels $\{N_a\} = \{N_b'\} = \{5\}$, $\{3, 1, 1\}, \{1, 1, 1, 1, 1\}$, respectively. Other parameters are fixed as $\varphi' = 0$, $p = 2.6$. As the

photons of which the HES with the total excitation level N consists are partitioned into more photons to form a HES with smaller excitation levels $\{N_a\}, \{N'_b\}$, we find in Fig. 12 that the small segments disappear. We conclude that even with the HES with $J > 1$ the fractal nature is not found, therefore, the scattering amplitudes are not chaotic.[24]

This behavior on the partitions is explained as follows. As seen from the examples of the case $J = 1$, the smaller segments appear for larger N (or N_a, N'_b). In the scattering amplitude, there exist several lines of poles. When we pick out the pole with the largest residue, the largest pole depends on the incoming angles. Thus, the line in the scattering data of the largest pole is segmented. This magnitude of the residue at each pole is mostly determined by the coefficients $c_k^{(i)}(\alpha), d_l^{(j)}(\beta)$, where α, β are proportional to N_a, N'_b times oscillating functions (see (4.23), (4.30)). These coefficients oscillate more rapidly for larger values of $\{N_a\}, \{N'_b\}$. Then, the largest pole frequently changes from a line to another, and then, the line of the largest pole is split into smaller segments. The minimum length of the segments is bounded by the maximum of $\{N_a\}, \{N'_b\}$.

From the reasons described above, we expect that a larger N and a change in J does not produce the fractal behavior. First of all, for the fractal structure the scattering data needs to have exponentially small segments. The smallness of the segments is bounded by the maximum of $\{N_a\}$, $\{N'_b\}$. Increasing N provides only linearly small segments, which does not help giving a fractal structure. Increasing J just lowers the maximum of $\{N_a\}$, $\{N'_b\}$ and thus reduces the fractalness. The complexity of the J-partitions of N is not related to the fractal nature.[25] This is the reason why the scattering data is not fractal.

4.3 Possible cases when chaos shows up

The absence of a fractal structure in the scattering data is a negative result for looking for chaos. Nevertheless, we have not yet excluded all possibilities. We can expect that chaos shows up when we include higher loop corrections for the following reasons.

If we regard the multiple scattering in classical transient chaos as multiple scattering in string theory, it could mean that we need to visit higher loop amplitudes. The scattering amplitudes which we have studied in this paper is the tree level scattering, which is of the order of the string coupling constant. However, the particle scattering by a fixed potential is a non-perturbative process in the sense that the scattering potential can be decomposed

[24]We have used the typical value of p so that the total energy is positive. Even with other values of p, the scattering data does not show the fractal structure.

[25]Note that the exponential growth of the number of states in string excitations is not related to the small segments in the scattering data. In some other setup of the amplitudes, this exponential growth might produce some chaotic behavior, though it does not in our case.

into its radial modes. Therefore, naively speaking, for a possible transient chaos, higher loop amplitudes would be necessary.

As a first guess, we can use the tree level scattering data given in Fig. 10, Fig. 11 and Fig. 12 to produce the multiple scattering. For example, we can use the function

$$\theta'(\theta) \tag{4.41}$$

and apply this map many times, as

$$\theta'(\theta'(\theta)), \cdots \tag{4.42}$$

This is an analogy of the popular baker map which produces chaos. Unfortunately, since the slope of the scattering data in the left panels of Fig. 10 and Fig. 11 and in Fig. 12 is identical to 1, this map does not work to magnify a part of the scattering data (which is necessary for any chaotic map). While at this stage, our naive multiple application of the scattering data map does not seem to produce chaos, the slope of some parts of the scattering data with $\varphi' = \pi/4$ exceeds 1. The measure analysis is necessary to figure out whether the map can generate chaos or not.

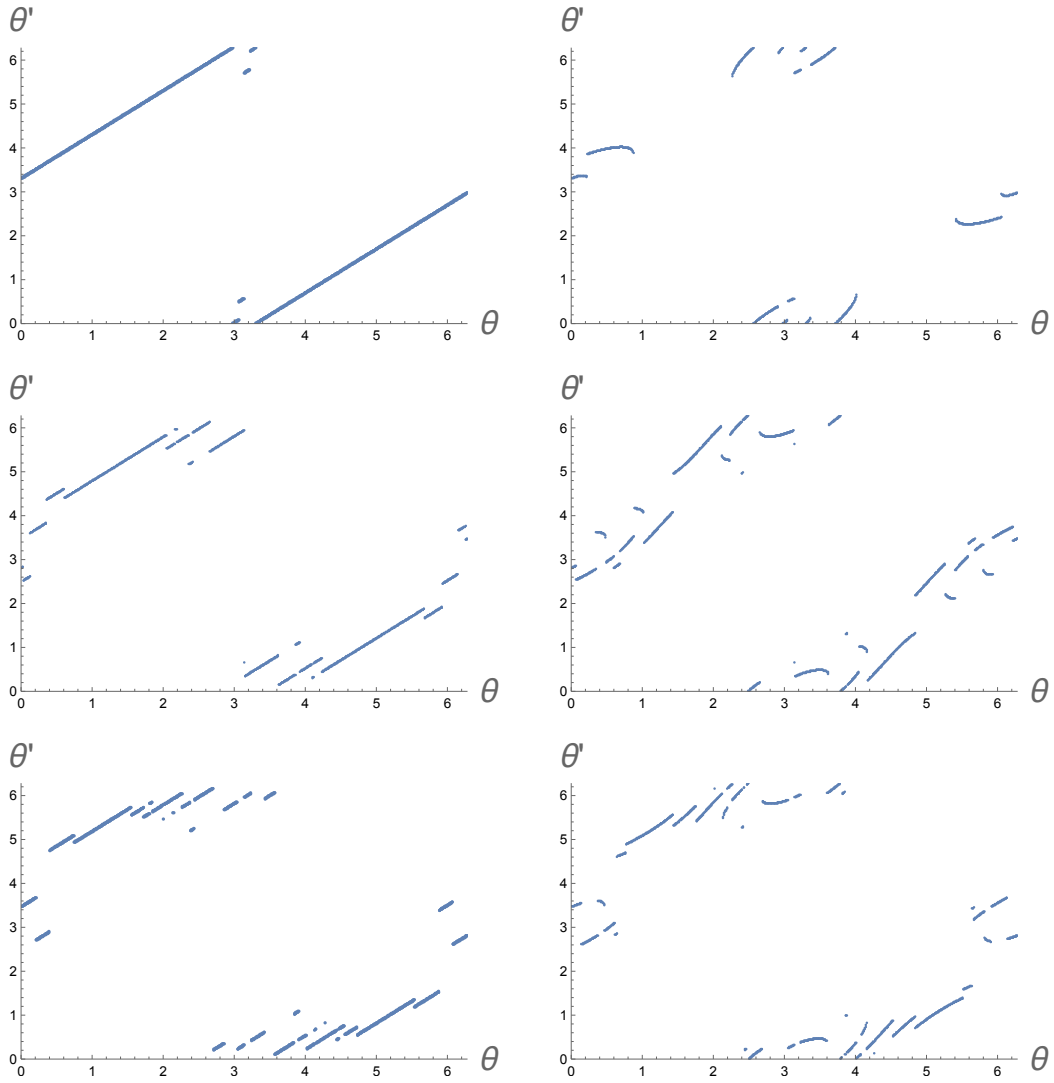

Figure 10: Scattering data $\theta'(\theta)$ involving a HES with the angular momentum $J = 1$. The top/middle/bottom two panels are the plots when the excitation level is $N = N_1 = N_1' = 1, 5, 9$. The three panels on the left/right hand side are the plots when $\varphi' = 0, \pi/4$. The momentum is fixed at $p = 2.6$. Although the plots are highly erratic, fractal structure has not been observed.

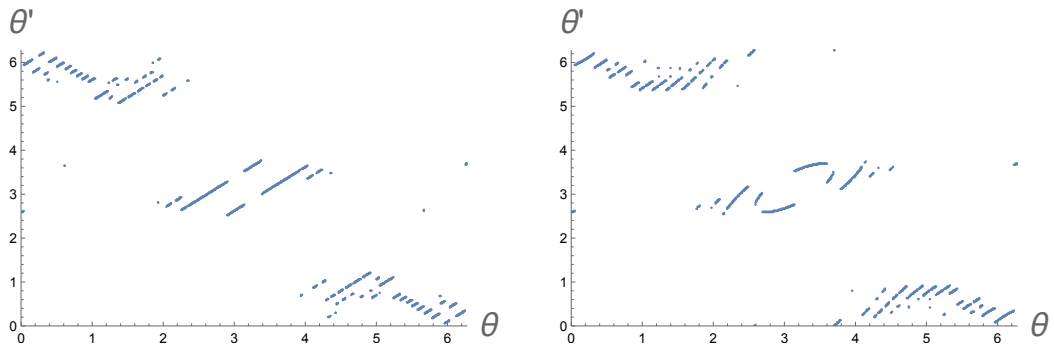

Figure 11: Scattering data $\theta'(\theta)$ when $J = 1, N = 27$. The excitation level is chosen so that as many t-channel poles appear as possible. Other parameters are fixed as Fig. 10. Still fractal structure does not appear.

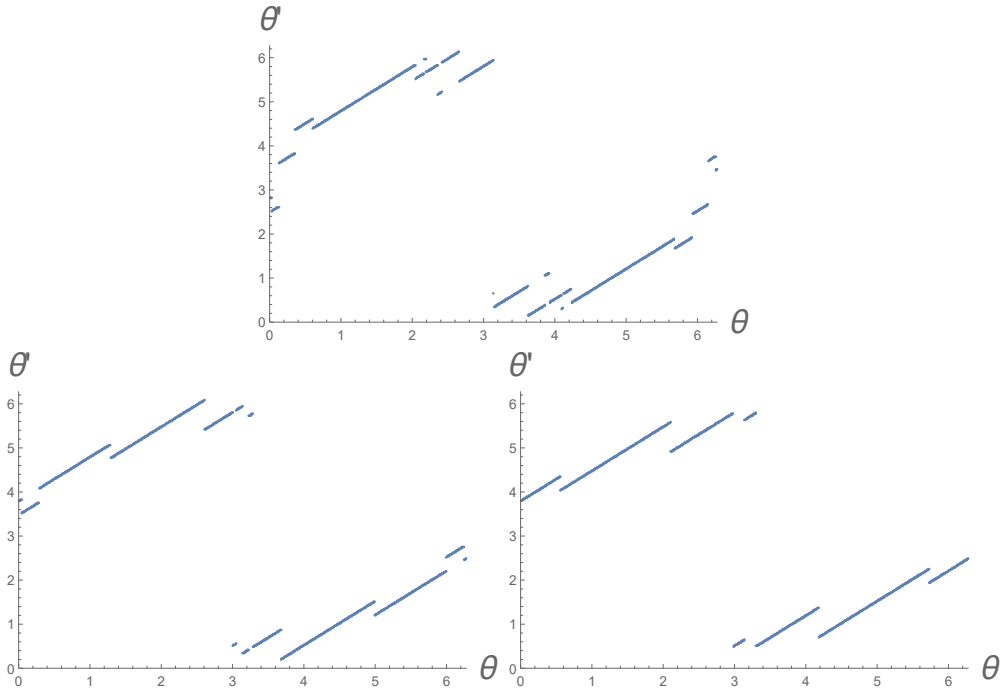

Figure 12: Scattering data $\theta'(\theta)$ involving a HES with the angular momentum $J > 1$. The top/bottom-left/bottom-right panels are the plots when the excitation level is $\{N_a\} = \{N'_b\} = \{5\}, \{3, 1, 1\}, \{1, 1, 1, 1, 1\}$. Other parameters are fixed as $\varphi' = 0, p = 2.6$. As the level N is partitioned into smaller numbers $\{N_a\}, \{N'_b\}$, the small segments disappear.

5 Geometrical structure in string scattering region

In this section, we study the geometrical structure of string scattering regions. We employ an imaging method: Fourier transformation of scattering amplitudes. First of all, we check that our method appropriately works in the standard double-slit experiment. Then we show that string scattering regions look like double-slits. It can be explained analytically; the zeros of string amplitudes coincide with the ones of the standard double-slit experiment. We may interpret the slits in string images as the end points of strings.

We could not find any non-trivial geometrical structure, which is necessary for chaos, since the slits are aligned along the same straight line. We discuss the possibility that chaos shows up if we consider closed strings or multi-point scatterings.

5.1 Double-slit experiment

First of all, we review the standard double-slit experiment, and a method to reconstruct the image from the amplitude on a screen, to demonstrate that the amplitudes actually encode the image of the double slit.

Let us put two slits S_1, S_2 on $(z, x) = (\pm l/2, 0)$, and place the center of a spherical screen of redius $L \gg l$ at the origin. A wave with wavelength $\lambda_{\rm ds}$ passes through the slits from the negative to the positive x-direction. An observer P is placed at $(z, x) = (L\cos\theta', L\sin\theta')$ on the screen. See Fig. 13.

If the screen is sufficiently large, *i.e.* $L \gg l$, the difference of two optical paths is given by

$$\overline{\mathrm{S_2P}} - \overline{\mathrm{S_1P}} \simeq l\cos\theta'. \tag{5.1}$$

Thus the condition that the amplitude at P vanishes is

$$\cos\theta' \simeq \frac{k'}{2}\frac{\lambda_{\rm ds}}{l} \tag{5.2}$$

where k' is an odd integer. More precisely, supposing that a spherical wave is emitted from the two slits with identical phase and amplitude A, the wave amplitude on the sphere placed at the spatial infinity $L(\gg l)$ is

$$\mathcal{A}(\theta', \varphi') \simeq 2A\cos\left(\frac{\pi l}{\lambda_{\rm ds}}\cos\theta'\right). \tag{5.3}$$

Zeros of this amplitude is given by (5.2). The result is independent of another spherical coordinate φ' as the slits are separated along the z-axis in this case.

The wave amplitude itself does not give the image of the slit, as understood in Fig. 14. Optical wave theory provides a method for the imaging. The popular method is just to put a

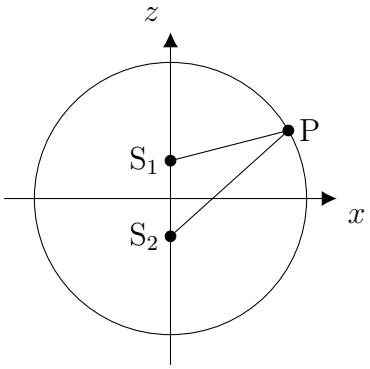

Figure 13: Double-slit is put at S_1 and S_2, and scattered wave is observed at the point P.

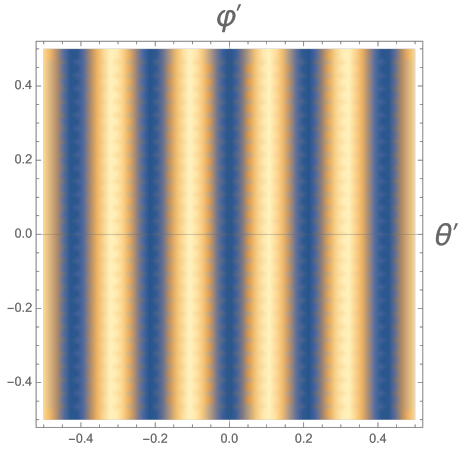

Figure 14: The amplitude of waves in the double slit experiment, for $\pi l/\lambda_{\rm ds} = 15$.

lens of a finite size d on the celestial sphere, and convert the wave amplitude with the frequency $\omega = 2\pi/\lambda_{\rm ds}$ into the image on a virtual screen located at a focal point of the lens. The formula for converting the amplitude to the image is approximated just by a Fourier transformation for $L \gg l$ (see [58, 59] for more details and brief reviews of the formula):

$$I(X,Y) = \frac{1}{(2d)^2 \sin\theta'_0} \int_{\theta'_0-d}^{\theta'_0+d} d\theta' \int_{\varphi'_0-d/\sin\theta'_0}^{\varphi'_0+d/\sin\theta'_0} d\varphi' e^{i\omega((\theta'-\theta'_0)X+(\varphi'-\varphi'_0)Y)} \mathcal{A}(\theta',\varphi'). \tag{5.4}$$

Here the coordinate (X, Y) is the one on the virtual screen placed behind the lens, so the image I of the optical wave is produced on that XY-plane. The location of the center of the lens is at $(\theta', \varphi') = (\theta'_0, \phi'_0)$, and a rectangular shape of the lens region is adopted for computational simplicity.

The lens size d needs to cover at least several zeros of the amplitude to find a sharp image, otherwise the image is blur and no structure can be reconstructed from the amplitude. In the present case of the double-slit experiment, when one takes the limit $l \gg \lambda_{\rm ds}$ the zeros of the

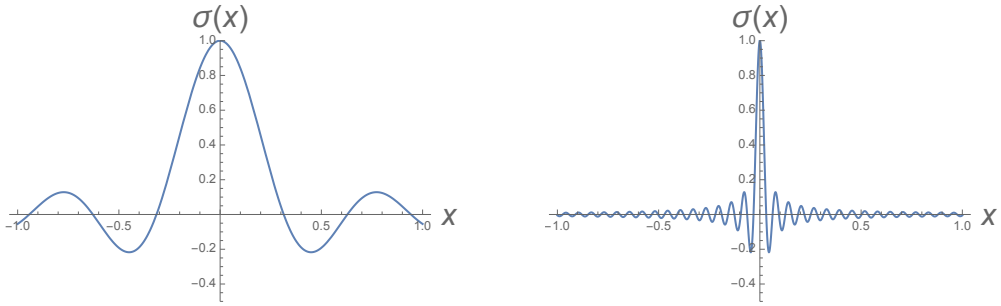

Figure 15: The lens resolution, seen in the behavior of the function $\sigma(x)$ (5.6), for $2\pi d/\lambda_{\rm ds} = 10$ (left) and for $2\pi d/\lambda_{\rm ds} = 100$ (right). For large $d/\lambda_{\rm ds}$ (meaning that the wave length is small enough so that it detects many oscillations of the amplitude), this function is highly peaked at $x = 0$, and the resolution is high.

amplitude are aligned densely, so the lens size d can be taken quite small compared to 2π. It means that the curvature effect of the celestial sphere in the imaging can be ignored and the formula (5.4) is validated.

Let us substitute the double-slit amplitude (5.3) into the imaging formula (5.4) and check if the image reproduces the shape (location) of the slits. The result is

$$I(X,Y) = A(-1)^{\tilde{k}}\sigma(Y/\sin\theta_0')\left(\sigma\left(X - \frac{l\sin\theta_0'}{2}\right) + \sigma\left(X + \frac{l\sin\theta_0'}{2}\right)\right) \tag{5.5}$$

where we have defined

$$\sigma(x) \equiv \frac{\sin\left(\frac{2\pi d}{\lambda_{\rm ds}}x\right)}{\frac{2\pi d}{\lambda_{\rm ds}}x}. \tag{5.6}$$

See Fig. 15 for the meaning of this function $\sigma(x)$. The calculation is straightforward but we have just assumed that the center of the location of the lens satisfies the condition

$$\frac{l}{\lambda_{\rm ds}}\cos\theta_0' = \tilde{k} \in \mathbf{Z} \tag{5.7}$$

to simplify the result. It can be met easily because we can find such an integer in the limit $l \gg \lambda_{\rm ds}$ which we took as described above.

The density plots of the image function (5.5) are shown in Fig. 16. One clearly finds the position of the double slits. The parameters are chosen as: $2\pi d/\lambda_{\rm ds} = 30$ and $l = 1$. The left figure is the image of the lens put at $(\theta_0', \varphi_0') = (\pi/2, 0)$. The location $\theta_0' = \pi/2$ means that the lens is put at the right hand side in Fig. 13, facing the double slits head-on, and the distance between the images of the two slits should be the largest. On the other hand, when the location of the viewer is shifted in the z direction in Fig. 13, the distance between

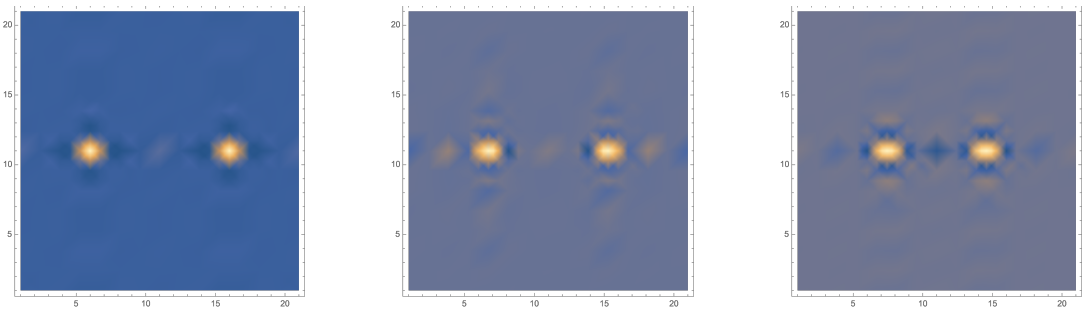

Figure 16: The X-Y images of the double-slit experiment, reconstructed from the wave amplitudes at the spatial infinity. Left: seen from the head-on point $(\theta_0', \varphi_0') = (\pi/2, 0)$ facing the aligned slit. Middle: $(\theta_0', \varphi_0') = (\pi/3, 0)$. Right: $(\theta_0', \varphi_0') = (\pi/4, 0)$. As the viewer shifts from the head-on point, the distance between the slits decreases by the function $\sin\theta_0'$ consistently.

the images of the slits should decrease. In fact, as seen in the middle and the right figures in Fig. 16, for $(\theta_0', \varphi_0') = (\pi/3, 0)$ and for $(\theta_0', \varphi_0') = (\pi/4, 0)$ respectively, one finds a consistent behavior.

In the next part, we apply this method for string scattering amplitudes, and see the images of the fundamental string.

5.2 Images of string via Veneziano amplitude

In this part, we obtain the images of a fundamental string by using the Veneziano amplitude, and show that the fundamental string is a double-slit.

More specifically, we point out that the zeros of the Veneziano amplitude match the ones of the double-slit amplitude described in the previous Sec. 5.1. Then we reconstruct images of a string by the Fourier transformation of the Veneziano amplitude. The images show two columns (which are "slits") standing apart at a distance of a typical length of strings.

5.2.1 Veneziano amplitude and its zeros

First, we describe our notation of the Veneziano amplitude, tachyon-tachyon to tachyon-tachyon scattering amplitude.

We label its four vertices with $1, 2, 2', 1'$. The momentum conservation law is

$$0 = p_1 + p_2 + p_2' + p_1'. \tag{5.8}$$

Since each vertex is a tachyon, we have the on-shell condition

$$p_1^2 = p_2^2 = p_2'^2 = p_1'^2 = -(-2). \tag{5.9}$$

Here, we conventionally chose $\alpha' = 1/2$. In the following computations, we will use the same unit. The Mandelstam variables are defined as

$$s = -(p_1 + p_2)^2 = -(p_1' + p_2')^2, \tag{5.10}$$
$$t = -(p_1 + p_2')^2 = -(p_1' + p_2)^2, \tag{5.11}$$
$$u = -(p_1 + p_1')^2 = -(p_2 + p_2')^2. \tag{5.12}$$

These satisfy an identity

$$s + t + u = 4 \cdot (-2). \tag{5.13}$$

The Veneziano amplitude [63] is given by

$$\mathcal{A}^{\mathrm{Ven}} = 2\left[\mathcal{A}_{st}^{\mathrm{Ven}} + \mathcal{A}_{tu}^{\mathrm{Ven}} + \mathcal{A}_{us}^{\mathrm{Ven}}\right], \tag{5.14}$$

where

$$\mathcal{A}_{xy}^{\mathrm{Ven}} = \frac{\Gamma(-\alpha(x))\Gamma(-\alpha(y))}{\Gamma(-\alpha(x) - \alpha(y))}, \quad \alpha(x) = 1 + x/2. \tag{5.15}$$

The amplitude has s-channel poles at $s = 2n$ for integers $n \geq -1$. Since we are interested in the images of a string formed at the scattering, we pull out one of the s-channel poles and look at the residue of the pole of the Veneziano amplitude. Using the reflection formula of the Gamma function and the identity (5.13), the residue of the s-channel pole is

$$\begin{aligned}\tilde{\mathcal{A}}_s^{\mathrm{Ven}} &= \lim_{s\to 2n} \frac{\sin\pi(-1 - s/2)}{\pi} \left(\mathcal{A}_{st}^{\mathrm{Ven}} + \mathcal{A}_{us}^{\mathrm{Ven}}\right) \\ &= \frac{1}{\Gamma(2+n)}\left[\frac{\Gamma(-1 - t/2)}{\Gamma(-2 - n - t/2)} + (t \leftrightarrow u)\right] = \frac{1}{\Gamma(2+n)}\left[\frac{\Gamma(-1 - t/2)}{\Gamma(2 + u/2)} + (t \leftrightarrow u)\right].\end{aligned} \tag{5.16}$$

To evaluate this amplitude, we denote the magnitude of the momentum of the in-coming tachyons is p. In the center-of-mass frame, the momenta can be generically parametrized as

$$\begin{aligned} p_1 &= \begin{pmatrix} \sqrt{p^2 - 2} \\ p\sin\theta \\ 0 \\ p\cos\theta \end{pmatrix}, \qquad -p_1' = \begin{pmatrix} \sqrt{p^2 - 2} \\ p\sin\theta'\cos\varphi' \\ p\sin\theta'\sin\varphi' \\ p\cos\theta' \end{pmatrix}, \\ p_2 &= \begin{pmatrix} \sqrt{p^2 - 2} \\ -p\sin\theta \\ 0 \\ -p\cos\theta \end{pmatrix}, \qquad -p_2' = \begin{pmatrix} \sqrt{p^2 - 2} \\ -p\sin\theta'\cos\varphi' \\ -p\sin\theta'\sin\varphi' \\ -p\cos\theta' \end{pmatrix}. \end{aligned} \tag{5.17}$$

The parameter θ, which measures the angle of the incoming tachyon against the z-axis, will be fixed later for the convenience in numerical computations. Under this parametrization, the Mandelstam variables are expressed as

$$s = 4(p^2 - 2) = 2n, \tag{5.18}$$

$$t = -2p^2(1 + \cos\theta\cos\theta' + \sin\theta\sin\theta'\cos\varphi'), \tag{5.19}$$

$$u = -2p^2(1 - \cos\theta\cos\theta' - \sin\theta\sin\theta'\cos\varphi'). \tag{5.20}$$

Let us look for zeros of the residue of the s-channel pole of the amplitude (5.16). It is zero if and only if

$$\begin{aligned} 0 &= \Gamma(-1 - t/2)\Gamma(2 + t/2) + (t \leftrightarrow u) \\ &= \frac{\pi}{\sin\pi(-1 - t/2)} + (t \leftrightarrow u). \end{aligned} \tag{5.21}$$

This condition is equivalent to

$$\pi(-1 - t/2) + \pi(-1 - u/2) = 2\mathbf{Z}\pi, \tag{5.22}$$

$$\text{or} \quad \pi(-1 - t/2) - \pi(-1 - u/2) = (2\mathbf{Z} - 1)\pi. \tag{5.23}$$

If n is even, the first equation is satisfied for any angles. Then the amplitude is trivially zero. In the following discussion, we assume that n is odd. The second equation reduces to

$$\cos\theta\cos\theta' + \sin\theta\sin\theta'\cos\varphi' = \frac{2\mathbf{Z} - 1}{n + 4}. \tag{5.24}$$

Fixing $\theta = 0$ makes clear a comparison of this result to the double-slit experiment in Sec. 5.1. In the present case the zeros of the amplitude are at

$$\cos\theta' = \frac{2k + n}{n + 4}, \tag{5.25}$$

for an integer $k \in \mathbf{Z}$. Rewriting this as

$$\cos\theta' \simeq \frac{k'}{n + 4} = \frac{k'}{2p^2}, \tag{5.26}$$

where k' is an odd integer, $k' \in 2\mathbf{Z} - 1$, we find that the location of the zeros is exactly the same as that of the double-slit experiment, (5.2), with the replacement

$$p^2 = \frac{l}{\lambda_{\rm ds}}. \tag{5.27}$$

Here p is the magnitude of the tachyon momentum in the Veneziano amplitude, while l ($\lambda_{\rm ds}$) is the slit-separation (wave length) in the double-slit experiment.

We have found here that the zeros of the Veneziano amplitude coincide completely with the double-slit experiment. In the next subsection, we look at the Veneziano amplitude in more detail and will find that indeed the imaging of the fundamental string results in a double-slit in the $n \to \infty$ limit.

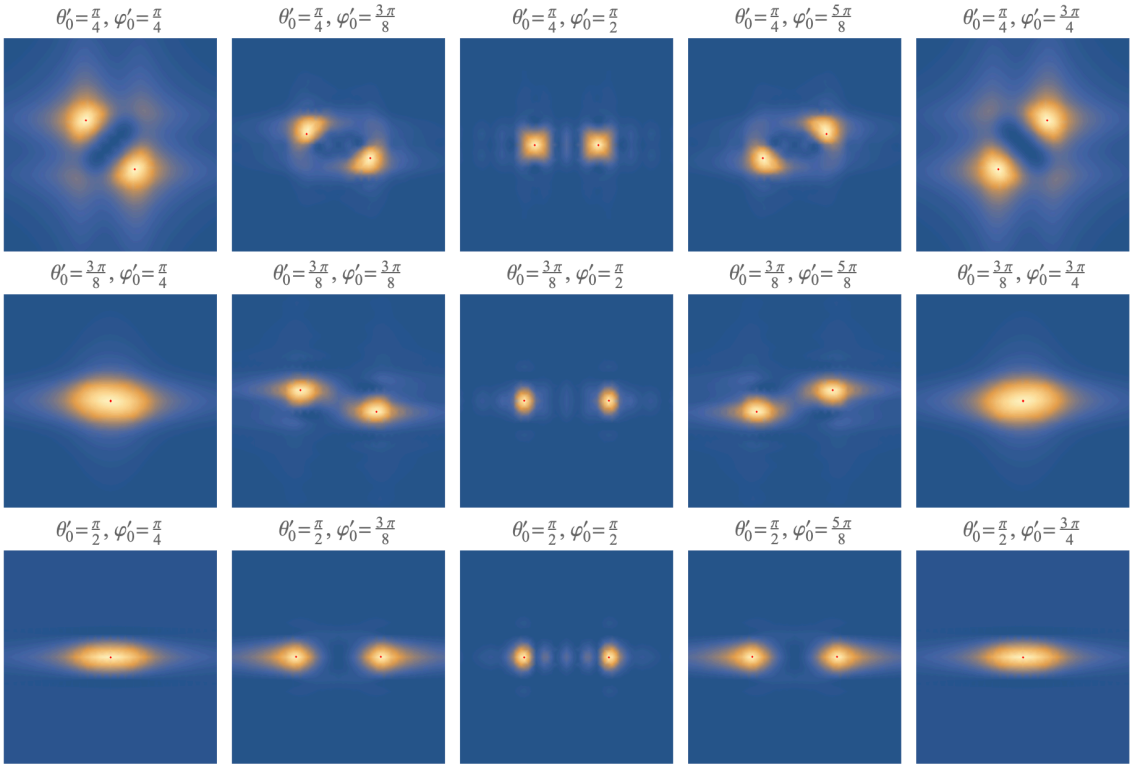

Figure 17: Images of a fundamental string, extracted and reconstructed from the s-channel pole of the Veneziano amplitude. The incoming angle is chosen as $\theta = \pi/2$. Various figures are for different choices of the viewer's location (lens location) specified by (θ'_0, φ'_0). Brightness of these density plots is normalized in each plot. The red points in the images are the brightest points.

5.2.2 Imaging of a fundamental string

Here first we present images of a string by straightforward numerical evaluations, and after that, we analyze the images analytically in a certain limit to extract the structure.

The imaging formula described in Sec. 5.1 is

$$I(X,Y) = \frac{1}{(2d)^2 \sin\theta'_0} \int_{\theta'_0-d}^{\theta'_0+d} d\theta' \int_{\varphi'_0-d/\sin\theta'_0}^{\varphi'_0+d/\sin\theta'_0} d\varphi' e^{ip((\theta'-\theta'_0)X+(\varphi'-\varphi'_0)Y)} \tilde{\mathcal{A}}_s^{\rm Ven}(\theta',\varphi'). \tag{5.28}$$

Here d is the size of the lens whose center is put at $(\theta', \varphi') = (\theta'_0, \varphi'_0)$. The lens is applied to the wave signal $\tilde{\mathcal{A}}_s^{\rm Ven}(\theta', \varphi')$ which reached the asymptotic infinity with the angle (θ', φ') in the 2-dimensional spherical coordinate. The frequency of the wave, appearing in the formula (5.4), is now given by the tachyon momentum p. The wave amplitude is taken as the residue of the s-channel pole at $s = 2n$, of the Veneziano amplitude (5.16).

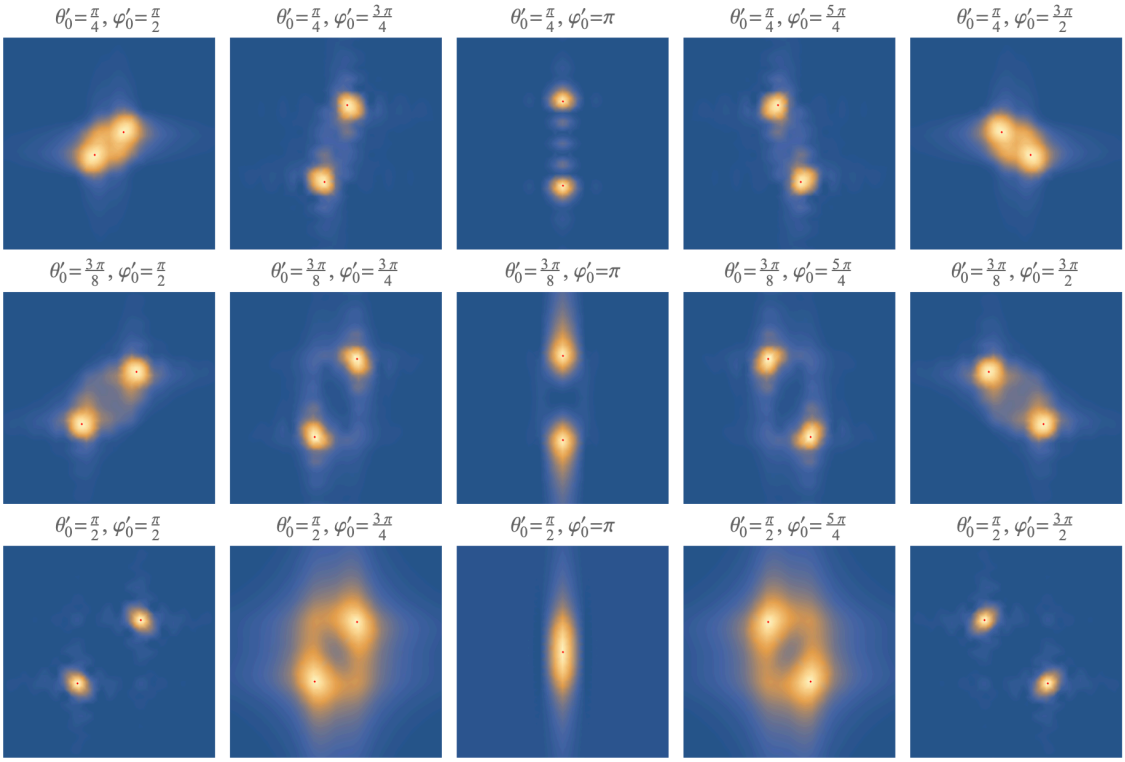

Figure 18: Images of a fundamental string, with $\theta = \pi/4$.

A straightforward numerical evaluation of the imaging (5.28) produces the images shown in Fig. 17 and Fig. 18. Since the tachyon scattering is in the center-of-mass frame, we can fix θ without losing generality. Fig. 17 and Fig. 18 are for $\theta = \pi/2$ and $\theta = \pi/4$, respectively, with $n = 11$. We find that in fact the images of the fundamental string are those of the double slits.

Analytic estimation of the image, which is useful to study the structure of the images, is possible. Let us investigate in particular the separation between the two slits. For simplicity let us take $\theta = 0$ to eliminate the φ'-dependence of the amplitude (5.16). We find

$$\tilde{\mathcal{A}}_s^{\text{Ven}} = \frac{1}{(n+1)!}\left[\frac{\Gamma\left(\frac{n}{2}+1-\frac{n+4}{2}\cos\theta'\right)}{\Gamma\left(-\frac{n}{2}-\frac{n+4}{2}\cos\theta'\right)} + \frac{\Gamma\left(\frac{n}{2}+1+\frac{n+4}{2}\cos\theta'\right)}{\Gamma\left(-\frac{n}{2}+\frac{n+4}{2}\cos\theta'\right)}\right]. \tag{5.29}$$

To perform an analytic evaluation of the imaging formula for this amplitude, we need to find a simplified expression of the amplitude. A simplification occurs when we take a large n. Indeed, in the large n limit the zeros are very close to each other, thus a small lenz is sufficient for the imaging. This means that we need only a local expression of (5.29) around a certain value of θ'.

Below, we obtain a simplified local expression of the amplitude around a zero specified by

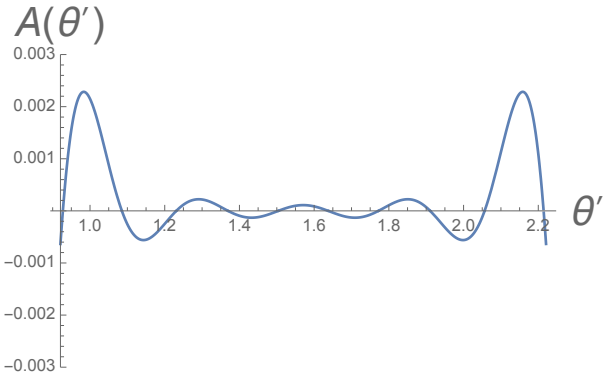

Figure 19: A plot of the amplitude (5.29) for $n = 11$, magnified around $\theta' = \pi/2$.

the integer k given in (5.24). We present two expressions; one is for the region around the zero with $k = -(n+1)/2$, which means the expression for $\theta' \sim 0$ in the large n limit, and the other is for a generic value of k.

First, notice that the amplitude (5.29) can be locally approximated by

$$\tilde{\mathcal{A}}_s^{\rm Ven} \sim f(\theta') \cos(c\theta'), \tag{5.30}$$

where c is a constant dependent on the choice of k of the central zero, and $f(\theta')$ is some smooth positive function giving the magnitude of the oscillation. This is obvious if we look at the plot of the amplitude (5.29) given in Fig. 19. The amplitude has zeros at (5.24) and does not diverge, so it can be approximated by the form (5.30) with a very simple function $f(\theta')$.

The derivation of the explicit form of $f(\theta')$ and the constant c is simple. The latter can be fixed by the distribution of the location of the zeros given in (5.24), and the magnitude function $f(\theta')$ can be fixed by evaluating the slope of the amplitude at those zeros. A straightforward calculation shows

$$\tilde{\mathcal{A}}_s^{\rm Ven}(\theta') \sim \pm \left[\frac{2}{\pi\, {}_nC_{\frac{n}{2}}} \right] \cos\left(\frac{n\pi}{2} \left(\theta' - \frac{\pi}{2} \right) \right) \qquad (\theta' \sim \theta'_0 = \pi/2) \tag{5.31}$$

This expression tells us that the magnitude function $f(\theta')$ is constant around $\theta' = \pi/2$. And for a generic k (which means $\theta' \sim \theta'_0$ for generic θ'_0), we find

$$\tilde{\mathcal{A}}_s^{\rm Ven}(\theta') \sim \pm \left[\frac{2}{n\pi\, {}_nC_{\frac{n}{2}(1-\cos\theta'_0)}} \left(\frac{1-\cos\theta'_0}{1+\cos\theta'_0} \right)^{(n\sin\theta'_0/2)(\theta'-\theta'_0)} \right] \cos\left(\frac{n\pi \sin\theta'_0}{2} (\theta' - \theta'_0) \right). \tag{5.32}$$

We can see that the magnitude function $f(\theta')$ is an exponentially growing function. As a consistency check, if one puts $\theta'_0 = \pi/2$ in this expression (5.32), it reduces to (5.31)[26].

[26]Note that the difference factor $1/n$ is irrelevant as it comes out by just how the combinatoric factor ${}_nC_{\frac{n}{2}(1-\cos\theta'_0)}$ is evaluated in the sub-leading order in the large n expansion. In any case, the overall constant factor is not the issue to look at the structure of the images.

Let us evaluate the imaging formula (5.28) with these large-n approximated amplitudes (5.31) and (5.32). For the case $\theta' \sim \pi/2$, the expression (5.31) is completely the same as that of the double slit (5.3), and we find

$$I_{\theta_0=\pi/2}(X,Y) \propto \sigma(Y)\left[\sigma\left(X-\pi p\right)+\sigma\left(X+\pi p\right)\right] \tag{5.33}$$

where

$$\sigma(x) \equiv \frac{\sin(pdx)}{pdx}. \tag{5.34}$$

The function σ is, as was described for the case of the double-slit experiment, is highly peaked at $x=0$ in the limit $p \to \infty$. Thus the bright spots in the image are localized at

$$(X,Y) = (\pm\pi p, 0). \tag{5.35}$$

This is in fact a double slit. In the limit $n \simeq 2p^2 \to \infty$, the image consists of just two bright point-like spots, and the coincidence with the double-slit experiment is exact.

The distance Δ between the two bright points in the image is given by

$$\Delta = \pi\sqrt{2n} \tag{5.36}$$

in the string length unit $l_s = 1/\sqrt{2}$ which we took throughout the paper. The behavior $\Delta \sim \sqrt{n}\, l_s$ is consistent with the approximate length of a fundamental string at the excitation level n, as we will discuss in Sec. 5.4.

Next, let us evaluate the images with the generic θ_0' using (5.32). The result is

$$I_{\theta_0=\theta_0'}(X,Y) \;\propto\; \sigma\left(\frac{Y}{\sin\theta_0'}\right)\left[\sigma\left(X-\frac{\Delta(\theta_0')}{2}+i\tilde{X}_0\right)+\sigma\left(X+\frac{\Delta(\theta_0')}{2}+i\tilde{X}_0\right)\right] \tag{5.37}$$

where

$$\Delta(\theta_0') \equiv \pi\sqrt{2n}\sin\theta_0', \quad \tilde{X}_0 \equiv \sqrt{\frac{n}{2}}(\sin\theta_0')\log\frac{1+\cos\theta_0'}{1-\cos\theta_0'}. \tag{5.38}$$

This means that there are two slits which are located, in the complexified coordinates,

$$(X,Y) = \left(\pm\frac{\Delta(\theta_0')}{2}+i\tilde{X}_0, 0\right). \tag{5.39}$$

The imaginary part contributes to make the peak of $\sigma(x)$ smoother, as the pole deviates from the real axis. The real part gives a physical consistency with the spatial location of the double-slit: the distance between the bright spots in the image is $\Delta(\theta_0')$. The factor $\sin\theta_0'$ in this $\Delta(\theta_0')$ is expected from the spatial consistency since the position of the viewer is shifted from the equator and thus the two slits should be seen at an angle, exactly giving the factor $\sin\theta_0'$. Thus we conclude that the images seen at angle are spatially consistent with each other, which is a nontrivial check for the image slits to be present in the real space.

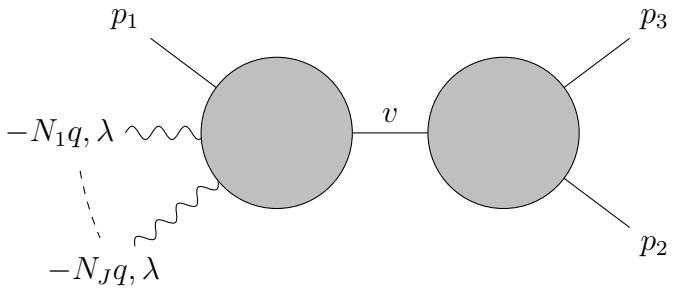

Figure 20: String amplitude of three tachyons and J photons. Picking out a pole at the internal line labeled with v leads to the amplitude of a HES decaying into two tachyons.

5.3 Images of highly excited string

In this part, we show that the slit-like behavior of a string is not limited to the Veneziano amplitude. As another clean example, we study a highly excited string (HES) decaying to two tachyons.

The amplitude formula for a HES decaying to two tachyons was computed in [43, 44]. We will briefly review their results but with slight modifications. Later, we list the location of the amplitude zeros, and point out that its amplitude zeros also match the ones of the double-slit in Sec. 5.1. Then we reconstruct images of a HES by the Fourier transformation of the amplitude. The images show multi-slits, which are understood as convolutions of double-slits.

5.3.1 Amplitude and its zeros

Following [44], we start with a string scattering amplitude for

$$\text{tachyon, } J \text{ photons} \to 2 \text{ tachyons}$$

as depicted in Fig. 20. After computing the amplitude, we pick out a pole which corresponds to an intermediate HES state. Momenta of one incoming tachyon and two outgoing tachyons are denoted by p_1, p_2 and p_3. Momenta of J photons are chosen to be proportional to a null vector, q, and are given by $-N_a q$, where N_a are integers and $a = 1, \cdots, J$. The momentum conservation law is

$$0 = (p_1 - Nq) + p_2 + p_3 \tag{5.40}$$

where

$$N = \sum_{a=1}^{J} N_a, \quad (N_a \geq 1) \tag{5.41}$$

When a pole of the intermediate state is picked out, N and J will be interpreted as the excitation level and the angular momentum of the HES, respectively. The on-shell conditions for the tachyon momenta are

$$p_1^2 = p_2^2 = p_3^2 = -(-2). \tag{5.42}$$

For simplicity, polarizations of photons are taken to be equal to each other and denoted by λ. Then, the conditions for the photon momenta and polarizations are given by

$$q^2 = 0, \quad \lambda^2 = 0, \quad q \cdot \lambda = 0. \tag{5.43}$$

For simplicity, we assume that

$$(p_2 + p_3) \cdot \lambda = 0. \tag{5.44}$$

This condition is satisfied, for example, in the center-of-mass frame. Then the amplitude is factorized as

$$\mathcal{A}^{\rm HES} = \prod_{a=1}^{J} \mathcal{A}_a, \tag{5.45}$$

$$\begin{aligned} \mathcal{A}_a = & \frac{(-p_2 \cdot \lambda) - (-p_3 \cdot \lambda)}{2} \\ & \times \left[\frac{\Gamma(-\alpha_1^{(a)} + 1)\Gamma(-\alpha_2^{(a)})}{\Gamma(-\alpha_1^{(a)} - \alpha_2^{(a)} + 1)} - \frac{\Gamma(-\alpha_2^{(a)})\Gamma(-\alpha_3^{(a)})}{\Gamma(-\alpha_2^{(a)} - \alpha_3^{(a)})} + \frac{\Gamma(-\alpha_3^{(a)})\Gamma(-\alpha_1^{(a)} + 1)}{\Gamma(-\alpha_3^{(a)} - \alpha_1^{(a)} + 1)} \right], \end{aligned} \tag{5.46}$$

where

$$\alpha_i^{(a)} = N_a p_i \cdot q. \tag{5.47}$$

Each factor of the amplitude, $\mathcal{A}_a$ has poles when $1 - \alpha_1^{(a)}$ is a negative integer. Poles at

$$\alpha_1^{(a)} \sim N_a, \tag{5.48}$$

are located at the same position in the momentum space,

$$v = -(p_1 - Nq)^2 \sim 2(N-1). \tag{5.49}$$

Picking out this pole, we have a HES at an intermediate state. By taking the residues of $\mathcal{A}_a$, we obtain the decay of the HES with the mass

$$M^2 = 2(N-1), \tag{5.50}$$

and the total angular momentum J. Using an identity $\alpha_1^{(a)}+\alpha_2^{(a)}+\alpha_3^{(a)}=0$, and the condition of the pole, $\alpha_1^{(a)}\sim N_a$, we find

$$\begin{aligned}\tilde{\mathcal{A}}_v^{\rm HES} &= \lim_{v\to 2(N-1)}\left(\prod_{a=1}^{J}\frac{\sin\pi\alpha_1^{(a)}}{\pi}\right)\mathcal{A}^{\rm HES}\\ &= \prod_{a=1}^{J}\frac{(-p_2\cdot\lambda)-(-p_3\cdot\lambda)}{2}\left[\frac{\Gamma(-\alpha_2^{(a)})}{\Gamma(N_a)\Gamma(-\alpha_2^{(a)}-N_a+1)}+(2\leftrightarrow 3)\right]\\ &= \prod_{a=1}^{J}\frac{(-p_2\cdot\lambda)-(-p_3\cdot\lambda)}{2}\left[\frac{\Gamma(-\alpha_2^{(a)})}{\Gamma(N_a)\Gamma(\alpha_3^{(a)}+1)}+(2\leftrightarrow 3)\right]\end{aligned}\tag{5.51}$$

Here, the first term is a contribution studied in [44].

In the center-of-mass frame, we take the following parametrization of the momenta,

$$-q=\frac{1}{\sqrt{2N-2}}\begin{pmatrix}1\\0\\0\\-1\end{pmatrix},\qquad \lambda=\frac{1}{\sqrt{2}}\begin{pmatrix}0\\1\\i\\0\end{pmatrix},\tag{5.52}$$

$$p_1-Nq=\begin{pmatrix}\sqrt{2N-2}\\0\\0\\0\end{pmatrix},\quad -p_2=\begin{pmatrix}\sqrt{2N-2}/2\\ \sqrt{2N+6}/2\ \sin\theta'\\0\\ \sqrt{2N+6}/2\ \cos\theta'\end{pmatrix},\quad -p_3=\begin{pmatrix}\sqrt{2N-2}/2\\ -\sqrt{2N+6}/2\ \sin\theta'\\0\\ -\sqrt{2N+6}/2\ \cos\theta'\end{pmatrix}.\tag{5.53}$$

Under this parametrization, the variables $\alpha_i^{(a)}$ are expressed as

$$\alpha_1^{(a)}=N_a,\tag{5.54}$$

$$\alpha_2^{(a)}=-\frac{N_a}{2}\left(1+\frac{\sqrt{2N+6}}{\sqrt{2N-2}}\cos\theta'\right),\tag{5.55}$$

$$\alpha_3^{(a)}=-\frac{N_a}{2}\left(1-\frac{\sqrt{2N+6}}{\sqrt{2N-2}}\cos\theta'\right).\tag{5.56}$$

Let us look for zeros of the amplitude (5.51). It is zero if and only if

$$0=(-p_2\cdot\lambda)=-(-p_3\cdot\lambda),\tag{5.57}$$

$$\text{or}\qquad 0=\Gamma(-\alpha_2^{(a)})\Gamma(\alpha_2^{(a)}+1)+(2\leftrightarrow 3)\tag{5.58}$$

for some $1\le a\le J$. Calculations similar to those in Sec. 5.2 show that the amplitude is trivially zero if some N_a is even. In the following discussion, we assume that N_a's are odd for any $1\le a\le J$. Then we find that the zeros of the amplitude are at

$$\frac{\sqrt{2N+6}}{\sqrt{2N-2}}\cos\theta'=\frac{2\mathbf{Z}-1}{N_a}.\tag{5.59}$$

In the high excitation limit $N_a \to \infty$, it is written as

$$\cos\theta' \simeq \frac{k'}{N_a}, \tag{5.60}$$

where k' is an odd integer, $k' \in 2\mathbf{Z} - 1$. We find that the location of the zeros is exactly the same as that of the double-slit experiment, (5.2), with the replacement

$$\frac{N_a}{2} = \frac{l}{\lambda_{\rm ds}}. \tag{5.61}$$

Here N_a is an excitation level of the a-th mode such that $N = \sum_a N_a$, while l ($\lambda_{\rm ds}$) is the slit separation (wave length) in the double-slit experiment.

5.3.2 Imaging of a highly excited string

Here first we present images of a HES by straightforward numerical evaluations, and then understand the images analytically in a certain limit.

Since the amplitude depends only on the outgoing angle θ', we restrict ourselves to imaging in this single direction. We use the following imaging formula

$$I(X) = \frac{1}{(2d)^2 \sin\theta'_0} \int_{\theta'_0-d}^{\theta'_0+d} d\theta' e^{ip(\theta'-\theta'_0)X} \tilde{\mathcal{A}}_v^{\rm HES}(\theta'). \tag{5.62}$$

Here p is now the magnitude of the outgoing tachyon momentum $p = \sqrt{2N+6}/2$. A straightforward numerical evaluation of the imaging formula (5.62) produces the images shown in Fig. 21. Both of the images are for $\theta'_0 = \pi/2$, but with different numbers of excitations of $N = \sum_{a=1}^{J} N_a$. We find that the images of a HES are those of multi-slits.

Such multi-slit structures can simply be understood by using the results in the Veneziano amplitude. When $N_a \gg 1$, the amplitude (5.51) reduces to a simple form

$$\tilde{A}_v^{\rm HES} \simeq \prod_{a=1}^{J} \sin\theta' \left[\frac{\Gamma\left(+\frac{N_a}{2}(1+\cos\theta')\right)}{\Gamma\left(-\frac{N_a}{2}(1-\cos\theta')\right)} + \frac{\Gamma\left(+\frac{N_a}{2}(1-\cos\theta')\right)}{\Gamma\left(-\frac{N_a}{2}(1+\cos\theta')\right)} \right] \tag{5.63}$$

up to a constant. Remark that each factor inside $\prod_{a=1}^{J}$ coincides with the Veneziano amplitude at $\theta = 0$ (5.29) with the replacement $n \to N_a$,

$$\tilde{\mathcal{A}}_v^{\rm HES} \simeq (\sin\theta')^J \prod_{a=1}^{J} \tilde{\mathcal{A}}_s^{\rm Ven}\Big|_{n\to N_a}. \tag{5.64}$$

Thus the reconstructed image of a HES, the Fourier transformation of $\tilde{\mathcal{A}}_v^{\rm HES}$, is the convolution of the images of the Veneziano amplitudes with $n \to N_a$ as,

$$I^{\rm HES} \simeq (\sin\theta')^J * I^{\rm Ven}\big|_{n\to N_1} * \cdots * I^{\rm Ven}\big|_{n\to N_J}. \tag{5.65}$$

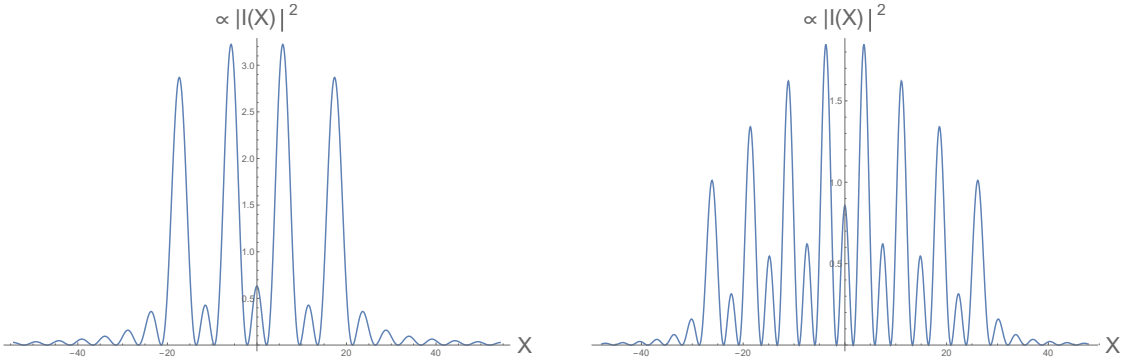

Figure 21: Images of a highly excited string, extracted and reconstructed from a HES intermediate state pole of the tachyon-photon amplitude. The size of the imaging lens is chosen as $d = 0.11$. The left panel, for a division $N = N_1 + N_2 = 19 + 39$, shows a 4-slit, while the right panel, for $N = N_1 + N_2 + N_3 = 19 + 39 + 79$, shows an 8-slit.

Recall that the image of the Veneziano amplitude $I^{\rm Ven}$ is a double-slit with a slit separation $l/\lambda_{\rm ds} \simeq n/2$. With replacements $n \to N_a, \lambda_{\rm ds} \to 1/\sqrt{N}$, the image of a HES is the convolution of double-slits with separations $\Delta_a \sim N_a/\sqrt{N}$. Then we can conclude that the image of a HES is a 2^J-slit. Indeed it can be easily demonstrated that the convolution of double-slits with different slit separations is a multi-slit. Let

$$I_a(X) = \delta\left(X - \frac{\Delta_a}{2}\right) + \delta\left(X + \frac{\Delta_a}{2}\right) \tag{5.66}$$

be an ideal image of a double-slit with the slit separation Δ_a. Then its convolution

$$\begin{aligned} I_a * I_b(X) &= \int_{-\infty}^{\infty} {\rm d}X' \; I_a(X') I_b(X - X') \\ &= \sum_{s_1, s_2 = \pm 1} \delta\left(X + s_1 \frac{\Delta_a}{2} + s_2 \frac{\Delta_b}{2}\right) \end{aligned} \tag{5.67}$$

is a 2^2-slit. Performing similar operations recursively, we can show that J-times convolution of the double-slit with different slit-separations is a 2^J-slit as[27]

$$I_1 * \cdots * I_J(X) = \sum_{s_a = \pm 1} \delta\left(X + s_1 \Delta_1 \cdots + s_J \Delta_J\right). \tag{5.68}$$

We conclude that the image of the highly excited string reconstructed from its decay amplitude is a multi-slit.

[27]Particularly when $\Delta_a/\Delta_1 \simeq 2^a$, the slits are equally separated.

5.4 Interpretation

In this part, we present several observations from the results obtained above, and provide their possible interpretations.

Firstly, we point out that the slit-like appearance of scattering amplitude images is an inherent feature of strings. Recall, for example, the Veneziano amplitude. At the zeros of the amplitude (5.24), each term of (5.16) becomes zero simultaneously. There is no non-trivial cancellation between the two terms. In other words, the zeros of the amplitude originate in the gamma functions in the denominator. These gamma functions are also the source of poles which correspond to intermediate excited string states. Thus the existence of a series of zeros (5.24) reflects the existence of a series of intermediate states in string theory. Remember that, contrary to string theory, perturbative quantum field theories have only a few intermediate states, and scatterings occur at a point.

Secondly, it is remarkable that the order of slit separtions agrees with that of the total string length. Recall that the slit separations in the Veneziano amplitude and in the HES scattering amplitude (with $J = 1$) are

$$\Delta^{\rm Ven} \sim \sqrt{n}\, l_s, \quad \Delta^{\rm HES} \sim \sqrt{N}\, l_s, \tag{5.69}$$

respectively. Here n is roughly the square of the invariant mass, and N is roughly the square of the mass of a HES. On the other hand, the total length of a string with a mass M is roughly estimated as

$$l_{\rm total} \sim \frac{1}{\alpha'} M \sim \sqrt{N}\, l_s \tag{5.70}$$

since a string has a constant tension α'. Thus, the slit separation and string length coincide with each other, meaning that the string may extend between the slits.

Thirdly, we stress that slits can only show up on a straight line both in the Veneziano amplitude and the HES amplitude. Technically, this is because the θ' dependence of their amplitude zeros is only in the form of $\pm\cos\theta'$. In fact, other types of θ' dependence with non-trivial phases $\cos(\theta' - \vartheta')$ are required for the slit to show up away from the straight line. This can be easily demonstrated as follows. Suppose that we have three slits S_1, S_2, S_3 which are not on a straight line as in Fig. 22. If the location of S_3 is $(z, x) = (0, -l'/2)$, the optical path lengthes are

$$\overline{\rm S_1P} - \overline{\rm OP} = -\frac{l}{2}\cos\theta', \tag{5.71}$$

$$\overline{\rm S_2P} - \overline{\rm OP} = +\frac{l}{2}\cos\theta', \tag{5.72}$$

$$\overline{\rm S_3P} - \overline{\rm OP} = +\frac{l'}{2}\cos(\theta' - \pi/2). \tag{5.73}$$

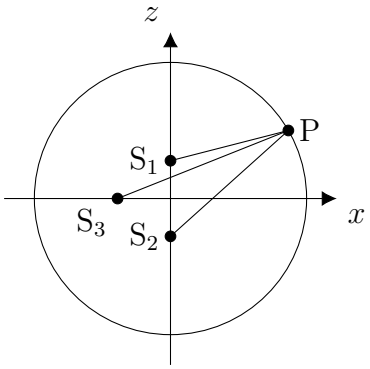

Figure 22: Three slits are put at S_1, S_2, S_3, and scattered wave is observed at the point P.

Thus the location of the amplitude zeros depends not only on $\pm\cos\theta'$ but also on the phase-shifted $+\cos(\theta'-\pi/2)$.

From these observations, we can provide an interpretation that the location of slits are the end points of a string. Firstly, we should remark that the order of the slit separation is not the random walk size $l \sim M^{1/2} \sim N^{1/4}$, but rather it is the total length of the string $L \sim M \sim N^{1/2}$. It motivates us to assume that the string behaves like a simple harmonic oscillator in the scattering processes.

Then there remain two possibilities: the locations of slits indicate (i) the nodes, or (ii) the end points, of the vibrating string. The first possibility is excluded since the HES amplitude with $J = 1, N \gg 1$ behaves like a double-slit as discussed in Sec. 5.3. If the nodes of the vibrating string are the origin of the slit image, the HES image with $J = 1, N \gg 1$ would have been a multi-slit, rather than the double-slit. Since this is not the case, thus we are left with the possibility (ii): slits are end points of the string.

Such an interpretation is also supported by the following scenarios. Suppose there is a classical vibrating string with markers attached to its end points, as an analogy of the world sheet with open string vertex operators inserted at its boundary. The long time average of the probability that the markers are found at a point X is roughly evaluated by

$$\int_0^T \frac{\mathrm{d}t}{T}\,\delta(X - X_0\sin\omega t) \sim \frac{1}{\sqrt{X_0^2 - X^2}}. \tag{5.74}$$

Then it becomes maximum at the point where the string is fully extended to its maximum size. This is consistent with our results where slits appeared with the slit separations of the order of the total string length.

Another scenario is about the origin of interference patterns. Suppose that incoming two strings are shot along the z-direction and scattered at the origin. Our results have shown that if this scattering is observed from the x-direction, the image is the double-slit lined up along

the z-direction. It would be natural to imagine that a string formed at the origin vibrates along the z-direction, and is torn apart when the string reaches its maximum length. Each of two pieces of the broken string can be scattered in any directions, though one must go in the opposite direction to the other. The observer in the x-direction can detect the scattered string with a definite probability. At the observation, the observer has two possibilities: the left one of the two pieces of the broken string reaches the observer while the right one goes in the opposite direction, or visa versa. The superposition of these two possibilities would be the source of the interference patterns which appear in the string scattering amplitudes.

These scenarios encourage us to state that the slits are the end points of a fundamental string.

5.5 Possible cases when chaos shows up

The slit-like structure of highly excited strings is a negative result for looking for chaos. Based on the interpretations explained previously, the bright spots in string images are understood as the place from which small pieces of a string come to an observer. Thus string scatterings we have studied are analogous to classical scatterings on multi-disks but all of whose disks are aligned along the same straight line. As we have reviewed, such scattering systems do not show chaos, nor string scatterings.

Nevertheless, it is too early to admit that string scattering has no chaos. In classical scatterings, chaos shows up when disks are placed away from the straight line. It makes particles collide with disks many times within a scattering region. Some setups of string scatterings can mimic such complicated collisions of particles. For example, we can consider a closed string. Since a closed string has a circle shape, its images may have bright spots on a circle, not on a straight line. Such a non-trivial geometrical structure could be the source of chaos. We may also have to consider 2-to-3 or 3-to-3 amplitudes as classical scatterings need no less than three disks for chaos to show up.

6 Conclusion and discussions

Summary of results

In this Ph.D. thesis, we have looked for chaos in string scatterings. We have studied open bosonic string amplitudes at tree-level. Our results showed that there is no fractal structure in the scattering data, nor non-trivial geometrical structure in the scattering regions. We have concluded that there is no sign of chaos in highly excited strings within our strategy to extract chaos and the HES states we have constructed.

In section Sec. 2, we reviewed black hole chaos. The essence of black hole chaos is the redshift near the event horizon. Also, recent studies on fast scrambling and chaos bounds imply that black holes are the most chaotic system in the universe.[28] These features distinguish black hole chaos from the chaos in ordinary many body systems. The correspondence principle between black hole states and string states has motivated us to look for the source of black hole chaos in highly excited strings.

In section Sec. 3, we reviewed transient chaos. Transient chaos is characterized by three properties: unexpectability, aperiodicity, and fractality. These are generated by three key mechanisms: stretching, folding, and escape. These mechanisms amplify a small deviation of the initial conditions iteratively for a finite time, causing irregular behaviors of a system. Transient chaos can be detected by a fractal structure in scattering data, and non-trivial geometrical structure in a scattering region.

In section Sec. 4, we have studied scattering amplitudes of a highly excited string and looked for a fractal structure in the scattering data. We considered open bosonic string amplitudes at tree-level as the first step. The states of a highly excited string were constructed by mimicking the DDF formalism. Since scattering amplitudes take non-zero values at almost all angles, we picked out the largest poles to construct scattering data $\theta'(\theta)$. Our results showed that there is no fractal structure in the scattering data.

In section Sec. 5, we have looked for a non-trivial geometrical structure in string scattering regions. We performed the Fourier transformation of string scattering amplitudes to take pictures of string scattering regions. Our results showed that the string scattering regions look like double-slits. Their geometrical structure was too simple to produce chaos.

Future works

Although the results were negative at this state, we have not yet excluded all possibilities. We need to continue our research to look for chaos in other setups.

[28] As explained in the introduction, more precise definitions for scrambling and quantum chaos should be developed.

At the end of Sec. 4 and Sec. 5, we have discussed that chaos possibly shows up when higher loop corrections are included, or when we consider a closed string, 5-point or 6-point scattering amplitudes. Also, we may need to consider more general states of a highly excited string. The photons we have shot into tachyons to construct HES states have shared the same polarization, and they could be generalized. These are left for future works.

It will be a better idea to look for a fractal structure in plots of delay-time with respect to an incoming angle. As explained in the review part Sec. 3, sometimes a fractal structure is cleaner to see in delay-time $T(\theta)$ than in the scattering data $\theta'(\theta)$ we have used. Also, we may need to modify our strategy to extract chaos. Since our definition of the scattering data extracts just an aspect of the quantum amplitudes (although we believe that it is a natural definition), there could be a more sophisticated definition of the scattering data which may manifest possible transient chaos. For example, we have ignored the impact parameter b in our definition because usually the quantum scatterings are defined by plane waves. However, if one considers wave packets rather than the plane waves, the amplitudes would contain more information about the locality of the HES structure.

We may develop more powerful tools to study string amplitudes. One hint lines in the works of [64–67]. The authors analyzed the high energy behavior of string amplitudes by finding saddles of the world-sheet integral. Since their main interest was $s \to \infty$ dependency, they focused on a single saddle contribution, ignoring angular dependency. We may improve their computations by, say, including contributions from other non-trivial saddles. The idea could be tested by the hyperasymptotics [68, 69] in the the Airy [70] function, the Gamma function [71], and the Beta function.

It will also be interesting to analyze the geometrical structure of strings more precisely. Its hint is in the spacetime uncertainty principle [72–74]. Yoneya looked for a string counterpart of the uncertainty principle in quantum mechanics. He arrived at spacetime uncertainty $\Delta X \Delta T \gtrsim 1$, and tried to reformulate string theory so that its geometrical structure becomes clearer [75]. The idea may be developed to study the geometrical structure of a string scattering region.

These problems are left for future works. By solving these, we will be able to approach microscopic irregular dynamics in black holes which explains their thermal properties.

Chaos in the future

While we have looked for chaos in this thesis, I hope that the word chaos is replaced with a more precise word in the future. Chaos is essentially the negation of solvability. It means that we have little knowledge about irregular dynamics, nor precise words to classify a variety of chaotic systems.

Our mission is to pin down the essential dynamics in highly excited strings which describes the thermal nature of black holes from microscopic viewpoints. The problem would be quite hard since the problem of thermalization is already challenging and very exciting without gravity.

We may need to liberate ourselves from the idea of an independent entity, or free quanta separated from a background. Modern physics assumes the existence of a free particle and additionally introduces interactions. Although we have eaten a lot of fruits from such a formulation, typical systems in the universe are not so simple. Around the transition between a highly excited string and a black hole, counting the number of strings makes no sense since there are irregular connection/re-connection processes within an interaction region.

I believe that the formulation of modern physics is quite inefficient in describing highly excited strings. Then what should we do to describe them? I have no idea at all now, however, I believe that chaos might give us some hints.[29] We should know more about chaos to pin down the essential mechanism, and to classify a variety of irregular systems. Then we may find a new concept to describe highly excited strings nonperturbatively.

[29] I also believe that resurgence might tell us a way to liberate ourselves from perturbation.

Acknowledgment

This Ph.D. thesis is based on my works [76, 77] which were partly done in collaboration with K. Hashimoto and Y. Matsuo. Although I could not include all subjects of other papers, I shall be grateful to collaborators M. Honda, T. Fujimori, S. Kamata, T. Misumi, N. Sakai on my research on resurgence. I would like to thank T. Onogi and H. Fukaya, who gave me an opportunity to start a new project on anomaly. I learned a lot through discussions and writing papers.

I am really indebted to the hospitality of my supervisor K. Hashimoto, and all members of my laboratory at Kyoto University. I would like to thank H. Hata, H. Kawai, S. Sugimoto, M. Fukuma, K. Tsumura, K. Yoshioka, K. Yoshida, K. Sugiyama, T. Ishii, Y. Matsuo, Y. Namekawa, H. Kyono, J. Sakamoto, K. Sakai, J. Yamamoto, Y. Hamada, N. Matsumoto, T. Ohata, S. Okumura, Y. Abe, J. Haruna, O. Fukushima, S. Kushiro, D. Takeda, R. Watanabe, T. Ito, K. Kyo, K. Sugiura, J. Yoshinaka, T. Ishii, T. Shigemura, and T. Tsukamoto.

It was an honor to have discussed spacetime uncertainty with T. Yoneya. His words "we are just going up a spiral staircase" encouraged me to continue my research on quantum gravity. Although I could not meet T. Maskawa face-to-face before he passed away, I would like to keep his words "Shutei-Ganko" in mind; his unique use of words, meaning that "have a high perspective to see far into the future, but do make a steady progress."

I enjoyed discussions on resurgence with J. Haruna, K. Murakami, Y. Hayashi, climbing mountains with H. Kanno, H. Omiya, K. Shiozaki, Y. Tanizaki, baseball with M. Amo, D. Takeda, Y. Taki, K. Kyo, J. Yoshinaka, and playing Nintendo Smash Bros. oji-san-battle with J. Haruna, K. Murakami, H. Omiya, R. Toshio, Y. Manita, T. Takahashi.

I thank singer-songwriter L. Ieiri. Her passionate music always strengthened my mind. I would like to cherish my memories with M. Genshin and Y. Kondo, my best friends at Kariya high school. I learned the joy of discussing problems in front of a blackboard, which made me decide to become a physicist. R. Usami and M. Hearn reminded me of my passion for string theory. I thank game creator ZUN, doujin writer Sohika, and doujin illustrator Minus.

Last but not least, I would like to thank my parents Takashi, Michiko, and my brother Tsuyoshi. They gave me opportunities to have an interest in science and supported me in studying a lot of things freely.

The works of T.Y. is in part supported by Sasakawa Scientific Research Grant from The Japan Science Society ID:2021-2026, JST SPRING Grant Number JPMJSP2110, and JSPS KAKENHI Grant No. JP22J15276.

A Explicit formulas of HES-tachyon to HES-tachyon amplitude

We start with a general formula for the bosonic open string tree-level amplitude, and pick out poles corresponding to HES states as was done in [44]. We use the same strategy to compute the four-point amplitude of the scattering of the HES-tachyon to HES-tachyon, to obtain the scattering data $\theta'(\theta)$.

A.1 Channels

The general formula for the tree-level amplitude involving any number of tachyons and photons is given by

$$\mathcal{A} = \frac{1}{\text{vol.}} \int \mathrm{d}w_i \, \mathrm{d}z_a \prod_{i<j} |w_{ij}|^{p_i \cdot p_j} \prod_{a<b} |z_{ab}|^{p_a \cdot p_b} \prod_{i,a} |w_i - z_a|^{p_i \cdot p_a} \times \exp\left[\sum_{a \neq b} \frac{\lambda_a \cdot \lambda_b}{2 z_{ab}^2} - \sum_{i,a} \frac{p_i \cdot \lambda_a}{w_i - z_a} \right] \Bigg|_{\mathcal{O}(\lambda_a)} , \tag{A.1}$$

where $w_{ij} = w_i - w_j$, $z_{ab} = z_a - z_b$. Here the indices i run over the tachyons, and the indices a run over the photons. The photon polarizations are denoted by λ_a.

We focus on the case $q \propto q'$ but applied to general integer J.[30] Using the assumption $q \propto q'$, the amplitude reduces to

$$\begin{aligned} \mathcal{A} = \frac{1}{\text{vol.}} \int_{-\infty}^{\infty} \prod_{i=1,2,2',1'} \mathrm{d}w_i \prod_{i<j} |w_{ij}|^{p_i \cdot p_j} \\ \times \int_{-\infty}^{\infty} \prod_{a=1}^{J} \mathrm{d}z_a \prod_{a,i} |z_a - w_i|^{-\alpha_i} \sum_i \frac{-p_i \cdot \lambda}{w_i - z_a} \\ \times \int_{-\infty}^{\infty} \prod_{b=1}^{J} \mathrm{d}z'_b \prod_{b,j} |z'_b - w_j|^{-\beta_j} \sum_j \frac{-p_j \cdot \lambda'}{w_j - z'_b} \end{aligned} \tag{A.2}$$

where we defined

$$\alpha_i = -(-N_a q) \cdot p_i, \quad \beta_j = -(-N'_b q') \cdot p_j. \tag{A.3}$$

The integral over w_i can be divided into six parts as in the case of the Veneziano amplitude,

$$\mathcal{A} = (\mathcal{A}_{st} + \mathcal{A}_{tu} + \mathcal{A}_{us}) + (\mathcal{A}_{ts} + \mathcal{A}_{ut} + \mathcal{A}_{su}) , \tag{A.4}$$

[30] See also [54] for a recent study on computation of the amplitudes.

where

$$\begin{aligned}
\mathcal{A}_{st} &= \mathcal{A}|_{w_1'=-\infty,w_2=0,w_1=w,w_2'=1} \\
&= \int_0^1 \mathrm{d}w\ w^{p_1\cdot p_2}(1-w)^{p_1\cdot p_2'} \prod_{a=1}^{J} Z_a^{212'}(\alpha,p,\lambda;w) \prod_{b=1}^{J} Z_b^{212'}(\beta,p,\lambda';w) \qquad \text{(A.5)} \\
\mathcal{A}_{tu} &= \mathcal{A}|_{w_2=-\infty,w_2'=0,w_1=w,w_1'=1} = \mathcal{A}_{st}|_{2\to 2',2'\to 1'}\,, \qquad \text{(A.6)} \\
\mathcal{A}_{us} &= \mathcal{A}|_{w_2'=-\infty,w_1'=0,w_1=w,w_2=1} = \mathcal{A}_{st}|_{2\to 1',2'\to 2}\,, \qquad \text{(A.7)} \\
\mathcal{A}_{ts} &= \mathcal{A}_{st}|_{2\leftrightarrow 2'}\,, \qquad \text{(A.8)} \\
\mathcal{A}_{ut} &= \mathcal{A}_{tu}|_{2'\leftrightarrow 1'}\,, \qquad \text{(A.9)} \\
\mathcal{A}_{su} &= \mathcal{A}_{us}|_{1'\leftrightarrow 2}\,. \qquad \text{(A.10)}
\end{aligned}$$

Here we have defined the photon integral

$$Z_a^{ijk}(\alpha,p,\lambda;w) = \int_{-\infty}^{\infty} \mathrm{d}z_a\ |z_a|^{-\alpha_i}|z_a-w|^{-\alpha_j}|z_a-1|^{-\alpha_k}\left(\frac{-p_i\cdot\lambda}{-z_a}+\frac{-p_j\cdot\lambda}{w-z_a}+\frac{-p_k\cdot\lambda}{1-z_a}\right) \qquad \text{(A.11)}$$

A.2 Photon integral

To proceed, we define following integrals and evaluate them.

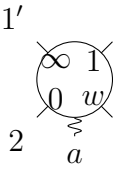

$$\begin{aligned}
&= \int_0^w \mathrm{d}z_a\ |z_a|^{-\alpha_2}|z_a-w|^{-\alpha_1}|z_a-1|^{-\alpha_2'} \\
&= \int_0^1 \mathrm{d}x\ w^{1-\alpha_2-\alpha_1}\frac{x^{-\alpha_2}(1-x)^{-\alpha_1}}{(1-wx)^{\alpha_2'}} \quad (z=wx) \\
&= w^{1-\alpha_2-\alpha_1}\Gamma(-\alpha_2+1)\Gamma(-\alpha_1+1)\,\mathbf{F}\left(\begin{matrix}\alpha_2', & -\alpha_2+1\\ -\alpha_2-\alpha_1+2\end{matrix};w\right), \qquad \text{(A.12)}
\end{aligned}$$

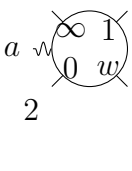

$$\begin{aligned}
&= \int_{-\infty}^0 \mathrm{d}z_a\ |z_a|^{-\alpha_2}|z_a-w|^{-\alpha_1}|z_a-1|^{-\alpha_2'} \\
&= \int_0^1 \mathrm{d}x\ \frac{x^{-2+\alpha_2+\alpha_1+\alpha_2'}(1-x)^{-\alpha_2}}{(1-(1-w)x)^{\alpha_1}} \quad (1-z=1/x) \\
&= \Gamma(\alpha_2+\alpha_1+\alpha_2'-1)\Gamma(-\alpha_2+1)\,\mathbf{F}\left(\begin{matrix}\alpha_1, & \alpha_2+\alpha_1+\alpha_2'-1\\ & \alpha_1+\alpha_2'\end{matrix};1-w\right), \qquad \text{(A.13)}
\end{aligned}$$

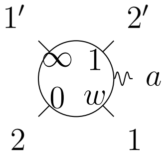

$$
\begin{aligned}
&= \int_w^1 \mathrm{d}z_a\ |z_a|^{-\alpha_2}|z_a-w|^{-\alpha_1}|z_a-1|^{-\alpha_2'} \\
&= \int_0^1 \mathrm{d}x\ (1-w)^{1-\alpha_2'-\alpha_1}\frac{x^{-\alpha_2'}(1-x)^{-\alpha_1}}{(1-(1-w)x)^{\alpha_2}} \quad (z=(1-w)(1-x)+w) \\
&= (1-w)^{1-\alpha_2'-\alpha_1}\Gamma(-\alpha_2'+1)\Gamma(-\alpha_1+1)\,\mathbf{F}\left(\begin{matrix}\alpha_2, & -\alpha_2'+1 \\ & -\alpha_2'-\alpha_1+2\end{matrix};1-w\right)
\end{aligned}
$$

$=$ 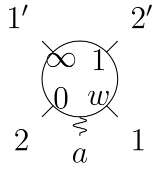

$$
\Bigg|_{2\leftrightarrow 2',\ w\leftrightarrow 1-w}\ , \qquad \text{(A.14)}
$$

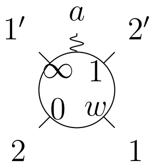

$$
\begin{aligned}
&= \int_1^\infty \mathrm{d}z_a\ |z_a|^{-\alpha_2}|z_a-w|^{-\alpha_1}|z_a-1|^{-\alpha_2'} \\
&= \int_0^1 \mathrm{d}x\ \frac{x^{-2+\alpha_2'+\alpha_1+\alpha_2}(1-x)^{-\alpha_2'}}{(1-wx)^{-\alpha_1}} \quad (z=1/x) \\
&= \Gamma(\alpha_2'+\alpha_1+\alpha_2-1)\Gamma(-\alpha_2'+1)\,\mathbf{F}\left(\begin{matrix}\alpha_1, & \alpha_2'+\alpha_1+\alpha_2-1 \\ & \alpha_1+\alpha_2\end{matrix};w\right)
\end{aligned}
$$

$=$ 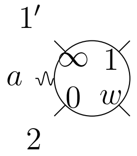

$$
\Bigg|_{2\leftrightarrow 2',\ w\leftrightarrow 1-w}\ . \qquad \text{(A.15)}
$$

Then the photon integrals are evaluated as follows.

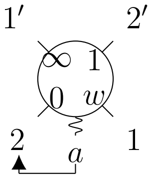

$$
= \int_0^w \mathrm{d}z_a\ |z_a|^{-\alpha_2}|z_a-w|^{-\alpha_1}|z_a-1|^{-\alpha_2'}\ \frac{-p_2\cdot\lambda}{-z_a}
$$

$= -(-p_2\cdot\lambda)$ 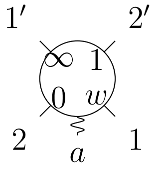

$$
\Bigg|_{\alpha_2\to\alpha_2+1}\ , \qquad \text{(A.16)}
$$

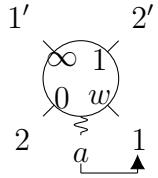

$$= \int_0^w \mathrm{d}z_a \ |z_a|^{-\alpha_2}|z_a - w|^{-\alpha_1}|z_a - 1|^{-\alpha_2'} \ \frac{-p_1 \cdot \lambda}{w - z_a}$$

$$= +(-p_1 \cdot \lambda)$$

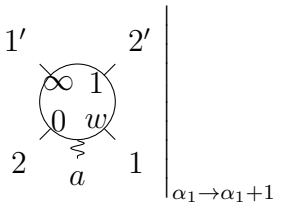

, (A.17)

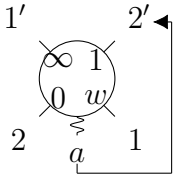

$$= \int_0^w \mathrm{d}z_a \ |z_a|^{-\alpha_2}|z_a - w|^{-\alpha_1}|z_a - 1|^{-\alpha_2'} \ \frac{-p_2' \cdot \lambda}{1 - z_a}$$

$$= +(-p_2' \cdot \lambda)$$

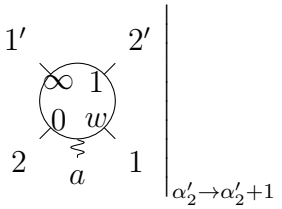

. (A.18)

Other integrals over the intervals $(-\infty, 0), (w, 1), (1, \infty)$ are evaluated in a similar manner.

We are interested in the HES-tachyon to HES-tachyon scattering. Picking out the HES-pole:

$$v,\ v' \sim 2(N-1), \quad i.e. \quad \alpha_2 \sim N_a,\ \beta_2' \sim N_b', \tag{A.19}$$

the photon integral reduces to

$$Z_a^{212'}(\alpha, p, \lambda; w) = \int_{-\infty}^{\infty} \mathrm{d}z_a \ |z_a|^{-\alpha_2}|z_a - w|^{-\alpha_1}|z_a - 1|^{-\alpha_2'} \left(\frac{-p_2 \cdot \lambda}{-z_a} + \frac{-p_1 \cdot \lambda}{w - z_a} + \frac{-p_2' \cdot \lambda}{1 - z_a} \right)$$

$$\sim$$

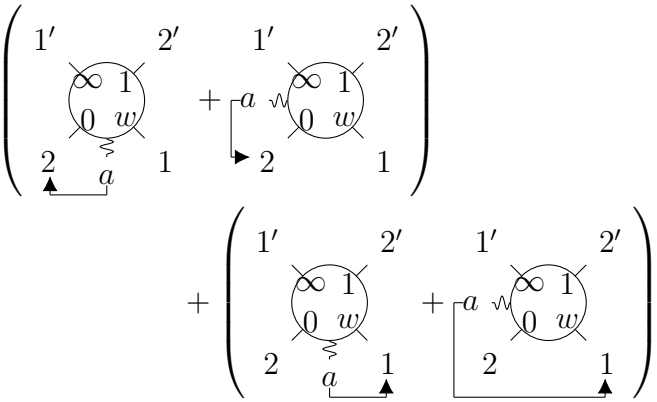

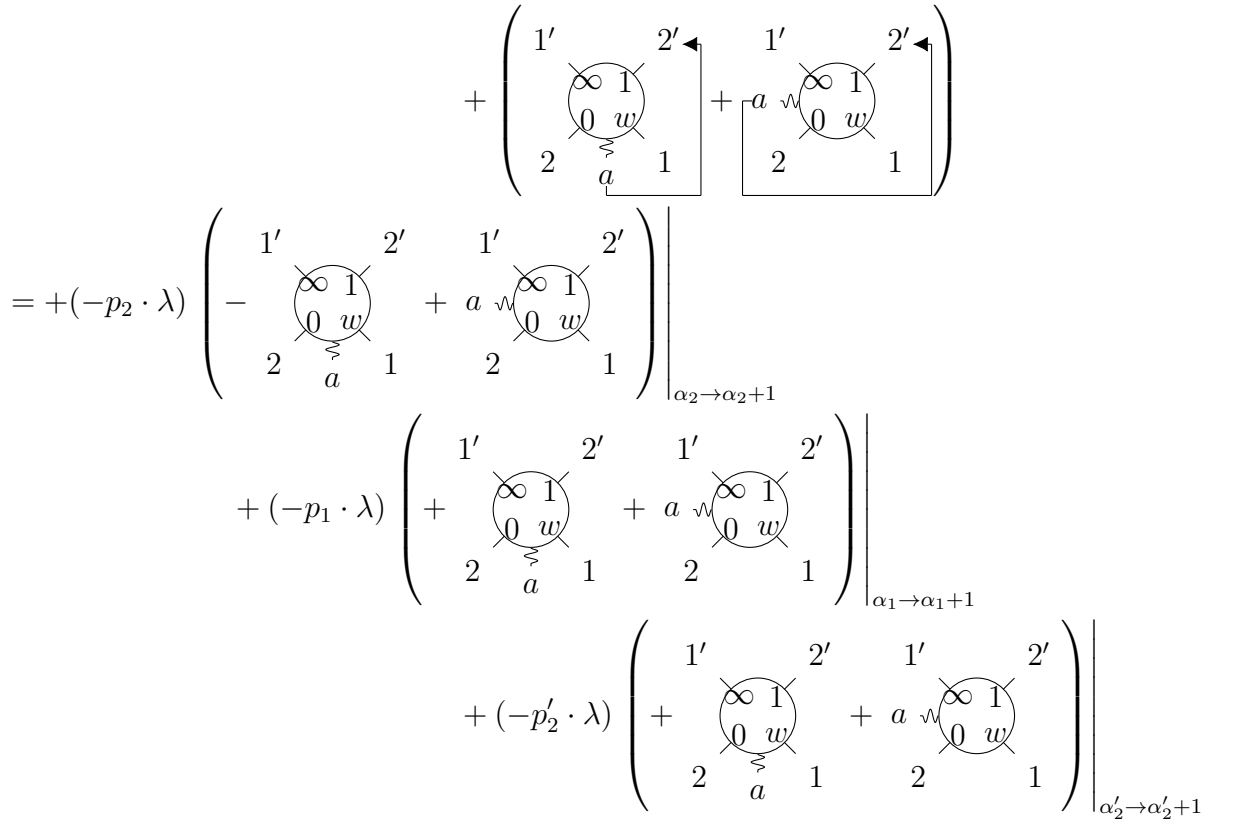

(A.20)

Using a formula for the hypergeometric function (see *e.g.* Eq. 15.8.4 in [78]),

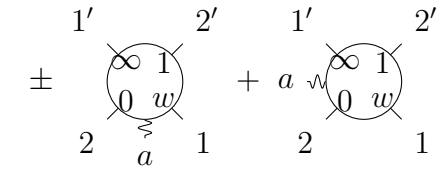

$$
\begin{aligned}
&= \pm w^{1-\alpha_2-\alpha_1}\Gamma(-\alpha_2+1)\Gamma(-\alpha_1+1)\,\mathbf{F}\left(\begin{array}{c}\alpha_2',\quad -\alpha_2+1\\ -\alpha_2-\alpha_1+2\end{array};w\right)\\
&\qquad + \Gamma(\alpha_2+\alpha_1+\alpha_2'-1)\Gamma(-\alpha_2+1)\,\mathbf{F}\left(\begin{array}{c}\alpha_1,\quad \alpha_2+\alpha_1+\alpha_2'-1\\ \alpha_1+\alpha_2'\end{array};1-w\right)\\
&= \pm w^{1-\alpha_2-\alpha_1}\Gamma(-\alpha_2+1)\Gamma(-\alpha_1+1)\,\mathbf{F}\left(\begin{array}{c}\alpha_2',\quad -\alpha_2+1\\ -\alpha_2-\alpha_1+2\end{array};w\right)\\
&\quad + \Gamma(\alpha_2+\alpha_1+\alpha_2'-1)\Gamma(-\alpha_2+1)\frac{\pi}{\sin\pi(-\alpha_2-\alpha_1+1)}\\
&\quad \times\left[\frac{1}{\Gamma(\alpha_2')\Gamma(-\alpha_2+1)}\mathbf{F}\left(\begin{array}{c}\alpha_1,\quad \alpha_2+\alpha_1+\alpha_2'-1\\ \alpha_2+\alpha_1\end{array};w\right)\right.\\
&\qquad\left. -\frac{w^{-\alpha_2-\alpha_1+1}}{\Gamma(\alpha_1)\Gamma(\alpha_2+\alpha_1+\alpha_2'-1)}\mathbf{F}\left(\begin{array}{c}\alpha_2',\quad -\alpha_2+1\\ -\alpha_2-\alpha_1+2\end{array};w\right)\right]
\end{aligned}
$$

$$
\begin{aligned}
&\sim \pm w^{1-\alpha_2-\alpha_1}\Gamma(-\alpha_2+1)\Gamma(-\alpha_1+1)\,\mathbf{F}\left(\begin{array}{c}\alpha_2', \quad -\alpha_2+1\\ -\alpha_2-\alpha_1+2\end{array};w\right)\\
&\quad -\Gamma(\alpha_2+\alpha_1+\alpha_2'-1)\Gamma(-\alpha_2+1)\frac{\pi}{\sin\pi(-\alpha_2-\alpha_1+1)}\\
&\qquad\qquad\qquad\qquad \times\frac{w^{-\alpha_2-\alpha_1+1}}{\Gamma(\alpha_1)\Gamma(\alpha_2+\alpha_1+\alpha_2'-1)}\mathbf{F}\left(\begin{array}{c}\alpha_2', \quad -\alpha_2+1\\ -\alpha_2-\alpha_1+2\end{array};w\right)\\
&=\left(\pm 1-\frac{\sin\pi\alpha_1}{\sin\pi(-\alpha_2-\alpha_1+1)}\right)\Gamma(-\alpha_2+1)\Gamma(-\alpha_1+1)\,w^{-\alpha_2-\alpha_1+1}\mathbf{F}\left(\begin{array}{c}\alpha_2', \quad -\alpha_2+1\\ -\alpha_2-\alpha_1+2\end{array};w\right)\\
&\sim \left(\pm 1+(-1)^{-\alpha_2+1}\right)
\end{aligned}
$$

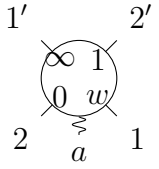

(A.21)

When N_a is even, the integral $Z_a^{212'}(\alpha,p,\lambda;w)$ trivially vanishes. Thus in the following computations, we assume that N_a is odd for any $a=1,\dots,J$. Then

$$
\begin{aligned}
&Z_a^{212'}(\alpha,p,\lambda;w)\\
&\sim +(p_2\cdot\lambda)(+2)
\end{aligned}
$$

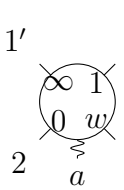

$$
\Big|_{\alpha_2\to\alpha_2+1}
+(p_1\cdot\lambda)(-2)
$$

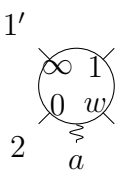

$$
\Big|_{\alpha_1\to\alpha_1+1}
+(p_2'\cdot\lambda)(-2)
$$

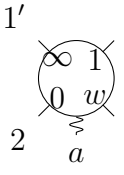

$$
\Big|_{\alpha_2'\to\alpha_2'+1}
\qquad (A.22)
$$

A.3 Tachyon integral

To proceed, let us expand the hypergeometric function as

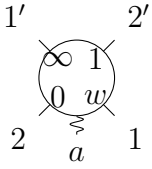

$$
= w^{-\alpha_2-\alpha_1+1}\Gamma(-\alpha_2+1)\Gamma(-\alpha_1+1)\,\mathbf{F}\left(\begin{array}{c}\alpha_2', \quad -\alpha_2+1\\ -\alpha_2-\alpha_1+2\end{array};w\right)
$$

$$= w^{-\alpha_2-\alpha_1+1} \sum_{k=0}^{\infty} c_k(\alpha_2, \alpha_1, \alpha_2')\, w^k. \tag{A.23}$$

Here we have defined

$$\begin{aligned}
&c_k(\alpha_2, \alpha_1, \alpha_2') \\
&= \frac{\Gamma(-\alpha_2+1)\Gamma(-\alpha_1+1)}{\Gamma(-\alpha_2-\alpha_1+2)} \frac{\Gamma(\alpha_2'+k)}{\Gamma(\alpha_2')} \frac{\Gamma(-\alpha_2+1+k)}{\Gamma(-\alpha_2+1)} \frac{\Gamma(-\alpha_2-\alpha_1+2)}{\Gamma(-\alpha_2-\alpha_1+2+k)} \frac{1}{\Gamma(k+1)} \\
&\sim \frac{\pi}{\sin \pi\alpha_2} \frac{1}{\Gamma(k+1)\Gamma(\alpha_2-k)} \frac{\Gamma(\alpha_2-k+\alpha_1-1)}{\Gamma(\alpha_1)} \frac{\Gamma(\alpha_2'+k)}{\Gamma(\alpha_2')}.
\end{aligned} \tag{A.24}$$

Then

$$\begin{aligned}
&Z_a^{212'}(\alpha, p, \lambda; w) \\
&\sim (p_2\cdot\lambda)(+2)\, w^{-\alpha_2-\alpha_1} c_k(\alpha_2+1, \alpha_1, \alpha_2')\, w^k + (p_1\cdot\lambda)(-2)\, w^{-\alpha_2-\alpha_1} c_k(\alpha_2, \alpha_1+1, \alpha_2')\, w^k \\
&\qquad + (p_2'\cdot\lambda)(-2)\, w^{-\alpha_2-\alpha_1} \sum_{k=0}^{\infty} c_k(\alpha_2, \alpha_1, \alpha_2'+1)\, w^{k+1}.
\end{aligned} \tag{A.25}$$

Now let us assume that

$$(p_1+p_2)\cdot\lambda = (p_2'+p_1')\cdot\lambda' = 0 \tag{A.26}$$

for simplicity. These conditions are satisfied, for example, in the center-of-mass frame. The first two terms in (A.25) are rearranged as

$$\begin{aligned}
Z_a^{212'}(\alpha, p, \lambda; w) &\sim (p_2\cdot\lambda)(+2)\, w^{-\alpha_2-\alpha_1} \sum_{k=0}^{\alpha_2\sim N_a} c_k(\alpha_2+1, \alpha_1+1, \alpha_2')\, w^k \\
&\quad + (p_2'\cdot\lambda)(-2)\, w^{-\alpha_2-\alpha_1} \sum_{k=0}^{\alpha_2\sim N_a} c_{k-1}(\alpha_2, \alpha_1, \alpha_2'+1)\, w^k.
\end{aligned} \tag{A.27}$$

Similarly, by replacements $2 \leftrightarrow 2', w \to 1-w, \alpha \to \beta, \lambda \to \lambda'$, we obtain

$$\begin{aligned}
Z_b^{212'}(\beta, p, \lambda'; w) &\sim (p_2'\cdot\lambda')(+2)\, (1-w)^{-\beta_2'-\beta_1} \sum_{l=0}^{\beta_2'\sim N_b'} c_l(\beta_2'+1, \beta_1+1, \beta_2)\, (1-w)^l \\
&\quad + (p_2\cdot\lambda')(-2)\, (1-w)^{-\beta_2'-\beta_1} \sum_{l=0}^{\beta_2'\sim N_b'} c_{l-1}(\beta_2', \beta_1, \beta_2+1)\, (1-w)^l.
\end{aligned} \tag{A.28}$$

Substituting these into (A.5), we can perform the integral over w. Noting that

$$p_1\cdot p_2 - \sum_{a=1}^{J} \alpha_2 - \sum_{a=1}^{J} \alpha_1 = -2 - s/2, \tag{A.29}$$

$$p_1 \cdot p_2' - \sum_{b=1}^{J} \beta_2' - \sum_{b=1}^{J} \beta_1 = -2 - t/2, \tag{A.30}$$

the result is

$$\mathcal{A}_{st} \sim \sum_{\{i_a=2,2'\}} \sum_{\{j_b=2,2'\}} \sum_{\{k_a=0\}}^{\{N_a\}} \sum_{\{l_b=0\}}^{\{N_b'\}} \left(\prod_{a=1}^{J} (p_{i_a} \cdot \lambda)\, c_{k_a}^{(i_a)} \right) \left(\prod_{b=1}^{J} (p_{j_b} \cdot \lambda')\, d_{l_b}^{(j_b)} \right) B(-\alpha(s)+k, -\alpha(t)+l) \tag{A.31}$$

where

$$c_k^{(2)} = c_k(\alpha_2 + 1, \alpha_1 + 1, \alpha_2'), \tag{A.32}$$

$$c_k^{(2')} = -c_{k-1}(\alpha_2, \alpha_1, \alpha_2' + 1), \tag{A.33}$$

$$d_l^{(2)} = -c_{l-1}(\beta_2', \beta_1, \beta_2 + 1), \tag{A.34}$$

$$d_l^{(2')} = c_l(\beta_2' + 1, \beta_1 + 1, \beta_2), \tag{A.35}$$

and where

$$B(a,b) = \frac{\Gamma(a)\Gamma(b)}{\Gamma(a+b)}, \quad \alpha(x) = 1 + x/2, \tag{A.36}$$

$$k = \sum_{a=1}^{J} k_a, \quad l = \sum_{b=1}^{J} l_b. \tag{A.37}$$

Here ends the derivation of the HES-tachyon to HES-tachyon amplitude, given in (A.31).

A.4 Another expression for the amplitude

In this subsection, for a consistency check of our amplitude formula (A.31), we study another expression of the amplitude.

Similar computations show that

$Z_b^{212'}(\beta, p, \lambda', w)$

$\sim +(p_2 \cdot \lambda')(+2)$ 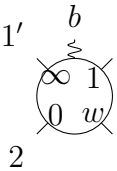

$\Big|_{\beta_2 \to \beta_2 + 1}$ $+ (p_1 \cdot \lambda')(+2)$ 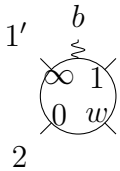

$\Big|_{\beta_1 \to \beta_1 + 1}$

$+ (p_2' \cdot \lambda')(+2)$ 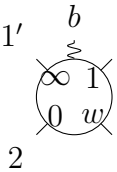

$\Big|_{\beta_2' \to \beta_2' + 1}$

$$\sim +(p_2\cdot\lambda')(+2)\left(\left.\begin{array}{c}1'\quad b\quad 2'\\ \infty\ 1\\ 0\ \ w\\ 2\qquad 1\end{array}\right|_{\beta_2\to\beta_2+1}-\left.\begin{array}{c}1'\quad b\quad 2'\\ \infty\ 1\\ 0\ \ w\\ 2\qquad 1\end{array}\right|_{\beta_1\to\beta_1+1}\right)$$

$$+(p_2'\cdot\lambda')(+2)\left.\begin{array}{c}1'\quad b\quad 2'\\ \infty\ 1\\ 0\ \ w\\ 2\qquad 1\end{array}\right|_{\beta_2'\to\beta_2'+1} \tag{A.38}$$

Using a formula for the hypergeometric function (see *e.g.* Eq. 15.8.1 in [78]),

$$\left.\begin{array}{c}1'\quad b\quad 2'\\ \infty\ 1\\ 0\ \ w\\ 2\qquad 1\end{array}\right|_{\beta_2\to\beta_2+1}-\left.\begin{array}{c}1'\quad b\quad 2'\\ \infty\ 1\\ 0\ \ w\\ 2\qquad 1\end{array}\right|_{\beta_1\to\beta_1+1}$$

$$=\Gamma(\beta_2'+\beta_1+\beta_2)\Gamma(-\beta_2'+1)\left[\mathbf{F}\left(\begin{array}{c}\beta_1,\quad \beta_2'+\beta_1+\beta_2\\ \beta_1+\beta_2+1\end{array};w\right)-\mathbf{F}\left(\begin{array}{c}\beta_1+1,\quad \beta_2'+\beta_1+\beta_2\\ \beta_1+\beta_2+1\end{array};w\right)\right]$$

$$=\Gamma(\beta_2'+\beta_1+\beta_2+1)\Gamma(-\beta_2'+1)\,(-w)\,\mathbf{F}\left(\begin{array}{c}\beta_1+1,\quad \beta_2'+\beta_1+\beta_2+1\\ \beta_1+\beta_2+2\end{array};w\right)$$

$$=(1-w)^{-\beta_2'-\beta_1}\,\Gamma(\beta_2'+\beta_1+\beta_2+1)\Gamma(-\beta_2'+1)\,(-w)\,\mathbf{F}\left(\begin{array}{c}\beta_2+1,\quad -\beta_2'+1\\ \beta_1+\beta_2+2\end{array};w\right)$$

$$=(1-w)^{-\beta_2'-\beta_1}\,\Gamma(-\beta_1'+1)\Gamma(-\beta_2'+1)\,(-w)\,\mathbf{F}\left(\begin{array}{c}\beta_2+1,\quad -\beta_2'+1\\ -\beta_2'-\beta_1'+2\end{array};w\right)$$

$$=(1-w)^{-\beta_2'-\beta_1}\,(-w)\sum_{l=0}^{\infty}c_l(\beta_2',\beta_1',\beta_2+1)\,w^l$$

$$=(1-w)^{-\beta_2'-\beta_1}\sum_{l=0}^{\beta_2'\sim N_b'}-c_{l-1}(\beta_2',\beta_1',\beta_2+1)\,w^l, \tag{A.39}$$

$$\left.\begin{array}{c}1'\quad b\quad 2'\\ \infty\ 1\\ 0\ \ w\\ 2\qquad 1\end{array}\right|_{\beta_2'\to\beta_2'+1}$$

$$=\Gamma(\beta_2'+\beta_1+\beta_2)\Gamma(-\beta_2')\,\mathbf{F}\left(\begin{array}{c}\beta_1,\quad \beta_2'+\beta_1+\beta_2\\ \beta_1+\beta_2\end{array};w\right)$$

$$= (1-w)^{-\beta_2'-\beta_1}\,\Gamma(\beta_2'+\beta_1+\beta_2)\Gamma(-\beta_2')\,\mathbf{F}\left(\begin{array}{c}\beta_2,\quad -\beta_2'\\ \beta_1+\beta_2\end{array};w\right)$$

$$= (1-w)^{-\beta_2'-\beta_1}\,\Gamma(-\beta_1')\Gamma(-\beta_2')\,\mathbf{F}\left(\begin{array}{c}\beta_2,\quad -\beta_2'\\ -\beta_2'-\beta_1'\end{array};w\right)$$

$$= (1-w)^{-\beta_2'-\beta_1}\sum_{l=0}^{\beta_2'\sim N_b'} c_l(\beta_2'+1,\beta_1'+1,\beta_2)\,w^l. \tag{A.40}$$

Substituting these into (A.5), and noting that

$$p_1\cdot p_2-\sum_{a=1}^{J}\alpha_2-\sum_{a=1}^{J}\alpha_1=-2-s/2, \tag{A.41}$$

$$p_1\cdot p_2'-\sum_{b=1}^{J}\beta_2'-\sum_{b=1}^{J}\beta_1=-2-t/2, \tag{A.42}$$

we can perform the integral over w. The result is

$$\mathcal{A}_{st}\sim\sum_{\{i_a=2,2'\}}\sum_{\{j_b=2,2'\}}\sum_{\{k_a=0\}}^{\{N_a\}}\sum_{\{l_b=0\}}^{\{N_b'\}} \left(\prod_{a=1}^{J}(p_{i_a}\cdot\lambda)\,c_{k_a}^{(i_a)}\right)\left(\prod_{b=1}^{J}(p_{j_b}\cdot\lambda')\,d_{l_b}^{(j_b)}\right)B(-\alpha(s)+k+l,-\alpha(t)) \tag{A.43}$$

where

$$c_k^{(2)}=c_k(\alpha_2+1,\alpha_1+1,\alpha_2'), \tag{A.44}$$

$$c_k^{(2')}=-c_{k-1}(\alpha_2,\alpha_1,\alpha_2'+1), \tag{A.45}$$

$$d_l^{(2)}=-c_{l-1}(\beta_2',\beta_1',\beta_2+1), \tag{A.46}$$

$$d_l^{(2')}=c_l(\beta_2'+1,\beta_1'+1,\beta_2), \tag{A.47}$$

and where

$$k=\sum_{a=1}^{J}k_a,\quad l=\sum_{b=1}^{J}l_b, \tag{A.48}$$

$$B(a,b)=\frac{\Gamma(a)\Gamma(b)}{\Gamma(a+b)},\quad \alpha(x)=1+x/2. \tag{A.49}$$

In spite of the superficially different appearance of the amplitude formula (A.31) and the formula (A.43), they are equivalent. The former depends on β_1 and both of the s,t-channels are shifted, while the latter depends on β_1' and only the s-channel is shifted.

References

[1] S. W. Hawking, "Particle Creation by Black Holes," *Commun. Math. Phys.* **43** (1975) 199–220. [Erratum: Commun.Math.Phys. 46, 206 (1976)].

[2] S. W. Hawking, "Breakdown of Predictability in Gravitational Collapse," *Phys. Rev. D* **14** (1976) 2460–2473.

[3] G. 't Hooft, "The black hole interpretation of string theory," *Nuclear Physics B* **335** no. 1, (1990) 138–154. https://www.sciencedirect.com/science/article/pii/055032139090174C.

[4] G. 't Hooft, "The Black hole horizon as a quantum surface," *Phys. Scripta T* **36** (1991) 247–252.

[5] E. P. Verlinde and H. L. Verlinde, "A Unitary S matrix and 2-D black hole formation and evaporation," *Nucl. Phys. B* **406** (1993) 43–58, arXiv:hep-th/9302022.

[6] K. Schoutens, H. Verlinde, and E. Verlinde, "Quantum black hole evaporation," *Phys. Rev. D* **48** (Sep, 1993) 2670–2685. https://link.aps.org/doi/10.1103/PhysRevD.48.2670.

[7] G. 't Hooft, "The Scattering matrix approach for the quantum black hole: An Overview," *Int. J. Mod. Phys. A* **11** (1996) 4623–4688, arXiv:gr-qc/9607022.

[8] T. Dray and G. 't Hooft, "The gravitational shock wave of a massless particle," *Nuclear Physics B* **253** (1985) 173–188. https://www.sciencedirect.com/science/article/pii/0550321385905255.

[9] G. 't Hooft, "Strings From Gravity," *Phys. Scripta T* **15** (1987) 143.

[10] L. Susskind, L. Thorlacius, and J. Uglum, "The Stretched horizon and black hole complementarity," *Phys. Rev. D* **48** (1993) 3743–3761, arXiv:hep-th/9306069.

[11] L. Susskind, "String theory and the principles of black hole complementarity," *Phys. Rev. Lett.* **71** (1993) 2367–2368, arXiv:hep-th/9307168.

[12] L. Susskind and L. Thorlacius, "Gedanken experiments involving black holes," *Phys. Rev. D* **49** (1994) 966–974, arXiv:hep-th/9308100.

[13] L. Susskind and J. Lindesay, *An Introduction to Black Holes, Information and the String Theory Revolution.* WORLD SCIENTIFIC, 2004.

https://www.worldscientific.com/doi/pdf/10.1142/5689.
https://www.worldscientific.com/doi/abs/10.1142/5689.

[14] L. Susskind, "Some speculations about black hole entropy in string theory," arXiv:hep-th/9309145.

[15] M. J. Bowick, L. Smolin, and L. C. R. Wijewardhana, "Role of string excitations in the last stages of black-hole evaporation," *Phys. Rev. Lett.* **56** (Feb, 1986) 424–427. https://link.aps.org/doi/10.1103/PhysRevLett.56.424.

[16] A. Strominger and C. Vafa, "Microscopic origin of the Bekenstein-Hawking entropy," *Phys. Lett. B* **379** (1996) 99–104, arXiv:hep-th/9601029.

[17] E. Halyo, B. Kol, A. Rajaraman, and L. Susskind, "Counting Schwarzschild and charged black holes," *Phys. Lett. B* **401** (1997) 15–20, arXiv:hep-th/9609075.

[18] G. T. Horowitz and J. Polchinski, "A Correspondence principle for black holes and strings," *Phys. Rev. D* **55** (1997) 6189–6197, arXiv:hep-th/9612146.

[19] G. T. Horowitz and J. Polchinski, "Selfgravitating fundamental strings," *Phys. Rev. D* **57** (1998) 2557–2563, arXiv:hep-th/9707170.

[20] T. Damour and G. Veneziano, "Selfgravitating fundamental strings and black holes," *Nucl. Phys. B* **568** (2000) 93–119, arXiv:hep-th/9907030.

[21] A. Giveon and D. Kutasov, "Fundamental strings and black holes," *Journal of High Energy Physics* **2007** no. 01, (Jan, 2007) 071. https://dx.doi.org/10.1088/1126-6708/2007/01/071.

[22] Y. Chen, J. Maldacena, and E. Witten, "On the black hole/string transition," arXiv:2109.08563 [hep-th].

[23] L. Susskind, "Black Hole-String Correspondence," arXiv:2110.12617 [hep-th].

[24] J. Polchinski, "Chaos in the black hole S-matrix," arXiv:1505.08108 [hep-th].

[25] S. H. Shenker and D. Stanford, "Black holes and the butterfly effect," *JHEP* **03** (2014) 067, arXiv:1306.0622 [hep-th].

[26] S. H. Shenker and D. Stanford, "Multiple Shocks," *JHEP* **12** (2014) 046, arXiv:1312.3296 [hep-th].

[27] S. H. Shenker and D. Stanford, "Stringy effects in scrambling," *JHEP* **05** (2015) 132, arXiv:1412.6087 [hep-th].

[28] A. Kitaev, "Hidden Correlations in the Hawking Radiation and Thermal Noise." The 2015 Breakthrough Prize Symposium, Nov. 10, 2014. https://youtu.be/OQ9qN8j7EZI. (accessed: Nov. 04, 2022).

[29] A. Kitaev, "Hidden Correlations in the Hawking Radiation and Thermal Noise." Kavli Institute for Theoretical Physics, Theory Seminars, Feb. 12, 2015. https://online.kitp.ucsb.edu/online/joint98/kitaev/. (accessed: Nov. 04, 2022).

[30] A. Kitaev, "A simple model of quantum holography (part 1)." KITP Program: Entanglement in Strongly-Correlated Quantum Matter, Apr. 07, 2015. https://online.kitp.ucsb.edu/online/entangled15/kitaev/. (accessed: Nov. 04, 2022).

[31] A. Kitaev, "A simple model of quantum holography (part 2)." KITP Program: Entanglement in Strongly-Correlated Quantum Matter, May 27, 2015. https://online.kitp.ucsb.edu/online/entangled15/kitaev2/. (accessed: Nov. 04, 2022).

[32] Y. Sekino and L. Susskind, "Fast Scramblers," *JHEP* **10** (2008) 065, arXiv:0808.2096 [hep-th].

[33] P. Hayden and J. Preskill, "Black holes as mirrors: Quantum information in random subsystems," *JHEP* **09** (2007) 120, arXiv:0708.4025 [hep-th].

[34] B. Yoshida and A. Kitaev, "Efficient decoding for the Hayden-Preskill protocol," arXiv:1710.03363 [hep-th].

[35] J. Maldacena, S. H. Shenker, and D. Stanford, "A bound on chaos," *JHEP* **08** (2016) 106, arXiv:1503.01409 [hep-th].

[36] K. Hashimoto, K. Murata, N. Tanahashi, and R. Watanabe, "A bound on energy dependence of chaos," arXiv:2112.11163 [hep-th].

[37] T. Xu, T. Scaffidi, and X. Cao, "Does scrambling equal chaos?," *Phys. Rev. Lett.* **124** no. 14, (2020) 140602, arXiv:1912.11063 [cond-mat.stat-mech].

[38] K. Hashimoto, K.-B. Huh, K.-Y. Kim, and R. Watanabe, "Exponential growth of out-of-time-order correlator without chaos: inverted harmonic oscillator," *JHEP* **11** (2020) 068, arXiv:2007.04746 [hep-th].

[39] S. Müller, S. Heusler, P. Braun, F. Haake, and A. Altland, "Periodic-orbit theory of universality in quantum chaos," *Phys. Rev. E* **72** (Oct, 2005) 046207. https://link.aps.org/doi/10.1103/PhysRevE.72.046207.

[40] F. Haake, *Quantum Signatures of Chaos*. Springer Series in Synergetics. Springer Berlin, Heidelberg, 2010.

[41] T. H. Seligman and H. Nishioka, *Quantum Chaos and Statistical Nuclear Physics*. Lecture Notes in Physics. Springer Berlin, Heidelberg, 1986.

[42] S. L. Les Houches, "Chaos and quantum physics, eds. m.-j. giannoni, a. voros and j. zinn-justin," 1991.

[43] D. J. Gross and V. Rosenhaus, "Chaotic scattering of highly excited strings," *JHEP* **05** (2021) 048, arXiv:2103.15301 [hep-th].

[44] V. Rosenhaus, "Chaos in a Many-String Scattering Amplitude," *Phys. Rev. Lett.* **129** no. 3, (2022) 031601, arXiv:2112.10269 [hep-th].

[45] V. Rosenhaus, "Chaos in the Quantum Field Theory S-Matrix," *Phys. Rev. Lett.* **127** no. 2, (2021) 021601, arXiv:2003.07381 [hep-th].

[46] M. Firrotta and V. Rosenhaus, "Photon emission from an excited string," *JHEP* **09** (2022) 211, arXiv:2207.01641 [hep-th].

[47] M. Bianchi, M. Firrotta, J. Sonnenschein, and D. Weissman, "A measure for chaotic scattering amplitudes," arXiv:2207.13112 [hep-th].

[48] T. Tél and M. Gruiz, *Chaotic Dynamics: An Introduction Based on Classical Mechanics*. Cambridge University Press, 2006.

[49] E. Ott, *Chaos in Dynamical Systems*. Cambridge University Press, 2 ed., 2002.

[50] Y.-C. Lai and T. Tél, *Transient Chaos*. Applied Mathematical Sciences. Springer New York, NY, 2011.

[51] J. M. Seoane and M. A. F. Sanjuán, "New developments in classical chaotic scattering," *Reports on Progress in Physics* **76** no. 1, (Dec, 2012) 016001. https://dx.doi.org/10.1088/0034-4885/76/1/016001.

[52] P. Gaspard, *Chaos, Scattering and Statistical Mechanics*. Cambridge Nonlinear Science Series. Cambridge University Press, 1998.

[53] E. Del Giudice, P. Di Vecchia, and S. Fubini, "General properties of the dual resonance model," *Annals Phys.* **70** (1972) 378–398.

[54] M. Bianchi and M. Firrotta, "DDF operators, open string coherent states and their scattering amplitudes," *Nucl. Phys. B* **952** (2020) 114943, arXiv:1902.07016 [hep-th].

[55] M. Hindmarsh and D. Skliros, "Covariant Closed String Coherent States," *Phys. Rev. Lett.* **106** (2011) 081602, arXiv:1006.2559 [hep-th].

[56] D. Skliros and M. Hindmarsh, "String Vertex Operators and Cosmic Strings," *Phys. Rev. D* **84** (2011) 126001, arXiv:1107.0730 [hep-th].

[57] L. Cangemi and P. Pichini, "Classical Limit of Higher-Spin String Amplitudes," arXiv:2207.03947 [hep-th].

[58] K. Hashimoto, S. Kinoshita, and K. Murata, "Imaging black holes through the AdS/CFT correspondence," *Phys. Rev. D* **101** no. 6, (2020) 066018, arXiv:1811.12617 [hep-th].

[59] K. Hashimoto, S. Kinoshita, and K. Murata, "Einstein Rings in Holography," *Phys. Rev. Lett.* **123** no. 3, (2019) 031602, arXiv:1906.09113 [hep-th].

[60] A. I. Larkin and Y. N. Ovchinnikov, "Quasiclassical method in the theory of superconductivity," *Journal of Experimental and Theoretical Physics* (1969) .

[61] R. H. Brandenberger and C. Vafa, "Superstrings in the Early Universe," *Nucl. Phys. B* **316** (1989) 391–410.

[62] S. Bleher, C. Grebogi, and E. Ott, "Bifurcation to chaotic scattering," *Physica D: Nonlinear Phenomena* **46** no. 1, (1990) 87–121.

[63] G. Veneziano, "Construction of a crossing - symmetric, Regge behaved amplitude for linearly rising trajectories," *Nuovo Cim. A* **57** (1968) 190–197.

[64] D. J. Gross and P. F. Mende, "The high-energy behavior of string scattering amplitudes," *Physics Letters B* **197** no. 1, (1987) 129–134. https://www.sciencedirect.com/science/article/pii/0370269387903558.

[65] D. J. Gross and P. F. Mende, "String theory beyond the planck scale," *Nuclear Physics B* **303** no. 3, (1988) 407–454. https://www.sciencedirect.com/science/article/pii/0550321388903902.

[66] D. J. Gross and J. L. Mañes, "The high-energy behavior of open string scattering," *Nuclear Physics* **326** (1989) 73–107.

[67] P. F. Mende and H. Ooguri, "Borel summation of string theory for planck scale scattering," *Nuclear Physics B* **339** no. 3, (1990) 641–662. https://www.sciencedirect.com/science/article/pii/055032139090202O.

[68] M. V. Berry and C. J. Howls, "Hyperasymptotics for integrals with saddles," *Proceedings: Mathematical and Physical Sciences* **434** no. 1892, (1991) 657–675. http://www.jstor.org/stable/51890.

[69] W. G. C. Boyd, "Error bounds for the method of steepest descents," *Proceedings: Mathematical and Physical Sciences* **440** no. 1910, (1993) 493–518. http://www.jstor.org/stable/52396.

[70] E. Delabaere, "Effective resummation methods for an implicit resurgent function," *arXiv preprint math-ph/0602026* (2006) .

[71] W. G. C. Boyd, "Gamma function asymptotics by an extension of the method of steepest descents," *Proceedings: Mathematical and Physical Sciences* **447** no. 1931, (1994) 609–630. http://www.jstor.org/stable/52450.

[72] M. Li and T. Yoneya, "Short distance space-time structure and black holes in string theory: A Short review of the present status," *Chaos Solitons Fractals* **10** (1999) 423–443, arXiv:hep-th/9806240.

[73] T. Yoneya, "String theory and space-time uncertainty principle," *Prog. Theor. Phys.* **103** (2000) 1081–1125, arXiv:hep-th/0004074.

[74] T. Yoneya, "On the Short-Distance Space-Time Structure of String Theory: Personal Recollections," *Looking Beyond the Frontiers of Science* (2022) 313–327.

[75] T. Yoneya. Private communication.

[76] K. Hashimoto, Y. Matsuo, and T. Yoda, "Transient chaos analysis of string scattering," arXiv:2208.08380 [hep-th].

[77] K. Hashimoto, Y. Matsuo, and T. Yoda, "String is a double slit," arXiv:2206.10951 [hep-th].

[78] "Degital library of mathematical functions, chapter 15 hypergeometric function." https://dlmf.nist.gov/15.8. Accessed: 2022-08-10.